THE UNIVERSITY *of* EDINBURGH

This thesis has been submitted in fulfilment of the requirements for a postgraduate degree (e.g. PhD, MPhil, DClinPsychol) at the University of Edinburgh. Please note the following terms and conditions of use:

This work is protected by copyright and other intellectual property rights, which are retained by the thesis author, unless otherwise stated.
A copy can be downloaded for personal non-commercial research or study, without prior permission or charge.
This thesis cannot be reproduced or quoted extensively from without first obtaining permission in writing from the author.
The content must not be changed in any way or sold commercially in any format or medium without the formal permission of the author.
When referring to this work, full bibliographic details including the author, title, awarding institution and date of the thesis must be given.

Advanced Optical Fibre Communication via Nonlinear Fourier Transform

Iman Tavakkolnia

A thesis submitted for the degree of

Doctor of Philosophy

The University of Edinburgh

2018

THE UNIVERSITY *of* EDINBURGH
School of Engineering

Dedication

To my dear parents,

for their endless care, support, and love.

To the love of my life, ***Mahdie***

for all her patience, advice, and unconditional support.

To my beautiful little girl, ***Elena Rose****.*

for the joy she brought to our lives.

This was not possible without you all.

Iman Tavakkolnia

August 2017

Abstract

Optical fibre communication using the Nonlinear Fourier transform (NFT) is one of the potential solutions to tackle the so-called capacity crunch problem in long-haul optical fibre networks. The NFT transforms the nonlinear propagation of temporal signal, governed by the nonlinear Schrödinger equation (NLSE), into simple linear evolutions of continuous and discrete spectra in the so-called nonlinear spectral domain. These spectra and the corresponding nonlinear spectral domain, defined by the NFT, are the generalized counterparts of the linear spectrum and frequency domain defined by the ordinary Fourier transform. Using the NFT, the optical fibre channel is effectively linearised, and the basic idea is to utilize degrees of freedom in the nonlinear spectral domain for data transmission. However, many aspects of this concept require rigorous investigation due to complexity and infancy of the approach. In this thesis, the aim is to provide a comprehensive investigation of data transmission over mainly the continues spectrum (CS) and partly over of the discrete spectrum (DS) of nonlinear optical fibres. First, an optical fibre communication system is defined, in which solely the CS carries the information. A noise model in the nonlinear spectral domain is derived for such a system by asymptotic analysis as well as extensive simulations for different scenarios of practical interest. It is demonstrated that the noise added to the signal in CS is severely signal-dependent such that the effective signalling space is limited. The variance normalizing transform (VNT) is used to mathematically verify the limits of signalling spaces and also estimate the channel capacity. The numerical results predict a remarkable capacity for signalling only on the CS (e.g., 6 bits/symbol for a 2000-km link), yet it is demonstrated that the capacity saturates at high power. Next, the broadening effect of chromatic dispersion is analysed, and it is confirmed that some system parameters, such as symbol rate in the nonlinear spectral domain, can be optimized so that the required temporal guard interval between the subsequently transmitted data packets is minimized, and thus the effective data rate is significantly enhanced. Furthermore, three modified signalling techniques are proposed and analysed based on the particular statistics of the noise added to the CS. All proposed methods display improved performance in terms of error rate and reach distance. For instance, using one of the proposed techniques and optimized

parameters, a 7100-km distance can be reached by signalling on the CS at a rate of 9.6 Gbps. Furthermore, the impact of polarization mode dispersion (PMD) is examined for the first time, as an inevitable impairment in long-haul optical fibre links. By semi-analytical and numerical investigation, it is demonstrated that the PMD affects the CS by causing signal-dependent phase shift and noise-like errors. It is also verified that the noise is still the dominant cause of performance degradation, yet the effect of PMD should not be neglected in the analysis of NFT-based systems. Finally, the capacity of soliton communication with amplitude modulation (part of the degrees of freedom of DS) is also estimated using VNT. For the first time, the practical constraints, such as the restricted signalling space due to limited bandwidth, are included in this capacity analysis. Furthermore, the achievable data rates are estimated by considering an appropriately defined guard time between soliton pulses. Moreover, the possibility of transmitting data on DS accompanied by an independent CS signalling is also validated, which confirms the potentials of the NFT approach for combating the capacity crunch.

Lay summary

Optical fibre is the only medium that can support the ever-increasing demand for data rate and make the Internet possible. Optical fibre communication systems have kept up with demands for decades thanks to the tremendous research in different disciplines. However, the growth rate of data transmission over optical fibre has slowed down in recent years because all conventional communication methods eventually fail due to the inherent nonlinearity of optical fibre, which makes it different from other communication types, such as wireless. Thus, specific methods are required for enhancing the performance of the optical fibre systems. The recently proposed optical fibre communication based on the nonlinear Fourier transform (NFT) is one of the novel solutions which can address the nonlinearity problem. Unlike previous techniques, which consider the nonlinearity as a source of noise and try to compensate it, the NFT-based approach tries to adapt the system to the existing nonlinearity and exploit it. In this thesis, different aspects of the optical fibre communication using NFT are studied. The channel model of a NFT-based structure is derived, and it is observed that the noise statistics depend on the input signal. This is a very important feature of NFT-based communication, which affects all aspects of the system. Based on such a model, the information capacity of the channel is estimated, and remarkable capacity is predicted only for a part of the available degrees of freedom, called continuous spectrum. Furthermore, different NFT-based signal processing techniques are proposed, and system parameters are optimized to further improve the performance. It is demonstrated that data can be transmitted over more than 7000 kilometres of fibre with a rate of approximately 10 Gigabits per second. Moreover, for the first time, impacts of an unavoidable impairment of the optical fibre channel on NFT-based systems is investigated, and compensation techniques are proposed. Finally, the channel information capacity for the other part of available degrees of freedom, called discrete spectrum, is estimated. It is further demonstrated that it is possible to simultaneously and independently transmit data using both continuous and discrete spectra. This thesis provides a comprehensive study of optical fibre communication using NFT, and confirms its high potentials for future communication systems.

Acknowledgements

I would like to take this opportunity to sincerely thank all the people who helped me during my studies. I would like to offer my sincerest appreciation to my supervisor, Dr. Majid Safari, who guided me during the past four years and devoted so much of his time and energy to my work. Without his continuous enthusiasm, encouragement and support this study would hardly have been completed.

I am deeply grateful to my parents, Marzie Pourkhalili and Rahim Tavakkolnia, who continuously supported me over the years. I feel extremely lucky to have such wonderful parents. I owe my deepest gratitude to my wife, Mahdie Sokhanvar, for her patience, love, and support. I could not achieve this without her.

I would particularly like to thank my thesis reviewers, Prof. Sergei Turitsyn and Dr. Wasiu Popoola, for their insightful comments.

Special thanks to all my friends in Edinburgh, who made it enjoyable to live and work in this wonderful city and helped me during my PhD studies.

Declaration

I declare that this thesis has been composed solely by myself and that it has not been submitted, either in whole or in part, in any previous application for a degree. Except where otherwise acknowledged, the work presented is entirely my own.

Iman Tavakkolnia

Contents

List of Tables

List of Figures

List of abbreviations

ASE . . . . . amplified spontaneous emission

AWGN . . . . . additive white Gaussian noise

BER . . . . . bit error rate

CS . . . . . continuous spectrum

CNLSE . . . . . coupled nonlinear schrödinger equations

DBP . . . . . digital back propagation

DPC . . . . . dispersion pre-compensation

DS . . . . . discrete spectrum

EDFA . . . . . Erbium-doped fibre amplifiers

EVM . . . . . error vector magnitude

FFT . . . . . fast Fourier transform

FWM . . . . . four-wave mixing

GLM . . . . . Gelfan-Levitan-Marchenko

GVD . . . . . group velocity dispersion

HDFEC . . . . . hard decision forward error correction

IFT . . . . . inverse Fourier transform

IFFT . . . . . inverse fast Fourier transform

INFT . . . . . inverse nonlinear Fourier transform

IST . . . . . inverse scattering transform

KdV . . . . . Korteweg-de Vries

NFDM . . . . . nonlinear frequency division multiplexing

NF . . . . . noise figure

NFT . . . . . nonlinear Fourier transform

NIS . . . . . nonlinear inverse synthesis

NLSE . . . . . nonlinear schrödinger equation

OFDM . . . . . orthogonal frequency division multiplexing

OOK . . . . . on-off keying

PAM . . . . . pulse amplitude modulation

PAPR . . . . . peak-to-average power ratio

PDE . . . . . partial differential equation

PDF . . . . . probability distribution function

PMD . . . . . polarization mode dispersion

PMDC . . . . . polarization mode dispersion compensation

PNFT . . . . . periodic nonlinear Fourier transform

PSD . . . . . power spectral density

QAM . . . . . quadrature amplitude modulation

QPSK . . . . . quadrature phase shift keying

RMS . . . . . root-mean-square

SDFEC . . . . . soft decision forward error correction

SER . . . . . symbol error rate

SMF . . . . . single-mode fibre

SNR . . . . . signal-to-noise ratio

SPM . . . . . self-phase modulation

SSMF . . . . . standard single-mode fibre

VNT . . . . . variance normalizing transform

WDM . . . . . wavelength division multiplexing

XPM . . . . . cross-phase modulation

List of mathematical symbols

α	fibre loss factor
$\beta(\omega)$	mode propagation constant
β_i	ith derivative of the propagation constant
β_2	group velocity dispersion
γ	fibre nonlinearity parameter
$\Gamma_L(t)$	noise in GLM-based signalling method
$\delta(\cdot)$	Dirac delta function
ΔT_l	signal temporal width at length l
$\Delta\beta_1$	inverse group velocity difference of two polarization states
$\widetilde{\Delta T_l}$	linear approximation of signal temporal width at length l
κ	number of samples in GLM-based signalling method
λ	nonlinear frequency - spectral parameter of Zakharov-Shabat problem
λ_m	discrete eigenvalues
λ_k	nonlinear frequency at symbol points for CS
Λ	spectral width
ν_0	carrier frequency
$\rho(\lambda)$	continuous spectrum
$\rho_0(\lambda)$	input continuous spectrum
$\tilde{\rho}_L(\lambda)$	received continuous spectrum after phase shift removal
$\hat{\rho}_L(\lambda)$	linearly filtered version of $\tilde{\rho}_L(\lambda)$
ρ	signal-to-noise ratio for soliton communication
σ^2	normalize ASE noise power spectral density
σ_N^2	accumulated normalize ASE noise power spectral density at the receiver

σ_0^2 . . . . . accumulated normalize ASE noise power at the receiver

$\eta_L(\lambda)$ . . . . . effective noise added to the CS

τ . . . . . time (not normalized)

$\boldsymbol{\phi}$ . . . . . boundary eigenfunction vector of Zakharov-Shabat problem

$\boldsymbol{\psi}$ . . . . . boundary eigenfunction vector of Zakharov-Shabat problem

ψ_P . . . . . phase shift as a result of PMD

ω . . . . . angular frequency

ω_0 . . . . . carrier angular frequency

$\mathbf{A}(\omega)$ . . . . . Jones matrix

A_ρ . . . . . maximum amplitude constraint for CS

A . . . . . transmitted soliton amplitude

$A_{\max/\min}$ . . . . maximum/minimum soliton amplitude constraint

$\bar{A}$ . . . . . received soliton amplitude

$a(\lambda, z)$ . . . . . nonlinear Fourier coefficient

$b(\lambda, z)$ . . . . . nonlinear Fourier coefficient

B . . . . . normalized signal bandwidth

c . . . . . speed of light

$C_m(z)$ . . . . . norming constants

C . . . . . capacity

C_R . . . . . capacity of real channel

C_{PP} . . . . . peak power limited capacity for soliton communication

C_A . . . . . asymptotic capacity for soliton communication

D . . . . . fibre chromatic dispersion parameter

$\mathcal{D}$ . . . . . temporal derivative operator

D_P . . . . . PMD parameter

$\mathbf{D}_0$ . . . . . input symbol sequence for NFT-based systems

$\mathbf{D}_L$ . . . . . received symbol sequence for NFT-based systems

E . . . . . normalized signal energy

$e(t,z)$ . . . . . function expressing the noise-like error after linear all-order PMD compensation

$F(t)$ . . . . . inverse Fourier transform of CS

$F_0(t)$ . . . . . input signal in GLM-based signalling method

$F_L(t)$ . . . . . received signal in GLM-based signalling method

$f(|\rho_0|)$ . . . . . function expressing the dependence of noise variance to CS signal amplitude

$G(z,|\rho_0(\lambda_k)|_{k=1}^K)$ function expressing the dependence of perturbation to the fibre length and input symbols

h . . . . . Plank's constant

h_{ss} . . . . . step length of split-step method

h_κ . . . . . distance between subsequent samples in GLM-based signalling method

$\hat{h}$ . . . . . resolution for numerical INFT

j . . . . . imaginary unit

$\boldsymbol{K}(x,y)$ . . . . . Kernel of GLM equations

K_T . . . . . phonon occupancy factor

K . . . . . number of data symbols

$Q(\tau,l)$ . . . . . envelop of optical field (not normalized)

$q(t,z)$ . . . . . normalized envelop of optical field

$q_l(t)$ . . . . . normalized envelop of optical field at fibre length l

l . . . . . fibre length (not normalized)

l_c . . . . . polarization correlation length

L . . . . . total fibre length (not normalized)

L_D . . . . . length normalizing parameter for NLSE

$\mathbf{L}$ . . . . . an operator of Lax pair

$\mathbf{M}$ . . . . . an operator of Lax pair

M . . . . . number of discrete eigenvalues

$n(\omega)$ . . . . . refractive index

$N(\tau, l)$ . . . . . ASE noise (not normalized)

$n(t, z)$ . . . . . normalized ASE noise

N_{ASE} . . . . . ASE noise power spectral density

P . . . . . power constraint

P_ρ . . . . . power of CS in nonlinear spectral domain

P_q . . . . . power of time domain signal

$P(z)$ . . . . . function expressing the dependence of PMD effect to fibre length in single level modulation

R . . . . . bit rate

r . . . . . correction coefficient for signal duration after INFT

t . . . . . normalized time

T_0 . . . . . time normalizing parameter for NLSE

$T(\cdot)$ . . . . . variance normalizing transform

$T_c(A, L)$ . . . . . centre of soliton pulse

$T_g(A)$ . . . . . guard time for soliton communication

$T_w(A)$ . . . . . temporal window for soliton communication

T_w . . . . . average temporal window for soliton communication

$\boldsymbol{v}$ . . . . . eigenfunction vector of Zakharov-Shabat problem

$U(\tau, l)$ . . . . . envelop of optical field in first polarization state (not normalized)

$V(\tau, l)$ . . . . . envelop of optical field in second polarization state (not normalized)

W . . . . . signal bandwidth in Hz (not normalized)

z . . . . . normalized fibre length

Chapter 1

Introduction

1.1 Overview

Optical fibre has been an attractive medium for data transmission since its introduction in 1966 [1]. With enormous engineering advances in manufacturing and system design, optical fibre links are currently like the arteries that connect the world and make the Internet possible. Low loss (less than 0.2 dB/km at 1550 nm) and large bandwidth (7.1 THz for L-band 1565-1625 nm and 4.4 THz for C-band 1530–1565 nm) of optical fibre have made the transmission of huge amounts of information possible through terrestrial and submarine optical fibre links. However, for several decades, the ever increasing demand for data rate have forced scientists and engineers to search for more efficient and novel techniques for data transmission using optical fibre.

The first signal transmission using optical fibre was demonstrated in Chicago's Loop District in 1977 [2, 3]. After that, development of optical fibre links rapidly progressed. For instance, the first fibre-to-home scheme was demonstrated in Japan in 1978, and a commercial system with 45 Mb/s over multimode fibre was available in 1987 [4]. In 1991, practical optical network with 2.5 Gb/s rate was introduced, and 20 Gb/s was achieved through experiment [2]. While only electrically regenerated direct detection was used in previous systems, the availability of optical amplifiers made the unregenerated wavelength division multiplexing (WDM) possible in 1990s. Dispersion-management using consecutive fibre segments with positive and negative dispersions was a breakthrough that led to high data rate WDM systems [5]. From their advent, different dispersion management techniques with various fibres and dispersion maps were developed in a way that dispersion compensating fibres are used in most of the current

optical fibre links. By 2009, practical communication systems could support 40 Gb/s over a single wavelength, and 25 Tb/s rate was demonstrated in experimental setups [2].

Although high data rate transmission was enabled and commercially available, even more data rate was needed due to the rapid growth of demand. Analysis of historical data reveal that the global traffic growth rate is between 25% and 80% per year depending of the network and traffic type [6]. For instance, Youtube upload rate have had an almost constant growth of about 70% per year over the past 10 years, and the total UK broadband demand have increased 60% per year. It is expected that the emerging technologies and applications, such as 4K video streaming, Internet-of-Things, and social media, preserves the continuous growth of demand for data rate. While the growth rate of most of the generation and processing units (e.g., microprocessor performance, wireless interface speed, etc.) have kept up with the global network traffic growth, the transport units, such as WDM capacity, failed to satisfy such demand [6]. For instance, WDM capacity have only increased 20% per year from the year 2000. Therefore, techniques other than WDM with direct detection and On-Off-Keying (OOK) are crucially needed.

Coherent detection enables applying advanced modulation formats and polarization multiplexing. Moreover, the performance is enhanced using digital signal processing and error correction coding using powerful high-speed processors for coherent detection that makes the complex electric field available rather than the optical intensity. High data rates are demonstrated to be achievable with coherent detection, digital signal processing, and different multiplexing techniques in several experiments [7, 8]. For instance, 200 Gb/s systems are now commercially available for regional networks [2]. However, there is an inverse relationship between distance reach and data rate achieved by multi-dimensional advanced modulation formats because of the inevitable amplified spontaneous emission (ASE) noise added during the amplification process. To make it worse, increasing the signal power does not always result in higher signal-to-noise ratio (SNR) due to the nonlinearity of the fibre channel. Unfortunately, the effect of nonlinearity is not easily tractable because it is combined with dispersion and noise. It is now widely believed that the random effects as a result of nonlinear signal and noise interactions are the ultimate barrier for data rate increase in optical fibre channels [9]. Thus, some kind of nonlinearity treatment is essential for future modern

optical fibre communication systems.

Most of the techniques for optical fibre communication channels adopt ideas from the conventional communication methods developed for linear channels (e.g., radio wireless channel), yet the optical fibre is nonlinear. The propagation of light through the fibre is governed by a partial differential equation called nonlinear Shrödinger equation (NLSE), which does not lead to any known input-output relationship for the optical fibre channel. Therefore, except for some low power or short distance scenarios, conventional techniques are not efficient and eventually fail at some longer distances and higher signal power. For instance, the capacity of optical fibre channel may be studied using some empirical approaches [10] or low nonlinearity assumption [11] that does not work for a general optical fibre structure. As a consequence, even with detailed noise modelling of nonlinearity [12] or improved detection [13], the achievable information rates tend to zero at high powers, and the capacity saturates.

As demonstrated in many works, such as [2], there is a gap between the known lower capacity bounds, such as [9], and upper bounds such as [14]. Different signal processing techniques have been developed for increasing the capacity beyond the lower bound and as close as possible to the Shannon capacity [15–17]. As an example, one of the most promising techniques is called digital back propagation (DBP) that uses split-step Fourier method to reverse the effect of propagation [18]. In the absence of noise, all nonlinear signal-signal interactions can be compensated, yet in practical scenarios nonlinear signal-noise interactions limit the performance. Several modifications of DBP have also been proposed which improve the performance [19–21].

All methods developed for nonlinearity treatment, including DBP, fail at some point because either nonlinearity is treated as a noise source or the "distortions" resulted from nonlinearity is tried to be compensated. The novel idea of designing systems based on the nonlinear Fourier transform (NFT) [22, 23], the subject of this thesis, have recently attracted attention among researchers since the nonlinearity is no longer treated as a nuisance [16]. Using NFT, the communication system can be designed embracing the nonlinearity and adapting the signalling techniques to the inherent nonlinearity of the channel. Currently, NFT-based signal processing and information theoretical analysis of optical fibre are regarded as potential

approaches to achieve the true capacity of optical fibre links [24–27]. By applying the NFT, the available degrees of freedom in the time domain (i.e., the optical wave) are transformed into two types of spectra, namely the discrete and continuous spectrum. These spectra evolve linearly through the fibre, in a generalized spectral domain called nonlinear spectral domain, as the time domain signal travels in a nonlinear medium. Thus, the nonlinear channel defined by NLSE, is transformed by NFT to a linear memoryless channel. As a natural consequence, communication systems can be designed in which the mentioned spectra carry the information instead of the time domain signal. This a very attractive approach that opens up a whole new direction for capacity evaluation and signal processing in long-haul optical fibre communication.

Space division multiplexing using multi-core fibres and fibre spatial modes is also regarded as a promising technique for achieving high data rates [6, 28, 29], but nonlinearity still affects the channel along with some additional challenges such as cross-talk in spatial dimension. Spatial multiplexing is also a popular ongoing research route. Another way of tackling the problem is developing more efficient optical fibres and components. For instance, the concept of low noise amplifiers have been developed recently [30]. Hollow core fibres also can potentially provide very low nonlinearity and loss [31]. However, all these routes are still far from practical deployment in optical fibre communication systems.

1.2 Related work

Although the mathematical basis of the nonlinear Fourier transform was developed in 1970s [32–34], it was until 1993 [35] that NFT was first used as a technique for data transmission over the channel defined by NLSE. Indeed, NFT, also known as inverse scattering method, have been used in different areas of mathematics and physics during this time [36]. The NFT is a well-established method for solving the NLSE. Using this method, the continuous spectrum (CS) and discrete spectrum (DS) of input signal are obtained which evolve linearly along the fibre. Unlike Fourier transform in conventional linear systems, the NFT provides two types of spectra in nonlinear spectral domain. The DS corresponds to the solitonic part of time domain signals. Single soliton pulses retain their shapes as a result of perfect cancellation of nonlinearity with dispersion, and, likewise, multi-soliton waveforms possess some *shape*

preserving properties. The CS, however, corresponds to radiation part of time domain signals. In other words, the portion of the optical wave associated to CS is largely affected by the chromatic dispersion and is dispersed in time domain. Because of their nature, these two types of spectra are manifested in different forms in nonlinear spectral domain. A number of discrete points on the positive complex plane, called eigenvalues, together with their corresponding complex *amplitude*, called norming constant construct the DS. On the other hand, the CS is essentially a complex continuous waveform, which is analogous to the frequency domain representation of a signal in conventional linear communication channel. Thus, it is expected that signal processing techniques and communication systems for CS to be realizable through some of the known methods for conventional systems.

In [35], signalling on eigenvalues as part of the DS were nominated as a suitable tool for data communication since they remain unchanged along the fibre in the absence of noise and other perturbations. It should be noted that using eigenvalues for data transmission is closely related to the soliton transmission techniques in which soliton pulses are encoded/decoded in time domain. More recently in a prominent work by Yousefi and Kschischang [24–26], nonlinear frequency division multiplexing (NFDM) was proposed as a general technique for data communication for a nonlinear optical fibre link using NFT. In a NFDM system, data is mapped on continuous and discrete spectra, defined in nonlinear spectral domain. By their work, the NFT regained attention, and different aspects of NFDM have became subjects of numerous research projects recently.

In [24–26], Yousefi and Kschischang reformulated the NFT, derived some of its properties, proposed and examined numerical implementation methods, and studied the concept of NFDM. They concluded that, as shown in the older works [37], if the data is carried by the scattering data (i.e., CS and DS), the corresponding communication channel is free from nonlinearities. In other words, the deterministic distortions caused by the nonlinearity and dispersion are absorbed in the transform itself and the resulting channel is effectively linear. The NFT can be regarded as a generalization of orthogonal frequency division multiplexing (OFDM) for nonlinear optical fibre channel, yet with NFT instead of Fourier transform and different kind of spectra. Despite authors' attempts in [26], an important unanswered questions was that how the channel looks like in presence of perturbations and how much data rate can be achieved?

Many research groups have recently tried to apply this concept to more practical optical fibre communication systems. In the literature, due to lack of closed form mathematical relations for NFT and the complexity of numerical implementation, mainly either CS or DS are solely considered as the data transmission medium.

Mapping the information only on the CS makes it possible to use signalling techniques and modulation format similar to conventional systems such as OFDM because the CS is actually a continuous complex function in nonlinear spectral domain. In a series of papers [38–40], the linear spectrum of a predefined signal (OFDM or Nyquist) was mapped on the CS through inverse nonlinear Fourier transform (INFT), which essentially prevents soliton formation in the time domain signal. This scheme was named nonlinear inverse synthesis (NIS), and the performance of data transmission using NIS was investigated assuming distributed or lumped amplification. It was demonstrated that NIS approach can improve the performance (about 4.5 dB) compared to linear compensation and potentially can lead to high data rates over long distances of fibre. The non-ideal distributed amplification was taken into account in [41], and an experimental work [42] confirmed the feasibility of effective NIS data transmission for transoceanic distances. Multiuser NFDM was recently compared to WDM in [43], and it was demonstrated that achievable rates can be doubled using the proposed nonlinear multiplexing in defocusing case of NLSE. Similar approach was used for focusing case of NLSE in [44]. Most recently in [45], up to 1.3 dB performance gain was reported for NFDM compared to OFDM in an experimental demonstration using only CS and quadrature amplitude modulation (QAM), which confirms the potential benefits of the NFT approach. The capacity of CS channel was studied in [46] using the perturbation theory [47]. The derived model for the CS channel showed absence of inter-symbol interference, and a lower bound of 10.7 bits per symbol was estimated for 2000 km of fibre length and 500 GHz of bandwidth.

Information transmission using the particle-like nature of DS is also an attractive approach. Indeed, before the new research direction powered by NFT, soliton communication has been largely studied in the literature, mainly with OOK modulation and direct detection [48]. Despite relative immunity to dispersion and nonlinear effects, the performance of soliton communication was limited by impairments such as Gordon-Haus effect [49], Raman scattering [50], or acoustic effects [51]. For instance, the famous Gordon-Haus effect refers to

the timing jitter in arrival of soliton pulses as a result of interaction of ASE noise with solitons. Such timing jitter increases for longer fibre or higher power that, consequently, limits the achievable data rates [49]. Numerous attempts have been made to improve the performance and reach distance for soliton communication [48]. Dispersion management, for example, leads to reduced Gordon-Haus jitter as well as other mentioned effects, and successful transmission of high data rates over more than 10000 km of fibre using dispersion managed solitons has been reported [52]. However, fast growth of other high data rate techniques such as WDM caused that the research on soliton-based systems to become scarce [53, 54]. With emergence of NFT-based systems, soliton communication is revived once again but different in format this time. For single soliton communication, using NFT means that data can be mapped on the eigenvalue in positive complex plane and corresponding phase and amplitude of norming constants, which requires coherent detection. The noise model as well as capacity bounds for such system was derived in [55–60]. In these works, however, information rates in bits per second were not presented. Also, some intrinsic limitations, such as dependence of signal bandwidth on the amplitude, were ignored. The more important aspect of using DS is that multi-soliton, also known as multi-eigenvalue, signals can be generated which in effect can increase the spectral efficiency. In [61,62], multi-eigenvalue communication was analysed, in which data is mapped on multiple purely imaginary eigenvalues. The multi-eigenvalue communication was investigated by simulation and experiment, and algorithms were proposed for optimization of bandwidth and pulse duration to maximize the spectral efficiency that led to 3 bit/s/Hz over 2000 km. However, it was observed that spectral broadening can be a limiting issue. In a number of other works general communication system designs, including the modulation on the norming constants, were studied [63–70]. Recently in [71], transmission of 6 bits/symbol at 24 Gbps over 1000 km of fibre was demonstrated by experiment using a single eigenvalue and its corresponding norming constant. In general, it can be concluded from all these research that reliable high data rates can be achieved for long distances of fibre link by signalling on DS provided that an optimized system design is opted.

Other related aspects of NFT-based communication systems include alternative designs based on NFT. For instance, DBP using NFT was proposed in [72], but only the soliton-free defocusing case of NLSE was considered due to complexity. The NFT can also be used at the receiver of current optical fibre links with conventional modulation to design an NFT-based

detector. In such approach, the spectra of the received noisy signal are calculated and the detection is performed based on all possible spectra using minimum distance criteria [64, 73–76]. Periodic NFT (PNFT) was proposed in [77, 78] and studied in [79–81]. Periodic boundary condition are assumed in PNFT rather vanishing boundary conditions in NFT. Similar to OFDM cyclic prefix is added to the signal, which leads to reduced complexity, lower peak-to-average power ratio (PAPR), and more controllable temporal width at the receiver. Recently, attempts have been made to map data on both spectra [82], and it was observed that CS and DS are almost uncorrelated and the performance degradation of CS happens at higher powers (3 dB increase). Some works have also studied polarization multiplexing in NFT-based systems [83–85].

Since the NFT and its inverse are only implemented by numerical methods, development of faster and more efficient numerical algorithms is also an important research direction [43, 66, 86–91]. Detailed review of numerical methods regarding their error and complexity can be found in [25, 27, 77] and references therein. Fast NFT implementation was proposed in [77, 92, 93], and it was demonstrated that CS and DS can be computed using $O(M_s \log^2 M_s)$ and $O(M_s^2)$ flops for M_s sample points. Recently, fast INFT algorithms were also proposed in [94–97], and a complexity of $O(M_s N_d + M_s \log^2 M_s)$ was achieved for M_s sample points and N_d DS points.

1.3 Contributions of the thesis

The CS is the main focus of this thesis, and we aim to study the CS channel comprehensively here. Although some works have studied the CS [39, 40, 42, 43, 46], a fundamental analysis of CS is conducted in this thesis. The capacity analysis, development of signal processing techniques, and investigation of an important impairment for the CS altogether build a complete study of the NFT-based concept using CS. The capacity of the CS is estimated using asymptotic method combined with extensive simulation for the first time, while in [46], perturbation method was used to study the capacity of the CS. Moreover, signal processing techniques are proposed based on the specific noise behaviour of CS, which was lacking in previous studies. Also, the effect of the polarization mode dispersion (PMD) is studied on the single polarization data transmission using the CS that was not considered before. At the end, we

briefly study the capacity of DS part and possibility of simultaneous modulation on both spectra for the first time. It should be noted that only single mode fibre is considered in NFT-related research to date, and long-haul optical fibre communication is the main application of the methods presented in this thesis. Also, device imperfections, higher order dispersions, and other perturbative effects are not included in the definition of NFT and may negatively affect the performance of NFT-based systems. The main contributions of this thesis are presented in four chapters:

Capacity analysis of CS

It is essential to first have a solid model of the CS channel, so that the capacity analysis can be conducted based on it. In order to understand the CS channel, a communication system is defined, in which data symbols are mapped on the CS waveform. Then, the time domain signal is constructed through INFT. The resulted signal is launched into the fibre, and at the receiver the CS, which contains the initial data symbols, is obtained using NFT. Since the effective channel response in nonlinear spectral domain is only a phase shift for the CS, the input-output relation of the channel can be easily defined. However, the properties of noise added to the CS are unknown because the ASE noise induced during the propagation of the signal in time domain is also transformed by NFT. Deriving the statistics of noise in nonlinear spectral domain is not straightforward and novel ways are required for such purpose. The main features of the noise, which play a key role in the capacity of the CS channel, are derived by analysis of the channel for asymptotically long fibres. Such features are confirmed and more details of the noise characteristics are then evaluated by detailed extensive numerical simulations in non-asymptotic scenarios. In brief, it is demonstrated that the effective noise added to the CS signal is almost white, non-Gaussian, and signal-dependent. Having necessary information about the noise, the capacity is estimated numerically utilizing the variance normalizing transform (VNT), which basically transforms the specific noise of the CS channel to an additive Gaussian noise. As an important result, we infer that the capacity saturates at high powers and the capacity achieving distribution is discrete for the CS, which is caused by the signal-dependency of the noise that effectively limits the signalling space. To wrap up the capacity analysis, achievable data rates in bits per second are estimated by taking into account available time-frequency resources, and an approximate closed form equation is

provided.

Signal processing for CS

After providing a detailed capacity analysis of the CS channel, more practical aspects of signalling on the CS are investigated. An important characteristic of the CS channel in NFT-based systems, similar to the traditional optical fibre communication systems, is the data rate limitation due to the temporal broadening as a result of chromatic dispersion. Thus, it is essential to investigate the effect of chromatic dispersion on the system performance because NFT cannot compensate it. Note that NFT is only defined for a fibre channel without any dispersion compensation method in temporal domain. Using a semi-analytic approach, it is demonstrated that improved performance and higher bit rates can be achieved by properly choosing the system parameters and minimizing the effect of dispersion. The other important attribute of the CS channel is its specific noise characteristics in nonlinear spectral domain. By considering such a distinctive feature, we propose three different signalling methods for performance improvement and compare them with the basic method of direct mapping on CS and sampling for detection. We provide analysis in terms of error performance, distance reach, and complexity. It is demonstrated that by adding reasonable amount of complexity to the system, significant performance enhancement can be achieved. For instance, it is shown that a distance of 7100 km can be reached with a 9.6 Gbps rate in only 26 GHz of bandwidth. At the end, a simple general dispersion pre-compensation technique is also proposed. By this digital pre-compensation of the CS and without adding any complexity to the system, up to 100% increase in data rate is obtained.

PMD: An unavoidable impairment

An important fibre impairment which is not included in the master model of optical fibre, the NLSE, is the PMD. In long-haul and high speed fibre links, the impact of PMD can be quite critical. Therefore, for the first time in the literature, the effect of PMD on NFT-based systems is studied. In a nonlinear coherent optical system, the assumption of this thesis, some kind of treatment of PMD is essential since the energy is coupled into the two orthogonal polarization states at the receiver. However, due to the lack of effective PMD compensation methods considering the nonlinearity, the all-order linear PMD compensation method is opted

here. Simulation results show that such PMD compensation is effective and can reverse most of the distortion caused by PMD. Then, the remaining non-compensated effects of PMD on CS, as a consequence of interaction of nonlinearity with PMD, are examined. An analytical framework is provided to better understand the impact of PMD and obtain a corresponding channel model. It is deduced that, apart from the PMD parameter, the fibre length, input power, and instantaneous signal amplitudes are the parameters that determine the perturbation caused by PMD. The analysis is followed by simulation results, which confirm the channel model provided. The main impacts on the CS are a signal-dependent phase shift and a noise-like error. These effects are studied for different modulation formats, fibre lengths, and PMD parameters by simulation. Finally, the combined effects of PMD and ASE noise are evaluated. We infer that, while the effect of ASE noise is still dominant, the PMD can indeed worsen the performance and must be included in the analysis of long haul systems.

Data transmission using the DS part

The CS is only a portion of the available degrees of freedom, and the ultimate capacity of optical fibre can only be realized if all degrees of freedom are exploited efficiently. Since obtaining the capacity of NFT-based systems with optimized signalling on both spectra is cumbersome and subject to future research, we provide the capacity estimate of single soliton communication with amplitude modulation as a complementary contribution to the signalling on CS approach. For the first time, the actual capacity of soliton communication, rather than bounds, is estimated utilizing the VNT. Some practical consideration, such as dependence of signalling space on the available bandwidth, are also included, and it is demonstrated that high data rates can be achieved by considering an appropriate guard time for each soliton pulse. At the end, as an initial step towards an efficient NFT-based system with full utilization of available spectra, the possibility of simultaneous signalling on both spectra is examined. It is demonstrated that independent error-free eigenvalues can be transmitted accompanying the CS, showing a high potential of NFT-based signalling for data transmission in nonlinear regime.

1.4 Outline of the thesis

The remainder of this thesis is organised as follows. In chapter 2, the preliminary background about the optical fibre channel, nonlinear Fourier transform, and numerical methods are presented. The noise model and capacity analysis of the CS channel is provided in chapter 3. The effect of chromatic dispersion, optimization of the channel parameters, efficient signal processing methods, and their corresponding performance are studied in chapter 4, followed by investigation of the effect of PMD in chapter 5. In chapter 6, the capacity of soliton communication with amplitude modulation is estimated, and the feasibility of simultaneous signalling on both spectra is validated. Chapter 7 provides the conclusion of the thesis and future research directions.

1.5 Publications

The outcomes of this thesis are published in the following papers:

Journal papers

- I. Tavakkolnia and M. Safari, "Capacity Analysis of Signaling on the Continuous Spectrum of Nonlinear Optical Fibers," *Journal of Lightwave Technology*, vol.35, no. 11, p. 2086, Jun. 2017. DOI: 10.1109/JLT.2017.2668474
- I. Tavakkolnia and M. Safari, "Signaling on the Continuous Spectrum of Nonlinear Optical Fiber," *Optics Expres*, vol.25, no. 16, p. 18685, Jul. 2017. DOI: 10.1364/OE.25.018685

Conference papers

- I. Tavakkolnia and M. Safari, "Signalling over nonlinear fibre-optic channels by utilizing both solitonic and radiative spectra," in *Proceeding of European Conference on Networks and Communications*, Jun. 2015, pp. 103–107. DOI: 10.1109/EuCNC.2015.7194049
- I. Tavakkolnia and M. Safari, "Dispersion pre-compensation for NFT-based optical fiber communication systems," in *Proceeding of Conference on Lasers and Electro-Optic*, Mar. 2016, Art. no. SM4F4. DOI: 10.1364/CLEO_SI.2016.SM4F.4

- I. Tavakkolnia and M. Safari, "Variance normalizing transform for performance improvement in radio-over-fiber systems," in *Proceeding of European Conference on Networks and Communications*, Jun. 2016, pp. 255–259. DOI: 10.1109/EuCNC.2016.7561043
- I. Tavakkolnia and M. Safari, "Efficient Signalling on the Continuous Spectrum of Nonlinear Optical Fibre," in *Proceeding of European Conference on Lasers and Electro-Optics and the European Quantum Electronics Conference*, Jun. 2017.
- I. Tavakkolnia and M. Safari, "Effect of PMD on the Continuous Spectrum of Nonlinear Optical Fibre," in *Proceeding of European Conference on Lasers and Electro-Optics and the European Quantum Electronics Conference*, Jun. 2017.

Chapter 2

Background

In this chapter, background subjects are briefly presented. Dominant physical phenomena in the fibre are reviewed, and the fibre channel model is presented. Next, nonlinear Fourier transform (NFT) is introduced, followed by numerical implementation of fibre channel and NFT. More details can be found in [27, 36, 98–100].

2.1 Optical fibre channel

History of optical fibre communication begins from 1966 when optical fibre was introduced as a medium for propagation of light originated from laser [1]. However, optical fibres with relatively low loss (lower than 20 dB/km) were introduced in 1970 [101], and the first signal transmission over optical fibre was carried out in 1977 [2, 3]. In the 1980s, optical fibre transmission lines were gradually commercialized and replaced coper wires and satellite communication. The first submarine optical fibre cable was used in 1984 for telephone traffic. Research and development on optical fibre systems has since continued in a way that optical fibre is now the only medium capable of supporting huge demands for data rate. In the following subsections basics of optical fibre and corresponding components are reviewed.

2.1.1 Optical fibre structure

Optical fibre is simply a cylindrical glass core covered by a cladding layer with smaller refractive index. This allows the light wave to travel through the fibre for long distances with low loss, typically 0.2 dB/km at wavelength 1550 nm for current single mode optical fibres. The cross-section of a typical step-index fibre is schematically shown in Figure 2.1. Step-index fibre refers to a fibre with two different refractive indices for core and cladding

in comparison to the graded-index fibre with gradual change of refractive index from core to cladding. Various refractive indices are obtained using different dopants in the silica glass at the fabrication process.

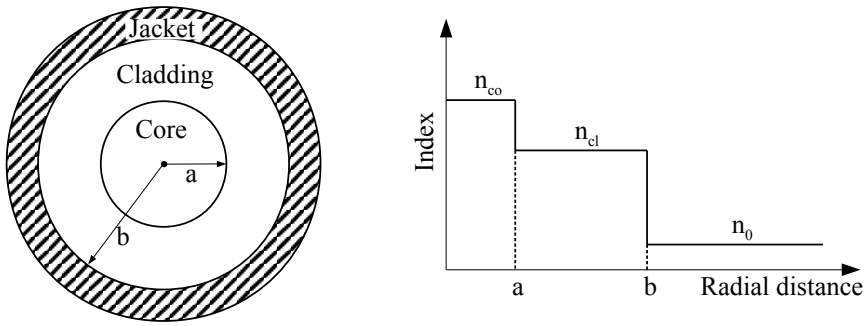

Figure 2.1: Cross-section of a step-index fibre and its refractive index profile.

The structure of optical fibre and the difference in refractive indices of core and cladding cause the light to be confined in the fibre by the total internal reflection from the cladding while travelling through the fibre. The difference of refractive indices between core and cladding together with core radius determines the number of modes the fibre can support. An optical fibre that only supports a single mode (fundamental mode) is called single-mode fibre (SMF). The core and cladding radius for SMFs are typically about 25 and 62.5 μm [98]. The specific structure of optical fibre results in several physical phenomena, the most important of which are explained briefly as follows.

2.1.2 Loss

Different factors in an optical fibre contribute to making the fibre a lossy medium. In silica glass fibre the main loss mechanism is Rayleigh scattering, which originates from light scattering in all direction due to the local fluctuations of refractive index as a results of density variation of silica [98]. Rayleigh scattering is inversely proportional to the fourth power of wavelength. Another mechanism is the material absorption caused by impurities left during the fabrication process such as OH ion.

The loss factor α is defined as the amount of power lost during the propagation of light through the fibre. It is usually expressed in units of dB/km. Fibre loss depends on the wavelength, and the minimum fibre loss is about 0.2 dB/km at wavelength 1550 nm. For long distances

of fibre links, amplifiers are used in order to compensate the loss and provide sufficient power at receivers. The most common type of optical amplifier (i.e., Erbium-doped fibre amplifiers) also work at around 1550 nm wavelength.

2.1.3 Chromatic dispersion

Dependence of the refractive index $n(\omega)$ in an optical fibre to the frequency is referred to as chromatic dispersion. At each optical frequency ω, the response of dielectric medium to incident electromagnetic wave is different compared to another frequency. As a consequence, the pulse broadens in time-domain because different frequency components travel at different speeds. This can be represented mathematically by Taylor series expansion of the mode-propagation constant $\beta(\omega)$ in the carrier frequency ω_0 [98]

$$\beta(\omega) = n(\omega)\frac{\omega}{c} = \beta_0 + \beta_1(\omega - \omega_0) + \frac{1}{2}\beta_2(\omega - \omega_0)^2 + \cdots ,$$

where c is the speed of light in vacuum and β_i is the ith derivative of $\beta(\omega)$ at the carrier frequency. Group velocity v_g, equal to $1/\beta_1$, is the speed of the envelope of optical wave travelling along the fibre. Dispersion of the envelope is determined by β_2, called group velocity dispersion (GVD) parameter. The chromatic dispersion parameter, which is commonly used in the literature, can be expressed as [98]

$$D = \frac{-\omega^2}{2\pi c}\beta_2.$$

Apart from frequency-dependence of refractive index of the core, the structure of the fibre also contributes to the dispersion by reducing the effective refractive index. This is referred to as waveguide dispersion. However, this usually has negligible effects except around zero-dispersion wavelength. Waveguide dispersion slightly increases the zero-dispersion wavelength. Higher order dispersion, such as third-order dispersion parameter β_3 should be included for ultra-short pulses or near the zero-dispersion wavelength where β_2 is small.

Dispersion is an important factor in optical fibre communication in both linear and nonlinear regime. Chromatic dispersion causes the amount of information received in a period of time to be limited due to the induced broadening of waveforms. For instance, this effect can be

investigated simply by considering a single Gaussian pulse in linear scenario [98]. If a Gaussian pulse with root-mean-square (RMS) value of initial temporal width of ΔT_0 travels a distance of L the received temporal width ΔT_L is equal to [98]

$$\Delta T_L^2 = \Delta T_0^2 + \left(\frac{\beta_2 L}{2\Delta T_0}\right)^2.$$

It can be seen that ΔT_L can be minimized by choosing $\Delta T_0 = \sqrt{|\beta_2|L/2}$. The limit of bit rate R can be estimated for on-off keying (OOK) modulation assuming 95% of the pulse remaining in the bit slot $T_B = 1/R$. The corresponding criterion would be $4\Delta T_L < T_B$, and thus the limitation on the bit rate R is expressed as [98]

$$4R\sqrt{|\beta_2|L} < 1.$$

For example, the bit rate is limited to about 1 Gbps for a 1000 km fibre link with $D = 16\ \mathrm{ps}/(\mathrm{km}\cdot\mathrm{nm})$ without any dispersion compensation or other limiting effect.

Different methods are used to compensate the effect of dispersion in optical fibre links. Dispersion-shifted fibre was developed to eliminate the large amount of dispersion in 1550 nm in Standard Single Mode Fibre (SSMF). However, nonlinear effects are high for dispersion-shifted fibres in such way that it was almost impossible to use WDM [2]. Dispersion compensating fibre was introduced in 1993 which consisted of segments of fibres with positive and negative dispersions. This led to zero dispersion overall, but local dispersion was high enough to mitigate the nonlinear effects. Dispersion effects can also be compensated using digital signal processing which usually requires coherent detection. It should be noted that dispersion is a linear effect and can be treated using relatively simple methods. However, it is no longer straightforward to model and analyse the dispersion effects when nonlinearity is not negligible, for instance, in advanced multi-level modulation formats.

2.1.4 Polarization mode dispersion

Even a single-mode fibre can support two degenerate modes in orthogonal polarization directions. As long as the fibre cross section is a perfect circle, the field excited in any of the orthogonal polarizations would not couple into the other mode [98]. During the manufacturing

process or due to the environmental stress the fibre deviates from the ideal cylindrical symmetry, and, consequently, the two orthogonal modes are no longer degenerate meaning that the refractive index for the two polarization states, shown by n_x and n_y, are no longer equal. This is called birefringence.

The parameter $B = |n_x - n_y|$ is used for evaluating the strength of birefringence. The two orthogonally polarized modes exchange their power periodically over the beat length $L_B = 2\pi c/\omega B$. An input signal with components in both polarizations broadens as it propagates along the fibre due to different speeds of two polarization components. This phenomena is called polarization-mode dispersion (PMD).

More importantly, in standard fibres, the birefringence randomly changes along the fibre because of some random effects, such as anisotropic environmental stresses. Therefore, the state of polarization changes randomly for a signal launched into the fibre, and a random broadening effect is observed. The RMS value of time delay between two polarization components ΔT_P is used for identifying PMD in standard optical fibres, which can be related to the PMD parameter D_P as [99]

$$< (\Delta T_P)^2 > \equiv D_P \sqrt{L},$$

The typical values of D_p are about a few tenth of $\mathrm{ps}/\sqrt{\mathrm{km}}$. Although the PMD-induced brodening has a $\sqrt{L}$ dependence, it becomes important in high data-rate optical communication, where it can not be neglected compared to the broadening due to chromatic dispersion.

2.1.5 Nonlinearity

Several nonlinear effects can be observed in an optical fibre due to the nonlinear response of dielectric (i.e., silica glass) to intense electromagnetic fields. The specific geometry of the wave guide also plays an important role in the significance of nonlinearity in optical fibres. The main origin of nonlinear effects in the fibre is the dependence of refractive index to the intensity of light, referred to as nonlinear refraction. The effective refractive index can be expressed as

$$\tilde{n}(\omega, E) = n(\omega) + n_2 |E|^2,$$

where $n(\omega)$ is the linear part of refractive index, E is the electromagnetic field, and n_2 is the nonlinear-index coefficient with typical value about 2.6×10^{-20} m^2/W. In spite of the fact that the nonlinear part of the refractive index is relatively small, the resulting nonlinear effects cannot be neglected in modern long-haul optical fibre communication systems. The nonlinearity parameter of the optical fibre is defined as

$$\gamma = \frac{\omega_0 n_2}{c A_{eff}},$$

where A_{eff} is the effective mode area of the fibre.

The dependence of the refractive index to optical intensity causes self-phase modulation (SPM) and cross-phase modulation (XPM). These effects, which lead to phase shift in time-domain and spectral broadening of the signal during propagating in the fibre, are widely studied in the field of optical fibre communication [15, 98]. The SPM and XPM, originated from intensity dependence of refractive index, are associated with the third-order nonlinear susceptibility. The SPM is generated from the in-band signal contributions, while XPM includes the nonlinear interference from out-of-band frequencies. Thus, the considered system model (e.g., the available bandwidth) is critical in analysis of nonlinearity that determines the included nonlinear contributions.

Another nonlinear effect also related to the third-order nonlinear susceptibility is called four-wave mixing (FWM). A fourth frequency component is generated by FWM, when three frequency components co-propagate in the fibre at the same time. Other nonlinear effects include simulated Raman scattering and simulated Brillouin scattering. If peak power of the signal is large enough, energy may be transferred to a new wavelength, and the energy in the new wavelength may interact with the signal through XPM. All nonlinear effects (except the simulated scattering effects), chromatic dispersion, and loss can be included in a single evolution equation that is the main model for analysis of fibre channel. Such evolution equation is introduced in the following subsection.

2.1.6 Nonlinear Schrödinger equation

The propagation of signal through the fibre can be described by the nonlinear Schrödinger equation (NLSE), which is widely used in the field of optical fibre communication and is tested in several experiments [98]. The NLSE can be derived starting from Maxwell's equation. The detailed derivation of NLSE can be found in several books and research papers such as [98] and [102]. Several major assumptions are needed in derivation of NLSE, which are presented here:

- The optical field has a slowly varying envelope. This corresponds to the signal bandwidth to be very small compared to the carrier frequency, or in other words, the envelope of the wave varies slowly in time and space compared to the period or wavelength. This is a valid assumption for pulses wider than 1 ps (calculated for carrier frequency 193.5 THz).
- Since nonlinearity is relatively small in silica glass, the nonlinear term is treated as a small perturbation compared to the linear terms. Also, power is small enough so that higher order nonlinearities, such as simulated scattering effects, can be ignored.
- It is assumed that PMD is negligible, and the initial field is polarized in one of the orthogonal polarization modes. Therefore, NLSE in its scaler form is valid. Unless polarization maintaining fibre are used, this assumption is generally not valid, particularly for high speed communication and long length of standard optical fibre, in which case coupled nonlinear Schrödinger equation should be used. This is discussed in chapter 5.

For the slowly varying envelope $Q \equiv Q(\tau, l)$ at carrier frequency ω_0, the NLSE can be expressed as

$$\frac{\partial Q}{\partial l} = -j\frac{\beta_2}{2}\frac{\partial^2 Q}{\partial \tau^2} + j\gamma Q|Q|^2 - \frac{\alpha}{2}Q \tag{2.1}$$

where $j \triangleq \sqrt{-1}$. In (2.1), a change of variable is used as $\tau = T - \beta_1 l$ for time T, which refers to a moving frame with the pulse at the group velocity v_g. The first term in the right hand side of (2.1) represents the dominant form of chromatic dispersion. The NLSE with $\beta_2 < 0$ is called focusing or anomalous that is the case considered in this thesis, and defocusing or normal case refers to $\beta_2 > 0$. In the focusing regime, high frequency components of optical pulse

travel faster than low-frequency components of the same pulse. Also, Silica fibre, which is mainly used in telecommunication, has focusing dispersion in wavelength 1550 nm. Moreover, soliton propagation is only possible in focusing case when the dispersion is compensated by nonlinearity, and the pulse shape is preserved. The second term in the right hand side of (2.1) is responsible for the nonlinearity, and the last term represents the fibre loss. Typical values for the parameters of NLSE at 1550 nm are $\alpha = 0.046$ km^{-1}, $\beta_2 = 22 \times 10^{-24}$ s^2/km, and $\gamma = 1.27$ W^{-1}km^{-1} [24].

Despite applying the aforementioned assumptions, the NLSE explains the behaviour of most of the optical fibre communication systems in typical data rate, fibre types, and transmission modes. Since higher order dispersion and nonlinearity are not included in NLSE, in some rare cases, modified version of the NLSE or entirely different modelling techniques may be required.

2.1.7 Optical amplification

As stated earlier, optical fibre is a lossy medium. Thus, amplification is necessary, particularly for long fibre links. Before commercialization of optical amplifiers, electrical amplification was used in optoelectronic repeaters [99]. From 1995, after development of more complex systems, such as WDM, optical amplifier became an indispensable part of fibre communication links. Optical signal is amplified periodically over distances of tens of kilometres in a way that enough optical power is available at the receiver for detection. There are two types of optical amplification: lumped amplification commonly using Erbium-doped fibre amplifiers (EDFA) and distributed amplification mainly using Raman amplifiers.

The optical amplification is realized through photon emission as a results of transition of matter elements (e.g., erbium ions) from an exited energy estate to a lower energy state. The required energy for simulation may come from an external source such as laser. As a result, the emitted photons are identical in phase, frequency, and direction with the external photons. This is the basic principle of optical amplification. However, photon emission may occur spontaneously without any external simulation in random direction and phase. This spontaneous emission is also amplified in the same way as the signal photons, and is regarded as a noise, called amplified

spontaneous emission (ASE) noise. The NLSE with optical amplification is expressed as

$$\frac{\partial Q}{\partial l} = -j\frac{\beta_2}{2}\frac{\partial^2 Q}{\partial \tau^2} + j\gamma Q|Q|^2 + \left(g_A(l) - \frac{\alpha}{2}\right)Q + N, \tag{2.2}$$

where $g_A(l)$ is the gain coefficient, which depends on the type of amplification. The term $N \equiv N(l,\tau)$ represents the ASE noise. As demonstrated in [103, 104], the ASE noise can be modelled as a circularly symmetric Gaussian process, fully characterized by its autocorrelation

$$\mathsf{E}\{N(l,\tau)N^*(l',\tau')\} = \frac{N_{\mathrm{ASE}}}{L}\delta(l-l')\delta(\tau-\tau'), \tag{2.3}$$

where $\delta(\cdot)$ is the Dirac delta function, and the power spectral density (PSD) after length L, denoted by N_{ASE}, is determined based on the type of the amplification.

EDFA

A relatively short length of fibre ($\sim$ 10 m) doped with an element, such as Erbium ions, can serve as an amplifier if it is pumped at a suitable wavelength. Semiconductor lasers operating at near 0.98 or 1.48 μm are used for pumping in EDFAs. Periodical lumped amplification is performed by placing EDFAs at fibre spans of typically between 40 and 120 km (corresponding to about 8 and 24 dB loss per span) [9]. The length of each span is determined by different system parameters and requirements. The PSD of noise for a fibre length L consisted of N_A fibre spans is given by

$$N_{\mathrm{ASE}}^{\mathrm{EDFA}} = N_A h\nu_0 n_{sp}(G-1),$$

where $G = e^{\alpha l_{sp}}$ is the amplifier gain for fibre span $l_{sp} = L/N_A$. Parameters h and ν_0 are respectively the Planck's constant and the carrier frequency of the signal being amplified, so that $h\nu_0$ corresponds the average photon energy. Also, the parameter $n_{sp} \leq 1$ is the spontaneous emission factor. Noise figure $\mathrm{NF} = 10\log_{10}(\text{input SNR} \,/\, \text{output SNR})$ for EDFAs is given by

$$\mathrm{NF} = 2n_{sp}(1-\frac{1}{G}) + \frac{1}{G},$$

which shows that NF for EDFAs is generally larger than 3dB (NF$\approx$ 3dB for $n_{sp} = 1$ and $G >> 1$).

Raman amplifier

In distributed amplification, simulated Raman scatering in fibre itself is used for amplification. Pump lasers are periodically placed along the link for power injection. Through several fibre couplers, placed along the fibre link, the pump and signal beams with different carrier frequencies are injected into the fibre. The energy is transferred from pump to the signal through simulated Raman scattering process, which happens continuously along the fibre. Raman amplifiers can provide better signal-to-noise ratio compared to EDFAs by maintaining the signal power along the fibre [9]. The effective noise figure in a Raman amplifier, removing the effect of passive fibre $\exp(-\alpha L)$, can be less than 1 (negative in dB), which makes it attractive for optical fibre communication [99]. Compared to the lumped amplification, in which the fibre loss is compensated at the end of the fibre section, the distributed Raman amplification compensates the loss during the transmission that results in less noise and improved SNR. However, the deployment of Raman amplifiers in commercial optical fibre communication systems is still in progress due to a few practical issues such as laser safety and power handling of optical connectors [2].

Similar to EDFAs, spontaneous Raman scattering adds a noise to the amplified signal during the amplification process. The PSD for Raman amplifiers can be obtained similar to EDFAs using the limit $l_{sp} \to 0$ and is given by

$$N_{\mathrm{ASE}} = \alpha L h \nu_0 K_T, \tag{2.4}$$

where K_T is the phonon occupancy factor approximately equal to 1.13 [9].

Considering ideal distributed amplification using Raman amplifiers allows assuming $g_A(l) = \alpha$ in (2.2). Such scenario is called ideal distributed amplification. Near ideal distributed amplification is demonstrated by experiment in [105, 106]. The NLSE considering ideal distributed amplification is given by

$$\frac{\partial Q}{\partial l} = -j\frac{\beta_2}{2}\frac{\partial^2 Q}{\partial \tau^2} + j\gamma Q|Q|^2 + N(l,\tau), \tag{2.5}$$

where the PSD of noise $N(l,\tau)$ is given in (2.4).

2.2 Nonlinear Fourier transform

In this section, the nonlinear Fourier transform (NFT) is introduced briefly as it is needed throughout the thesis. More details can be found in numerous book and papers such as [24–27, 36, 100].

2.2.1 Brief History of inverse scattering method

The first documented observation of solitary waves was reported in 1834, when J. Scott Russell followed the "the great wave of translation" along a canal in Edinburgh, Scotland [107]. He described his observation as:

> "*I was observing the motion of a boat which was rapidly drawn along a narrow channel by a pair of horses, when the boat suddenly stopped - not so the mass of water in the channel which it had put in motion; it accumulated round the prow of the vessel in a state of violent agitation, then suddenly leaving it behind, rolled forward with great velocity, assuming the form of a large solitary elevation, a rounded, smooth and well-defined heap of water, which continued its course along the channel apparently without change of form or diminution of speed. I followed it on horseback, and overtook it still rolling on at a rate of some eight or nine miles an hour, preserving its original figure some thirty feet long and a foot to a foot and a half in height. Its height gradually diminished, and after a chase of one or two miles I lost it in the windings of the channel. Such, in the month of August 1834, was my first chance interview with that singular and beautiful phenomenon which I have called the Wave of Translation*". [107]

The mathematical formulation of Russell's observation, currently known as Korteweg-de Vries (KdV) equation, was derived in 1871 [108,109]. More importantly, it was discovered that many other physical phenomena, such as lattice dynamics of Fermi-Pasta-Ulam [110], can also be modelled by the KdV equation [111]. Zabusky and Kruskal named the solitary wave solution of KdV equation "soliton" which possessed a particle-like characteristic. Solitons could pass through each other and retain their shape and velocity. After Zabusky and Kruskal's work until now, the term soliton refers to any nonlinear wave which retains its initial shape after

an arbitrary local disturbance [36]. Searching for a method for solving KdV equation led to discovering interesting mathematical theory by Gardner, Greene, Kruskal and Miura [32, 33], which later led to the NFT.

The KdV equation is expressed as

$$\frac{\partial q}{\partial z} = q\frac{\partial q}{\partial t} + \frac{\partial^3 q}{\partial t^3}, \tag{2.6}$$

for a real-valued pulse $q \equiv q(t, z)$ as a function of time t and distance z. Gardner, Greene, Kruskal and Miura found that the solution of (2.6), fits as the external potential term for linear Schrödinger equation

$$i\frac{\partial u}{\partial z} = \frac{\partial^2 u}{\partial t^2} + qu, \tag{2.7}$$

provided that the eigenvalues of the linear Schrödinger operator remain constant respect to z. This observation can be regarded as a linearization method for a nonlinear partial differential equation (PDE) such as KdV.

It was not clear whether or not such method, which perfectly worked for KdV, can be applied to any other PDE. In a remarkable work by Lax [112], it was mathematically proved that integrable nonlinear PDEs can be related to some linear operators (Lax pair) with invariant eigenvalue. If Lax pair for a nonlinear PDE are found by satisfying the compatibility condition between the linear operators, that nonlinear PDE can be solved in a way similar to the KdV equation [33]. However, the problem was that one should mainly guess Lax pair for a certain nonlinear PDE. In 1972, Zakharov and Shabat found Lax pair associated with the NLSE, and subsequently provided a mathematical technique for solving it. Manakov extended the approach to a pair of coupled NLSE [113]. It should be noted that, apart from nonlinear optical fibre, NLSE may appear in several other fields [100], such as deep water waves [114], plasma physics [115], magneto-static spin [116], and other nonlinear media [117]. Ablowitz, Kaup, Newell and Segur developed similar method for integrable PDEs, and called the more general method inverse scattering transform (IST) [37, 118]. As mentioned in [36, 100] by Ablowitz et al., the IST can be regarded as a nonlinear version of Fourier transform or in other words nonlinear Fourier transform.

The NFT framework provides the opportunity to solve the evolution of an initial value

according to an integrable nonlinear PDE in the *nonlinear spectral domain* (sometimes referred as nonlinear frequency domain). Recall that the linear spectrum is defined by ordinary Fourier transform. In contrast, the nonlinear spectra or the *scattering data* are found by NFT, for which all the nonlinearity and dispersion turn into a simple exponential term in nonlinear spectral domain. Thus, the solution of a nonlinear evolution equation (e.g., NLSE), having the initial value, can be found following the IST by three steps:

- The forward transform: Evaluation of the scattering data, which are independent of time, from the given initial value (e.g., input optical signal).
- The evolution: Transmission of the scattering data in their corresponding domain (i.e., nonlinear frequency domain) according to simple solvable evolution equations.
- The inverse transform: Evaluation of the evolved time-domain solution based on the evolved scattering data.

2.2.2 Evolution equation and Lax pair

The NLSE (2.5), governing the propagation of the complex envelop of optical wave in the fibre, can be normalized as

$$j\frac{\partial q(t,z)}{\partial z} = \frac{\partial^2 q(t,z)}{\partial t^2} + 2|q(t,z)|^2 q(t,z) + n(t,z), \tag{2.8}$$

by normalization rules

$$q = \sqrt{\gamma L_D}Q, \quad z = \frac{l}{2L_D}, \quad t = \frac{\tau}{T_0}, \tag{2.9}$$

where $L_D = T_0^2/|\beta_2|$, and the normalizing parameters T_0 can be chosen independent of other parameters. For isolated pulses, T_0 and L_D indicate the pulse width in time domain and dispersion length. For more complex signal shapes, these normalization parameters do not correspond to the same physical attributes, but they can be modified to control the physical characteristics of the system such as bandwidth, temporal duration, or induced dispersion. Therefore, the autocorrelation of the normalized noise can be described as

$$\mathsf{E}[n(t,z)n^*(t',z')] = \sigma^2\delta(t-t')\delta(z-z'), \tag{2.10}$$

where based on (2.9)

$$\sigma^2 = \frac{N_{ASE}}{L}\frac{2\gamma L_D^2}{T_0}. \tag{2.11}$$

In the noise-free scenario ($n \equiv 0$ in (2.8)), an evolution equation, basically a nonlinear PDE, can be defined as

$$\frac{\partial q(t,z)}{\partial z} = K(q), \tag{2.12}$$

where $K(q)$ depends on q and its temporal derivatives respect to t.

Based on Lax formulation, a linear eigenvalue problem and another associated linear problem should be found for a nonlinear evolution equation, such as (2.12), so that IST can be applied. The eigenvalue problem is defined for the operator $\mathbf{L} \equiv \mathbf{L}(z)$, a square matrix dependent to z, as

$$\mathbf{L}\boldsymbol{v} = \lambda \boldsymbol{v}, \tag{2.13}$$

which can be solved to determine the eigenfunctions that depend on the spectral parameter λ (eigenvalue) and temporal parameter t. The eigenvalues of the linear operator $\mathbf{L}(z)$ are invariant during the evolution in z, and such a linear operator is called isospectral. Scattering data are then evaluated using the eigenfunctions

$$\boldsymbol{v}(t,\lambda) = \begin{pmatrix} v_1(t,\lambda) \\ v_2(t,\lambda) \end{pmatrix}.$$

The evolution of the scattering data is determined by a second linear problem defined for operator $\mathbf{M}$ as

$$\frac{\mathrm{d}\boldsymbol{v}}{\mathrm{d}z} = \mathbf{M}\boldsymbol{v}. \tag{2.14}$$

Taking the derivative of (2.13), using $\mathrm{d}\lambda/\mathrm{d}z = 0$, and substituting in (2.14), the compatibility condition for diagonalizable operator $\mathbf{L}$ and some operator $\mathbf{M}$ is determined as

$$\frac{\mathrm{d}\mathbf{L}}{\mathrm{d}z} = [\mathbf{M}, \mathbf{L}], \tag{2.15}$$

where $[\mathbf{M}, \mathbf{L}] \triangleq \mathbf{ML} - \mathbf{LM}$ is the commutator bracket. The equation (2.15) can be used to construct a nonlinear evolution equation as in (2.12). Once the linear problems (2.13) and

(2.14) are found the IST can be used for solving the nonlinear evolution equation. For instance, the KdV equation (2.6), can be constructed by

$$\mathbf{L} = \mathcal{D}^2 + q$$

$$\mathbf{M} = \frac{3}{2}\mathcal{D}^3 + \frac{1}{2}(\mathcal{D}q + q\mathcal{D}),$$

where $\mathcal{D} = \partial/\partial t$ is the temporal derivative operator. The Lax pair for NLSE are given by [115]

$$\mathbf{L} = j \begin{bmatrix} \mathcal{D} & q \\ -q^* & -\mathcal{D} \end{bmatrix}, \tag{2.16a}$$

$$\mathbf{M} = \begin{bmatrix} 2j\lambda^2 - j|q|^2 & -2\lambda q - jq_t \\ 2\lambda q^* - jq_t & -2j\lambda^2 + j|q|^2 \end{bmatrix}. \tag{2.16b}$$

2.2.3 (Forward) nonlinear Fourier transform

The Zakharov-Shabat eigenvalue problem is derived by differentiating both sides of (2.13) as

$$\frac{\partial \boldsymbol{v}(t,\lambda)}{\partial t} = \begin{bmatrix} -j\lambda & q(t,z) \\ -q^*(t,z) & j\lambda \end{bmatrix} \boldsymbol{v}(t,\lambda), \tag{2.17}$$

which in some references is refereed to as AKNS (Ablowitz, Kaup, Newell, and Segur) or ZS/AKNS eigenvalue problem. It should be noted that the equality $\partial^2\boldsymbol{v}/\partial t\partial z = \partial^2\boldsymbol{v}/\partial z\partial t$ leads to the evolution equation (2.12) for q. We assume that $q \to 0$ rapidly as $|t| \to \infty$, and $q \in L_1(\mathbb{R})$. Thus, the integral

$$\mathcal{Q}(x) = \int_{-\infty}^{x} |q(y)|dy$$

exists, and also, the Neumann series of the Volterra integral equations converge in the upper half complex plan $\Im\{\lambda\} > 0$ [36].

The NFT is defined based on (2.17), and the evolution of the scattering data is derived using (2.14). There are infinite number of solutions to (2.17) for $\lambda \in \mathbb{C}$ associated with all possible boundary constitutions. Considering the vanishing boundary condition $q \to 0$ rapidly as $t \to$

$\pm\infty$, the problem (2.17) reduces to

$$\frac{\partial \boldsymbol{v}(t,\lambda)}{\partial t} = \begin{bmatrix} -j\lambda & 0 \\ 0 & j\lambda \end{bmatrix} \boldsymbol{v}(t,\lambda),$$

for large t. Thus, the boundary conditions of the eigenfunctions, solutions of above equation, are defined as

$$\boldsymbol{\psi}_\infty = \begin{pmatrix} 1 \\ 0 \end{pmatrix} e^{-j\lambda t}, \quad \tilde{\boldsymbol{\psi}}_\infty = \begin{pmatrix} 0 \\ -1 \end{pmatrix} e^{+j\lambda t}, \quad \text{as } t \to -\infty, \tag{2.18}$$

$$\boldsymbol{\phi}_\infty = \begin{pmatrix} 0 \\ 1 \end{pmatrix} e^{+j\lambda t}, \quad \tilde{\boldsymbol{\phi}}_\infty = \begin{pmatrix} 1 \\ 0 \end{pmatrix} e^{-j\lambda t}, \quad \text{as } t \to +\infty, \tag{2.19}$$

where $\boldsymbol{\psi}(t,\lambda) = (\psi_1(t,\lambda), \psi_2(t,\lambda))^T$ and $\boldsymbol{\phi}(t,\lambda) = (\phi_1(t,\lambda), \phi_2(t,\lambda))^T$ are the solutions for all $t \in \mathbb{R}$. Assume $\boldsymbol{v}(t,\lambda)$ and $\boldsymbol{u}(t,\lambda)$ (both 2×1 vectors) be two solutions of (2.17), the Wronskian of $\boldsymbol{u}$ and $\boldsymbol{v}$ defined as

$$W(\boldsymbol{u},\boldsymbol{v}) = u_1 v_2 - u_2 v_1,$$

is constant and independent of t. If $W(\boldsymbol{u},\boldsymbol{v}) \neq 0$, then $\boldsymbol{v}$ and $\boldsymbol{u}$ are linearly independent and form a basis of the subspace formed by all solutions. For the boundary values (2.18) and (2.19), we have

$$W(\boldsymbol{\psi}_\infty, \tilde{\boldsymbol{\psi}}_\infty) = 1, \quad W(\boldsymbol{\phi}_\infty, \tilde{\boldsymbol{\phi}}_\infty) = -1,$$

and thus we can write

$$\boldsymbol{\psi}(t,\lambda) = a(\lambda)\tilde{\boldsymbol{\phi}}(t,\lambda) + b(\lambda)\boldsymbol{\phi}(t,\lambda), \tag{2.20a}$$

$$\tilde{\boldsymbol{\phi}}(t,\lambda) = b^*(\lambda^*)\tilde{\boldsymbol{\phi}}(t,\lambda) - a^*(\lambda^*)\boldsymbol{\phi}(t,\lambda), \tag{2.20b}$$

where $a(\lambda) = W(\boldsymbol{\psi}(t,\lambda), \boldsymbol{\phi}(t,\lambda))$ and $b(\lambda) = -W(\boldsymbol{\psi}(t,\lambda), \tilde{\boldsymbol{\phi}}(t,\lambda))$ are called nonlinear Fourier coefficients. Since $q \in L_1(\mathbb{R})$ (i.e., absolutely integrable) $a(\lambda)$ is analytical in the upper half of complex plane. Also, for analyticity of $a(\lambda)$ on real axis $\Im\{\lambda\} = 0$, it is needed that

$$|q(t,0)| \leq c_1 e^{-2c_2|t|},$$

for sum constants c_1 and $c_2 > 0$. Then, $a(\lambda)$ is analytical for $\Im\{\lambda\} > -c_2$.

The Zakharov-Shabat eigenvalue problem has two types of spectra (i.e., scattering data). For sufficiently large values of $|q|$, (2.17) may have discrete eigenvalues in upper half complex plane $\mathbb{C}^+$, which are zeros of $a(\lambda)$. The discrete eigenvalues are shown by $\lambda_m \in \mathbb{C}^+$ for $m = 1, 2, \cdots, M$, where M is the number of eigenvalues. For discrete eigenvalues, (2.20a) leads to $\boldsymbol{\psi} = b(\lambda_m)\boldsymbol{\phi}$, and the ratio

$$C_m = \frac{b(\lambda_m)}{a'(\lambda_m)}, \tag{2.21}$$

is referred to as norming constants. Here, $a'(\lambda_m)$ is the derivative with respect to λ at $\lambda = \lambda_m$. The continuous spectrum is defined on the real axis $\lambda \in \mathbb{R}$ as

$$\rho(\lambda) = \frac{b(\lambda)}{a(\lambda)}, \tag{2.22}$$

where the spectral coefficients are given by

$$a(\lambda) = \lim_{t\to\infty} \psi_1(t, \lambda)e^{j\lambda t}, \tag{2.23a}$$

$$b(\lambda) = \lim_{t\to\infty} \psi_2(t, \lambda)e^{-j\lambda t}. \tag{2.23b}$$

Note that discrete eigenvalues can only happen for the focusing case considered in this thesis. In order to have an estimation on the condition for which the eigenvalues emerge, one can use the asymptotic expansion of the scattering coefficients. Without presenting the details, it can be shown that [36]

$$|a(\lambda) - 1| \leq I_0(2\mathcal{Q}_0(\infty)) - 1,$$

where $I_0(\cdot)$ is the modified Bessel function of the first kind. Thus, if $\mathcal{Q}_0^2(\infty) < 0.817$ there are no discrete eigenvalues (i.e., zeros of $a(\lambda)$).

The scattering data, needed for IST application, are $\{\rho(\lambda), \{\lambda_m\}_{m=1}^M, \{C_m\}_{m=1}^M\}$ for $i = 1, \cdots, M$ which are defined in the so-called nonlinear spectral domain. In this thesis the term nonlinear frequency refers to λ for the continuous spectrum. When the scattering data are available the evolution in the nonlinear spectral domain can be derived using the linear

evolution equation (2.14).

2.2.4 Evolution of scattering data

For $t \to \pm\infty$, the equation (2.14) with $\mathbf{M}$ defined in (2.16b) reduces to

$$\frac{\partial \boldsymbol{v}(t,\lambda)}{\partial z} = \begin{bmatrix} 2j\lambda^2 & 0 \\ 0 & -2j\lambda^2 \end{bmatrix} \boldsymbol{v} \tag{2.24}$$

because $|q| \to 0$ for large t. The solutions of (2.24) are not compatible with the boundary conditions (2.18) and (2.19) because the equation (2.14) does not allow fixed boundary conditions. Therefore, distance dependent eigenfunctions should be defined. For instance, $\boldsymbol{\Psi} = \boldsymbol{\psi} e^{2j\lambda^2}$ should satisfy (2.14), which results in

$$\partial_z \boldsymbol{\psi} = \begin{bmatrix} 2j\lambda^2 - j|q|^2 - 2j\lambda^2 & -2\lambda q - jq_t \\ 2\lambda q^* - jq_t & -2j\lambda^2 + j|q|^2 - 2j\lambda^2 \end{bmatrix} \boldsymbol{\psi}.$$

Using (2.20a) for $t \to \infty$ leads to

$$a(\lambda, z) = a(\lambda, 0), \tag{2.25a}$$

$$b(\lambda, z) = e^{-4j\lambda^2 z} b(\lambda, 0). \tag{2.25b}$$

which clearly show that eigenvalues (i.e., zeros of $a(\lambda)$) remain unchanged during the evolution. The evolution equation for continuous spectrum and norming constants are then expressed by

$$\rho(\lambda, z) = e^{-4j\lambda^2 z} \rho(\lambda, 0), \tag{2.26}$$

$$C_m(z) = e^{-4j\lambda_m^2 z} C_m(0). \tag{2.27}$$

Infinite number of conserved quantities also exist for any set equations solvable by Zakharov-Shabat problem (2.17), such as NLSE [36]. In fact, the existence of conserved quantities originates from the fact that $a(\lambda)$, is time independent. It is shown in [36] that the nonlinear evolution equations with time independent $a(\lambda)$ are completely integrable

Hamiltonian systems. The trace formula is given by [119]

$$\log a(\lambda) = \sum_{n=0}^{+\infty} \frac{\Gamma_n}{(2j\lambda)^{n+1}},$$

where

$$\Gamma_n = \sum_{m=1}^{M} \left[\frac{(2j\lambda_m^*)^{n+1} - (2j\lambda_m)^{n+1}}{n+1} \right] - \frac{1}{\pi} \int_{-\infty}^{+\infty} (2j\zeta)^n \log\left(1 + |\rho(\zeta)|^2\right) \mathrm{d}\zeta.$$

Also the conservation law can be derived using [34]

$$\Gamma_n = \int_{-\infty}^{+\infty} \gamma_n(x) \mathrm{d}x,$$

where

$$\gamma_0 = -|q|^2,$$

$$\gamma - 1 = q q_t^*,$$

$$\gamma_{n+1} = q \left(\frac{\gamma_n}{q} \right)_t + \sum_{k=1}^{n-1} \gamma_k \gamma_{n-k}, \quad n \geq 2.$$

The equivalent of Parseval equation for ordinary Fourier transform is derived for $n = 0$ as

$$\int_{-\infty}^{+\infty} |q(t)|^2 \mathrm{d}t = \frac{1}{\pi} \int_{-\infty}^{+\infty} \log\left(1 + |\rho(\lambda)|^2\right) \mathrm{d}\lambda + 4 \sum_{m=1}^{M} \Im(\lambda_m).$$

2.2.5 Inverse nonlinear Fourier transform

The inverse nonlinear Fourier transform (INFT) includes finding the time domain signal $q(t, z)$ from the scattering data. The eigenfunctions ϕ and $\tilde{\phi}$ can be represented as [36]

$$\boldsymbol{\phi} = \begin{pmatrix} 0 \\ 1 \end{pmatrix} e^{j\lambda t} + \int_t^{\infty} \boldsymbol{K}(t, s) e^{j\lambda s} \mathrm{d}s \tag{2.28a}$$

$$\tilde{\boldsymbol{\phi}} = \begin{pmatrix} 0 \\ 1 \end{pmatrix} e^{-j\lambda t} + \int_t^{\infty} \tilde{\boldsymbol{K}}(t, s) e^{-j\lambda s} \mathrm{d}s, \tag{2.28b}$$

where $\boldsymbol{K}$ and $\tilde{\boldsymbol{K}}$ are the kernel 2×1 vectors independent of λ. The integral terms in (2.28) determine the eigenfunctions based on the boundary values at $t = \infty$. In [36], it was proved that the solution for $\boldsymbol{K}$ and $\tilde{\boldsymbol{K}}$ exist and are unique by substituting (2.28) in the Zakharov-Shabat problem (2.17) satisfying the necessary and sufficient conditions

$$(\partial_x - \partial_s)K_1(x,s) - q(x)K_2(x,s) = 0,$$

$$(\partial_x + \partial_s)K_2(x,s) + q^*(x)K_1(x,s) = 0,$$

subject to boundary conditions

$$K_1(x,x) = -q(x)/2, \tag{2.29a}$$

$$\lim_{s\to\infty} K_2(x,s) = 0. \tag{2.29b}$$

The Gelfand-Levitan-Marchenko (GLM) integral equations can be derived as follows [120, 121]. Substituting (2.28) in (2.20a) divided by $a(\lambda)$, we have

$$\frac{\boldsymbol{\psi}}{a} = \begin{pmatrix} 1 \\ 0 \end{pmatrix} e^{-j\lambda t} + \int_t^\infty \tilde{\boldsymbol{K}}(x,s)e^{-j\lambda s}\mathrm{d}s + \rho(\lambda)\left(\begin{pmatrix} 0 \\ 1 \end{pmatrix} e^{j\lambda t} + \int_t^\infty \boldsymbol{K}(x,s)e^{j\lambda s}\mathrm{d}s\right). \tag{2.30}$$

Assume contour $\mathcal{C}$ in complex plane starting from $\lambda = -\infty + j0^+$ and ending at $\lambda = +\infty + j0^+$, which does not contain zeros of $a(\lambda)$. Then, by multiplying (2.30) in $e^{j\lambda y}/2\pi$ and integrating respect to λ on contour $\mathcal{C}$ for $y > x$, we have

$$\tilde{\boldsymbol{K}}(x,y) + \begin{pmatrix} 0 \\ 1 \end{pmatrix} F^*(x+y) + \int_x^\infty \boldsymbol{K}(x,s)F(s+y)\mathrm{d}s = 0 \tag{2.31}$$

where

$$F(x) = \frac{1}{2\pi}\int_{-\infty}^{\infty} \rho(\lambda)e^{j\lambda x}\mathrm{d}\lambda - j\sum_{m=1}^{M} C_m e^{j\lambda_m x}. \tag{2.32}$$

The zero on the right side of (2.32) is obtained from the fact that $\psi e^{j\lambda x}$ is analytical in $\mathbb{C}^+$, and the contour $\mathcal{C}$ does not contain any zero of $a(\lambda)$. Note that

$$\tilde{\boldsymbol{K}}(x,y) = \begin{pmatrix} K_2^*(x,y) \\ -K_1^*(x,y) \end{pmatrix},$$

and thus the GLM equations (2.31) can be rewritten as

$$K_1(x,y) - F^*(x+y) + \int_x^\infty \int_x^\infty K_1(x,s)F(s+s')F^*(s+y)\mathrm{d}s\mathrm{d}s' = 0. \tag{2.33}$$

Finally, using (2.29), it is concluded that

$$q(t) = -2K_1(t,t). \tag{2.34}$$

In [122], it was shown that the NFT tends to ordinary Fourier transform for small amplitudes of q. This can be easily confirmed using (2.31) when $F \to \epsilon F$ for $\epsilon << 1$. Another method can also be used for evaluating $q(t,z)$ from the scattering data [123]. Such method, which originates from quantum mechanics, is based on Riemman-Hilbert factorization problem in complex analysis [124]. In this thesis, we only use the GLM approach because it is more tractable through numerical methods.

2.2.6 Data transmission using nonlinear Fourier transform

The NFT transforms the time domain optical signal into scattering data consist of discrete and continuous spectra which evolve linearly along the fibre in nonlinear spectral domain. It is therefore natural to map the data on the scattering data in nonlinear spectral domain, and the input of the communication channel would be $\mathcal{X} = \{\rho(\lambda,0), \{C_m(0)\}_{m=1}^M, \{\lambda_m\}_{m=1}^M\}$. Figure 2.2, schematically demonstrates the input data $\mathcal{X}$ for $M = 7$. It can be seen that $\mathcal{X}$ contains a continuous waveform and several discrete points with positions according to $\{\lambda_m\}_{m=1}^M$ and *amplitudes* (norming constants) $\{C_m(0)\}_{m=1}^M$. The physical optical signal transfers through the fibre in time domain and is affected by nonlinear and dispersion effects. However, the communication channel in nonlinear spectral domain is linear and expressed by $\mathcal{Y} = \mathcal{X} + \mathcal{N}$, where $\mathcal{N}$ is the transformed effective noise. Such approach has recently gained attention in the field of long-haul optical fibre communication and is regarded as a potential solution for the capacity crunch problem (refer to section 1.2 in chapter 1).

Figure 2.3 demonstrates a general NFT-based optical fibre communication system. The data is directly encoded on CS and/or DS in the nonlinear spectral domain. Data is first converted to

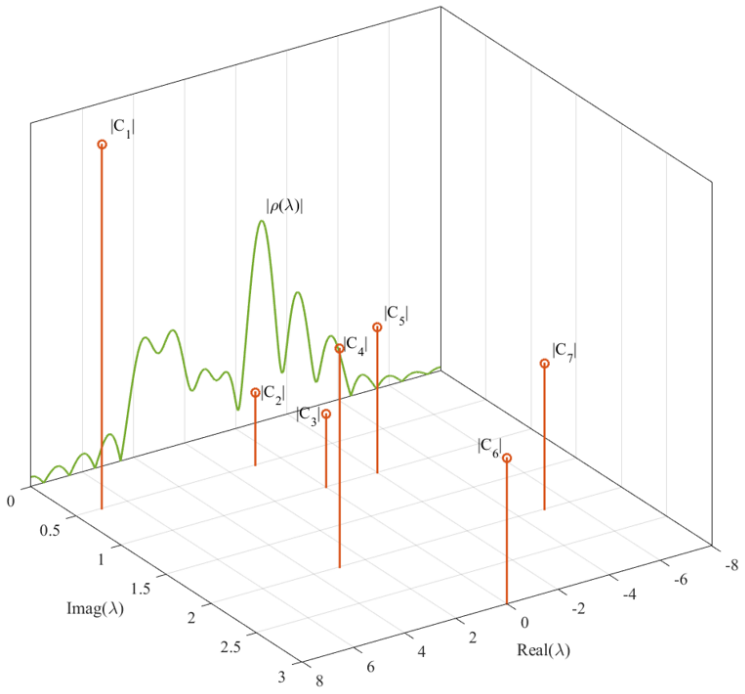

Figure 2.2: Schematic demonstration of input data for NFT-based systems.

a sequence of digital symbols of a specific modulation format, such as quadrature amplitude modulation (QAM), via serial to parallel conversion and constellation mapping. The sequence of digital symbols associated to CS are then converted to an oversampled continuous waveform using a pulse shaping filter (e.g., raised-cosine or sinc pulses). The pulse shaping is required to make the symbols as close as possible while avoiding a high signal bandwidth and consequently enhance the spectral efficiency. Note that since the integral equations of INFT are solved digitally in practice, oversampling is essential for minimizing numerical errors. Then, INFT is applied to the generated CS waveform along with the encoded DS to generate the signal in time domain. The optical transmitter and receiver consist of all operations needed for launching the signal into the fibre and detecting it as a digital signal, such as filtering and analogue/digital conversion. As indicated before, SSMF and ideal distributed amplification are assumed. After photo-detection at the receiver, NFT is performed, and the noisy outputs are obtained. The linear dispersion removal is then performed based on equations (2.26) and (2.27), which allows detection of data symbols.

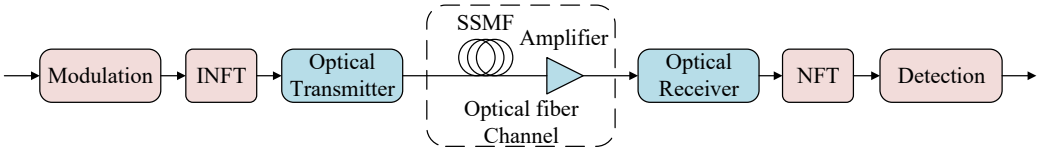

Figure 2.3: General block diagram of a NFT-based communication system.

The structure, shown in Fig. 2.3, is similar to an OFDM structure but using NFT instead of Fourier transform. The NFT decomposes the signal propagating in the nonlinear optical fibre channel to scattering data, which travel linearly in nonlinear frequency domain. This makes the channel tractable. However, using ordinary Fourier transform does not lead to such decomposition to linear channel, and the fibre channel in ordinary frequency domain is still nonlinear and difficult to study. Therefore, NFT is regarded as a useful tool to study and analyse the nonlinear optical fibre, and signalling in nonlinear frequency domain is expected to lead to superior performance.

2.3 Numerical methods

In this section, numerical methods for implementation of NLSE, NFT, and INFT, which are used in this thesis, are presented.

2.3.1 Split-step Fourier method

The NLSE (2.1) can be solved by numerical methods such as finite-difference or split-step Fourier. The former is usually quite complex. The latter, however, is less complex and can be modified for different scenarios. The NLSE (2.1) can be writen as

$$\frac{\partial Q}{\partial l} = \left(\hat{D} + \hat{N}\right) Q, \tag{2.35}$$

where $\hat{D}$ is the dispersion and loss operator defined as

$$\hat{D} = -j\frac{\beta_2}{2}\frac{\partial^2}{\partial \tau^2} - \frac{\alpha}{2},$$

and $\hat{N}$ is the nonlinearity operator defined as

$$\hat{N} = j\gamma|Q|^2.$$

The accurate solution of (2.35) for a small step (i.e., fibre length) of h_{ss} is given by

$$Q(\tau, l+h) = \exp\left[h_{ss}(\hat{D}+\hat{N})\right] Q(\tau, l),$$

which may be approximated by

$$Q(\tau, l+h_{ss}) \approx \exp(h_{ss}\hat{D}) \exp(h_{ss}\hat{N}) Q(\tau, l), \tag{2.36}$$

by assuming that nonlinearity and dispersion affect the wave propagation separately. It is assumed that first the nonlinearity operator ia applied, and an intermediate solution, only applying the nonlinear operator, is given by

$$Q_n(\tau, l+h_{ss}) = e^{jh_{ss}\gamma|Q(\tau,l)|^2} Q(\tau, l). \tag{2.37}$$

The dispersion operator is then applied in the frequency domain as

$$\tilde{Q}(\omega, l+h_{ss}) = e^{+jh_{ss}\frac{\beta_2}{2}\omega^2 - h_{ss}\frac{\alpha}{2}} \tilde{Q}(\omega, l), \tag{2.38}$$

where $\tilde{Q}(\omega, l)$ is Fourier transform of $Q(\tau, l)$. Since the Fourier transform is performed by fast algorithm (FFT), the split-step Fourier method is two orders of magnitude faster than finite-difference [125]. The error using the split-step method (2.36) can be reduced by using the symmetric method [126]

$$Q(\tau, l+h_{ss}) \approx \exp\left(\frac{h_{ss}\hat{D}}{2}\right) \exp\left(h_{ss}\frac{\hat{N}(l) + \hat{N}(l+h_{ss})}{2}\right) \exp\left(\frac{h_{ss}\hat{D}}{2}\right) Q(\tau, l), \tag{2.39}$$

in which the nonlinearity is applied in the middle of the step length. The choice of step size h_{ss} is another factor which determines the induced error. Depending on the scenario, it can be defined based on different criteria [127]. In this thesis, we use constant step size based on the error observed on the continuous spectrum for noise-free case. The step size h_{ss} is chosen

small enough so that the numerical error added by split-step method to the continuous spectrum is negligible.

It should be noted that, for numerically implementing the noisy NLSE (2.5), the ASE noise is added at the end of each step as a white Gaussian noise with PSD equal to $N_{\rm ASE}h_{ss}/L$ using (2.4).

2.3.2 Numerical implementation of NFT

Several numerical methods can be used for implementation of NFT [25, 27, 77]. Here, the so-called Ablowitz-Ladik discretization method is used [25]. The feature of this technique is that it leads to discrete version on NLSE which is also integrable [128].

In the definition of the NFT, it is assumed that the $|q(t)|$ is rapidly vanishing for large t. In practice, it is assumed that $q(t) = 0$ outside the finite interval $t_1 \leq t \leq t_2$. Assuming that the time interval is divided to N_{AL} equidistant points with $\epsilon = (t_2 - t_1)/N_{AL}$, the eigenvalue problem (2.17) can be discretized as

$$\frac{1}{\epsilon}\left(\boldsymbol{v}[n+1] - \boldsymbol{v}[n]\right) = \begin{bmatrix} -j\lambda & q[n] \\ -q^*[n] & j\lambda \end{bmatrix} \boldsymbol{v}[k], \quad n = 0, \cdots, N_{AL},$$

where $q[n] = q(t_1 + n\epsilon)$. Considering $e^{\pm j\lambda\epsilon} = 1 \pm j\lambda\epsilon$, the eigenvalue problem can be written as

$$\boldsymbol{v}[n+1] = \begin{bmatrix} e^{j\lambda\epsilon} & \epsilon q[n] \\ -\epsilon q^*[n] & e^{-j\lambda\epsilon} \end{bmatrix} \boldsymbol{v}[k], \quad n = 0, \cdots, N_{AL},$$

with the initial value determined based on (2.18) as

$$\boldsymbol{v}[0] = \begin{pmatrix} 1 \\ 0 \end{pmatrix} e^{-j\lambda t_1}.$$

Then, the scattering coefficients are found based on the limit (2.23) as

$$a(\lambda) = v_1[N_{AL}]e^{j\lambda t_2}$$

$$b(\lambda) = v_2[N_{AL}]e^{-j\lambda t_2}$$

It is clear that continuous spectrum can be simply found as $\rho(\lambda) = b(\lambda)/a(\lambda)$. For calculation of eigenvalues and norming constants, $a(\lambda)$ is found using the method above with required resolution of nonlinear frequency λ. Then, $a'(\lambda)$ is estimated and zeros of $a(\lambda)$ are found by searching the finely gridded upper complex plane.

2.3.3 Numerical implementation of INFT

Here, a simple method is presented for numerical INFT calculation. Considering $F(x) = 0$ for $|x| \geq A$, the solution to the GLM equations (2.31) would be zero for $x+y \geq A$. Therefore, the integrals are needed to be solved in the area between $x + y \leq A$ and $y \geq x$. We may discretise the GLM integral equations for a uniform grid on x-y plane. Assuming $x_i = \frac{A}{2} - i\hat{h}, \quad i = 0, 1, 2, \cdots$, for each i there are $2i+1$ points $y_{ij} = x_i + j\hat{h}, \quad j = 0, 1, \cdots, 2i$, where $\hat{h}$ denotes the resolution which is equal for both dimensions x and y. The discretised GLM integral equations, stated below, should be solved in order to determine $K_1(x_i, x_i)$.

$$K_2^*(x_i, y_j) + \hat{h} \sum_{n=-i}^{i-j} K_1(x_i, \frac{A}{2} + n\hat{h}) F(A + (n - i + j)\hat{h}) = 0, \tag{2.40a}$$

$$K_1(x_i, y_j) - \hat{h} \sum_{n=-i}^{i-j} K_2^*(x_i, \frac{A}{2} + n\hat{h}) F^*(A + (n - i + j)\hat{h}) = F^*(x_i + y_j). \tag{2.40b}$$

The GLM integral equations are then converted into the matrix form as

$$\begin{bmatrix} \mathbf{I} & -\mathbf{R_i}^* \\ \mathbf{R_i} & \mathbf{I} \end{bmatrix} \begin{bmatrix} \boldsymbol{K_1} \\ \boldsymbol{K_2^*} \end{bmatrix} = \begin{bmatrix} \boldsymbol{F}^* \\ \mathbf{0} \end{bmatrix}, \tag{2.41}$$

where considering $f_k = \hat{h}F(A - k\hat{h})$, $\mathbf{R_i}$ can be expressed as

$$\mathbf{R_i} = \begin{bmatrix} f_{2i} & f_{2i-1} & \cdots & f_1 & f_0 \\ f_{2i-1} & f_{2i-2} & \cdots & f_0 & 0 \\ \vdots & & & & \\ f_0 & 0 & \cdots & 0 & 0 \end{bmatrix}, \tag{2.42}$$

and $\boldsymbol{F} = \frac{1}{\hat{h}}\{f_{2i} \;\; f_{2i-1} \;\; \cdots \;\; f_1 \;\; f_0\}^t$.

We need to find the first element of $\boldsymbol{K_1}$ (i.e. $K_1(x_i, x_i)$). To determine $K_1(x_0, x_0)$, $K_1(x_1, x_1)$, $\cdots$, $K_1(x_{N-1}, x_{N-1})$, we need to solve N linear equations as in (2.41) with sizes $2 \times 2, 6 \times 6, \cdots, (4N-2) \times (4N-2)$, respectively. These systems can be solved through different methods, but symmetry in the elements of the matrix and the fact that we only need to find the first element of the unknown vector K_1 can be used to reduce the complexity of numerical computations. Expanding (2.41), one can see that the particular arrangement of elements in the matrix system (2.43) allows to find the first element of K_1 for every i by performing only one Gaussian elimination on the highest order system (i.e. $(4N-2) \times (4N-2)$). Also, note that half of the Gaussian elimination operations can be performed analytically, and consequently, the rest of operations are carried out numerically for the equation $(\mathbf{I} + \mathbf{R}\mathbf{R}^*)\mathbf{K_1} = \mathbf{F}^*$.

$$\begin{bmatrix} \mathbf{I} & -\mathbf{R}^* \\ \mathbf{R} & \mathbf{I} \end{bmatrix} = \begin{bmatrix} 1 & \cdots & 0 & 0 & 0 & f^*_{2N-2} & f^*_{2N-3} & f^*_{2N-4} & \cdots & f^*_0 \\ \vdots & & & & & & & & & \\ 0 & \cdots & 1 & 0 & 0 & f^*_2 & f^*_1 & f^*_0 & \cdots & 0 \\ 0 & \cdots & 0 & 1 & 0 & f^*_1 & f^*_0 & 0 & \cdots & 0 \\ 0 & \cdots & 0 & 0 & 1 & f^*_0 & 0 & 0 & \cdots & 0 \\ f_{2N-2} & \cdots & f_2 & f_1 & f_0 & 1 & 0 & 0 & \cdots & 0 \\ f_{2N-3} & \cdots & f_1 & f_0 & 0 & 0 & 1 & 0 & \cdots & 0 \\ f_{2N-4} & \cdots & f_0 & 0 & 0 & 0 & 0 & 1 & \cdots & 0 \\ \vdots & & & & & & & & & \\ f_0 & \cdots & 0 & 0 & 0 & 0 & 0 & 0 & \cdots & 1 \end{bmatrix} \tag{2.43}$$

Chapter 3

Capacity of signalling on the continuous spectrum

In this chapter, a model is developed for the channel in nonlinear spectral domain when data is mapped only on the continuous spectrum (CS). It is observed that the effective noise added to the CS signal is dependent on the signal amplitude. The channel model of such NFT-based optical fibre communication systems is studied based on the behaviour of the propagated optical signal in time domain for an asymptotically long fibre length. The derived channel model is validated using simulation for different scenarios of practical interest. A variance normalizing transform is applied as a tool to obtain an estimate on the capacity of the underlying channel. At the end, achievable data rates in bits per second are estimated by taking into account the temporal dispersion and available bandwidth.

Providing an accurate noise model and estimating the capacity of NFT-based systems is an important open problem. In [46], the noise in the CS channel was modelled using low order perturbation theory and a lower bound of 10.7 bits per symbol for WDM Nyquist and OFDM was derived using Pinsker estimation over 500 GHz bandwidth and 2,000 km fibre length. Also, in [43], similar results were obtained for defocusing case using direct modulation and sampling. Although, the general results obtained using novel approaches in this chapter agree with previous works, the results in this chapter are significant because of more accurate analysis of the communication system for practical scenarios, the obtained distinctive feature of the CS channel, and the estimation of achievable data rates in bits per second.

For simplicity in notation, the dependence to distance is dropped and shown as subscript wherever possible. For instance, $q(t, L)$ may be represented by $q_L(t)$ for fibre length L.

3.1 Communication system with signalling on CS

The block diagram of a typical NFT-based system with direct mapping of data on CS is demonstrated in Figure 3.1. Here, we consider only CS, which correspond to the dispersive radiation waves. In other words, $\{C_m(z)\}_{m=1}^{M}$ and $\{\lambda_m\}_{m=1}^{M}$, which correspond to solitonic waves, are zero throughout this chapter. In Figure 3.1, $\mathbf{D}_0$ is the vector of K symbols, which are derived from the binary data using a specific modulation format. The symbols in $\mathbf{D}_0$ are then converted to an oversampled continuous waveform $\rho_0(\lambda)$ using a pulse shaping filter (e.g., raised-cosine or sinc pulses). Note that since the integral equations of INFT are solved digitally in practice, oversampling is essential for minimizing numerical errors. Then, INFT is applied to generate the time domain signal $q_0(t)$. The optical transmitter (Tx) and receiver (Rx) consist of all operations needed for launching the signal into the fibre and detecting it as a digital signal, such as (de)normalization in (2.9), optical filtering, and analogue/digital conversion. Standard single mode fibre (SSMF) and ideal distributed amplification are assumed. At the receiver, after NFT operation and removing the phase shift introduced according to (2.26), the noisy CS signal $\tilde{\rho}_L(\lambda)$ is obtained, from which the data symbols can be recovered.

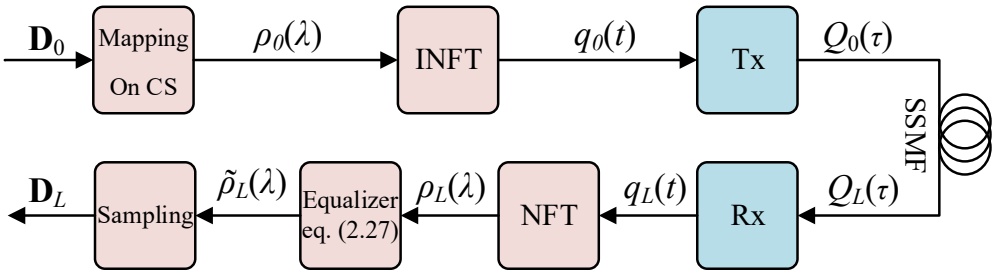

Figure 3.1: Block Diagram of a NFT-based system with direct mapping on CS.

3.2 Asymptotic analysis

In this section, asymptotic analysis of the noise in a NFT-based system with signalling on CS is presented. Asymptotic here refers to long distances of fibre $L \to \infty$. However, the asymptotic solution may be valid for many practical scenarios as well. Specifically for the signal only containing radiation and without soliton, the large dispersion can lead to the

asymptotic solution even in practical cases.

3.2.1 Asymptotic solution of NLSE

For relatively long fibre length, it can be shown that signal can be expressed in a slow-varying similarity solution form [36]

$$q(t,z) = \frac{1}{\sqrt{z}} A(t,z) e^{jz\theta(t,z)} \tag{3.1}$$

$$A(t,z) = f\left(\frac{t}{z}\right) + \sum_{n=1}^{\infty}\sum_{k=0}^{n} \frac{(\log z)^k}{z^n} f_{n,k}\left(\frac{t}{z}\right)$$

$$\theta(t,z) = \frac{1}{4}\left(\frac{t}{z}\right)^2 + \sum_{n=1}^{\infty}\sum_{k=0}^{n} \frac{(\log z)^k}{z^n} \theta_{n,k}\left(\frac{t}{z}\right)$$

where

$$\begin{aligned}
\theta_{1,0} &= g \\
\theta_{1,1} &= 2f^2 \\
f_{1,0} &= fg^{''} + 2g^{'}f^{'} + 4f(2(f^{'})^2 + ff^{''}) \\
f_{1,1} &= 4f(3(f^{'})^2 + ff^{''})
\end{aligned}$$

where $f(\frac{t}{z}) \geq 0$ and $g(\frac{t}{z})$ are real valued functions. For simplicity, terms $(\frac{t}{z})$ are omitted in above equations. The order of remaining terms would be $O((\frac{\log z}{z})^2)$, so for large z higher orders can be ignored without introducing significant error. It should be recalled that $z = L/2L_D$. Thus, asymptotic scenario (large z) can be satisfied for long fibre or high signal bandwidth (small T_0) or a combination of both.

There are different ways to find $f(\frac{t}{z})$ and $g(\frac{t}{z})$ in terms of spectra [36, 129, 130]. For the case that DS is zero, the asymptotic solution for the NLSE can be related to the CS as follows:

$$f^2(\frac{t}{z}) = \frac{1}{4\pi}\log\{1 + |\rho(\frac{-t}{4z})|^2\}, \tag{3.2}$$

$$g(\frac{t}{z}) = -\arg\{\rho(\frac{-t}{4z})\} + \frac{3\pi}{4} - \arg\{\Gamma(1+2jf^2(\frac{t}{z}))\} - 2\log 2f^2(\frac{t}{z}) - 2\int_{t/z}^{\infty} \log(y-\frac{t}{z})\frac{\partial f^2(y)}{\partial y}\mathrm{d}y + 2\int_{-\infty}^{t/z} \log|y+\frac{t}{z}|\frac{\partial f^2(y)}{\partial y}\mathrm{d}y.$$

The equation (3.2) can be easily verified using the conserved quantities described in section 2.2.4. Therefore, the asymptotic temporal signal can be expressed in terms of $\rho(\cdot)$. Now by only considering the leading factor in (3.2.1), we have

$$A(t,z) \approx f\left(\frac{t}{z}\right),$$

and therefore the amplitudes of temporal signal $q(t,z)$ at length z can be expressed in terms of amplitude of CS by

$$|q(t,z)|^2 = \frac{1}{z}f^2(\frac{t}{z}) = \frac{1}{4\pi z}\log\{1+|\rho(\frac{-t}{4z})|^2\} \tag{3.3}$$

or inversely

$$|\rho(\lambda)|^2 = e^{4\pi z|q(-4z\lambda,z)|^2} - 1. \tag{3.4}$$

Figure 3.2[1] compares the simulated amplitude of the temporal signal propagated over the fibre at $z = 10$ with the corresponding signal predicted by the asymptotic equation in (3.3). We first generate a CS continuous waveform by applying raised-cosine filtering to a sequence of 16 random symbols from the 16QAM constellation. By applying INFT on this CS signal, the temporal signal is generated at the input of the fibre which occupies a bandwidth of $W = 30$ GHz measured based on 99% energy of the signal $Q_0(\tau)$. It can be seen that the temporal signal can be well approximated by asymptotic equation (3.3) while increasing z would further reduces the error. Note that inverse scattering implies that this asymptotic solution for propagation over optical fibre can be also used to describe the behaviour of nonlinear Fourier transform at the end of the fibre.

[1]The parameters in the figure are the normalized parameters and are unit-less.

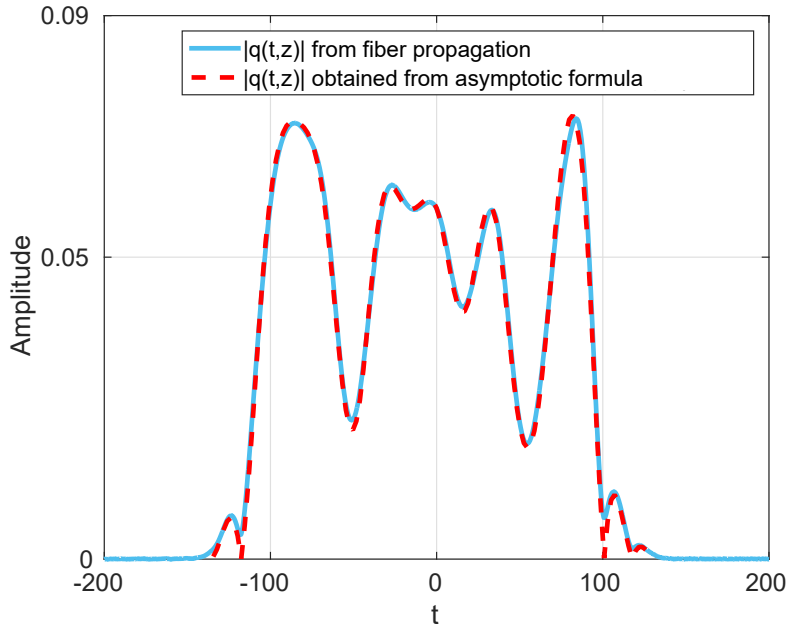

Figure 3.2: Accuracy of the asymptotic formula for temporal signal in (3.3) at $z = 10$ where t is the normalized time defined in (2.9) *for $T_0 = 0.05$ ns.*

3.2.2 Channel statistics based on the asymptotic analysis

The nonlinear Fourier transform allows us to describe nonlinear optical fibre channels in a linear form based on signalling over the nonlinear spectrum. For CS, this linear channel model is give by

$$\tilde{\rho}_L(\lambda) = \rho_0(\lambda) + \eta_L(\lambda), \tag{3.5}$$

where

$$\tilde{\rho}_L(\lambda) = \rho_L(\lambda) \exp(4j\lambda^2 L/2L_D)$$

refers to noisy CS signal after phase shift removal according to (2.26), and $\eta_L(\lambda)$ is the noise. It can be shown that the noise is zero-mean, i.e., $\mathsf{E}\{\tilde{\rho}_L(\lambda)\} = \rho_0(\lambda)$. This can be done readily by considering that $\mathsf{E}\{n(t,z)\} = 0$ in the normalized NLSE (2.8) and taking an ensemble average from the Zakharov-Shabat eigenvalue problem (2.17) which are basically two coupled differential equations.

In order to obtain the second order statistics of the noise in CS domain, we use the asymptotic solution introduced in previous subsection to describe NFT at the end of the fibre. Note that

the term "asymptotic" refers to the long fibre length L, at which the signal is significantly dispersed. In asymptomatically long fibre lengths, the signal amplitude is largely reduced due the dispersion. Thus, nonlinear signal-noise interactions would not be significant after the signal is propagated along the fibre for lengths larger than dispersion length. Here, we assume $q_L(t) = q_{\mathrm{NF}}(t) + n_L(t)$ resemble the propagated signal in time at the end of fibre where $n_L(t) = n_L^r(t) + jn_L^i(t)$ is the noise at the end of fibre, and $q_{\mathrm{NF}}(t) = q_{\mathrm{NF}}^r(t) + jq_{\mathrm{NF}}^i(t)$ is the signal when noise is absent. Note that the noise $n_L(t)$ includes the ASE noise and its interactions with signal at the initial distances of signal propagation. A simple simulation is performed to demonstrate that included assumptions are acceptable. Figure 3.3a shows signals at $L = 3000$ km or $z = 78$ with and without noise for a complex Gaussian input pulse, and the probability distribution of noise on the real part of the signal (similar results for imaginary part) as well as its Gaussian fit are demonstrated in Figure 3.3b. It is observed that the signal at this length can be regarded as the noise-free signal plus a noise which happens be to very close to Gaussian.

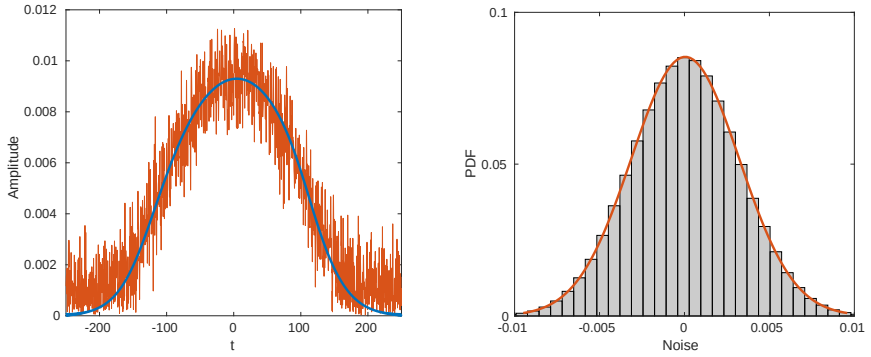

(a) (b)

Figure 3.3: (a) Received signal with and without noise at an asymptotically long fibre length $L = 3000$ km or $z = 78$. (b) PDF of noise on the real part (or imaginary part) of the signal in the time domain.

Using (3.4), the intensity of CS signal after applying NFT can be expressed as

$$|\tilde{\rho}_L(\lambda)|^2 = e^{4\pi z|q_{\mathrm{NF}}(t)+n_L(t)|^2} - 1. \tag{3.6}$$

Accordingly, the second moment of the noise in CS can be written as

$$\begin{aligned}\mathsf{E}\{|\eta_L|^2\} &= \mathsf{E}\{|\tilde{\rho}|^2\} - |\rho_0|^2 \\ &= e^{4\pi z|q_{\rm NF}|^2}\left(\mathsf{E}\{e^{4\pi z\left((n_L^r)^2+(n_L^i)^2+2q_{\rm NF}^r n_L^r+2q_{\rm NF}^i n_L^i\right)}\}-1\right).\end{aligned} \tag{3.7}$$

Here, for simplicity, the dependence on λ and time is omitted and $q_{\rm NF} = q_{\rm NF}(t)$. Assuming circularly symmetric Gaussian noise $n_L \sim \mathcal{N}(0,\sigma_0^2)$ at the end of fibre, the part corresponding to the real noise in time can be described as

$$\mathsf{E}\{e^{4\pi z\left((n_L^r)^2+2q_{\rm NF}^r n_L^r\right)}\} = \frac{e^{\frac{(4\pi z q_{\rm NF}^r)^2}{c_\rho}}}{\sqrt{\pi\sigma_0^2}}\int_{-\infty}^{\infty} e^{-c_\rho t^2}\mathrm{d}t,$$

where $c_\rho = \frac{1}{\sigma_0^2} - 4\pi z$. For practical ranges of fibre-optic channel parameters, the parameter c_ρ remains positive[1] for which we have

$$\mathsf{E}\left\{e^{4\pi z\left((n_L^r)^2+2q_{\rm NF}^r n_L^r\right)}\right\} = \frac{1}{\sqrt{c_\rho\sigma_0^2}}e^{\frac{(4\pi z q_{\rm NF}^r)^2}{c_\rho}}. \tag{3.8}$$

Similar derivations can be made for imaginary part of (3.7) and thus, the noise variance in CS can be asymptotically calculated as

$$\begin{aligned}\mathsf{E}\{|\eta_L|^2\} &= e^{4\pi z|q_{\rm NF}|^2}\left(\frac{e^{\frac{|4\pi z q_{\rm NF}|^2}{c_\rho}}}{c_\rho\sigma_0^2}-1\right) \\ &= \left(|\rho_0|^2+1\right)\left(\frac{\left(|\rho_0|^2+1\right)^{\frac{4\pi z}{c_\rho}}}{c_\rho\sigma_0^2}-1\right).\end{aligned} \tag{3.9}$$

The random variable $X = |q_{\rm NF}+n_L|^2/\sigma_0^2$ has a noncentral Chi-squared distribution with non centrality parameter $\zeta = |q_{\rm NF}|^2/\sigma_0^2$ and two degrees of freedom. Thus, the probability density function (PDF) of amplitude of CS as a random variable $Y = \sqrt{e^{4\pi z\sigma_0^2 X}-1}$ can be calculated as

[1]The normalized noise power at the end of the fibre can be expressed as $\sigma_0^2 = \alpha h\nu_s K_T\gamma L_D LW$ where W is the linear signal bandwidth. Then, the criteria for positive c can be obtained as $W < 1/(2\pi\alpha h\nu_s K_T\gamma L^2)$. For example, for the parameters used in this paper and $L = 3000$ km we should have $W < 2$ THz.

$$f_Y(y) = \frac{2y}{4\pi z\sigma_0^2(1+y^2)} f_X\left(\frac{1}{4\pi z\sigma_0^2}\log(1+y^2)\right)$$
$$= \frac{ye^{-\zeta/2}}{4\pi z\sigma_0^2(1+y^2)^{1+1/8\pi z\sigma_0^2}} \mathrm{I}_0\left(\sqrt{\frac{\zeta}{4\pi z\sigma_0^2}\log(1+y^2)}\right)$$

where $\mathrm{I}_0(x)$ is the modified Bessel function of the first kind. It should be noted that the noncentrality parameter can be related to the input CS as

$$\zeta = \frac{1}{4\pi z\sigma_0^2}\log\left(1+|\rho_0|^2\right)$$

The PDFs for different amplitudes of CS ($|\rho_0|$) are depicted in Figure 3.4 for $4\pi z\sigma_0^2 = 0.5$. It can be seen that the PDF depends on the signal amplitude $|\rho_0|$, and the variance increase for higher amplitudes.

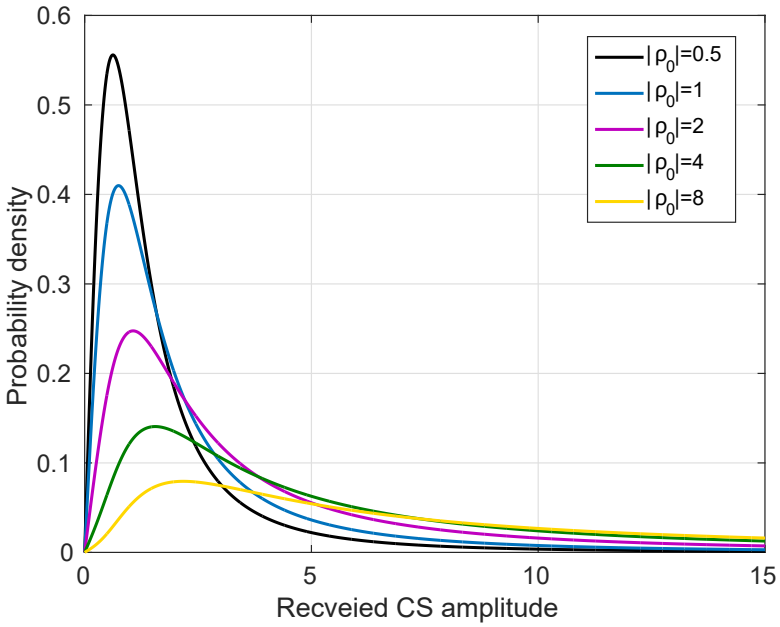

Figure 3.4: PDF of noise in CS channel for asymptotic scenario for different amplitudes of CS and $4\pi z\sigma_0^2 = 0.5$.

It can be seen from (3.9) that the noise variance depends on the signal amplitude $|\rho_0|$, and the order of dependence is $2 + 8\pi z/c_\rho$ which is larger than two. In the following sections, it will be demonstrated that this characteristic plays an important role in determining the capacity of

the channel. We also expect that the probability density function of noise not to be normal in practical case similar to the asymptotic PDF found above. In the next section, the behaviour of the CS channel will be studied numerically and these main characteristics (i.e. signal dependency of noise, order of dependence larger than 2, and non-Gaussian distribution) are verified even at not necessarily asymptotic regimes.

3.3 Numerical study of noise

In this section, simulation results are presented to study the characteristics of noise in CS. Only the effect of ASE noise as a result of amplification and its interaction with signal during the propagation along the fibre is considered here. It is essential to minimize the numerical error in NFT and INFT calculation as well as split-step Fourier method for fibre propagation, so that only noise remains as the source of distortion. This would increase the computational complexity, and since large number of samples are needed for estimating the noise statistics, the simulations would be highly time consuming. To overcome this problem, the simulations were all performed using more than 500 CPUs available for parallel computing at the Institute for Digital Communication at the University of Edinburgh without which the time needed for these simulations would have been escalated.

It should be noted that the complexity of numerical methods increases when the input power increases as observed in [42]. For a larger signal amplitude of CS a higher time resolution is needed for INFT in order to achieve the same error as for smaller amplitudes of signal. Therefore, it is essential to adaptively increase complexity for noise analysis to keep the numerical errors constant and below a desired value. However, downsampling is performed after calculation of $q_0(t)$ for launching the signal into the fibre which will not affect the numerical errors in the next steps.

In order to obtain the noise statistics, several streams of random symbols in various nonlinear frequencies λ with different noise realizations were analysed, truncated sinc pulses were utilized for pulse shaping, and $T_0 = 0.1$ ns was chosen. A signal was generated using 32 random complex symbols with the aforementioned pulse shaping and the required oversampling. It was transmitted through the fibre channel 20000 times for different noise realizations. Over all about 1.6×10^7 random samples were used. Split-step Fourier method

was used for propagation of signal along the fibre, and ASE noise was added in each step. After NFT, the noise samples were first extracted and then their statistic were calculated. Note, however, that although the main features of the asymptotic channel model described in section 3.2.2 are verified here at non-asymptotic ranges of z, we do not expect that the numerical values match accurately.

The dependence of noise variance on the amplitude of signal in CS is shown in Figure 3.5. In order to plot this figure, several combination of real and imaginary signals are considered for each amplitude, resulting in the same noise statistics for all of them. It can be seen in Figure 3.5 that the variance of noise drastically increases for longer fibres. The Simulation results also show that the variance of noise has a dependency to signal amplitude with an order larger than two if the variance is approximated by a polynomial. For example, in Figure 3.5, the orders of dependence for different fibre lengths are about 4. This result numerically confirms that the asymptotic statistical behaviour of the noise in CS as shown in equation (3.9) is even true for these lower values of z which correspond to some practical scenarios.

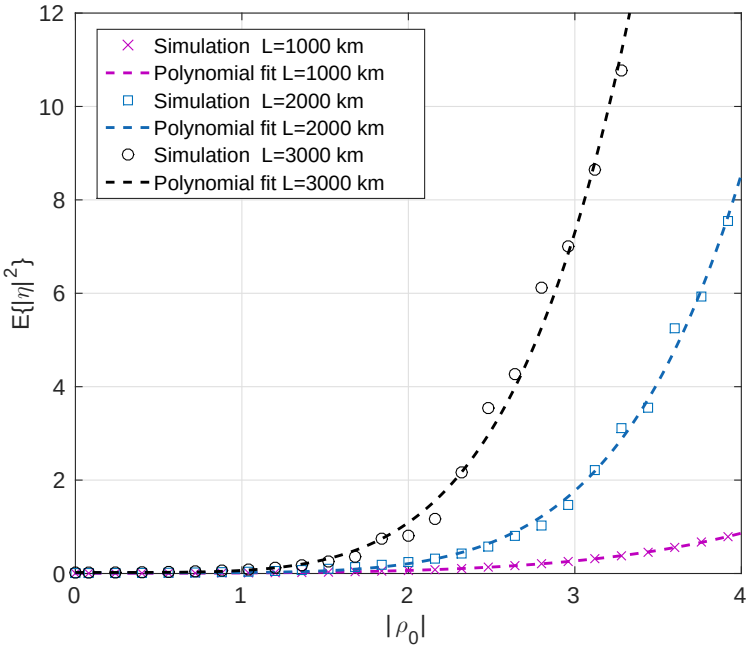

Figure 3.5: Variance of noise $\mathsf{E}\{|\eta_L|^2\}$ *for different signal amplitudes* $|\rho_0|$.

In Figure 3.6, the PDF of the received signal amplitude in CS is demonstrated. Many noise

samples are extracted at different nonlinear frequencies for which $\rho_0(\lambda) = 1$, 2, or 3. As expected, it can be seen that the distribution is not normal, and moreover the variance is increasing for higher values of input signal.

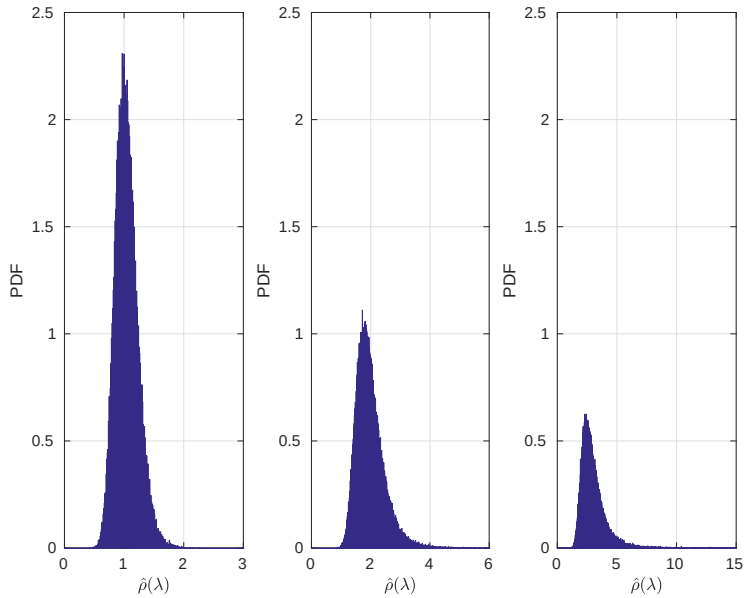

Figure 3.6: PDFs of received noisy CS for different input signal $\rho_0(\lambda) = 1, 2, 3$ from left to right.

Note that the asymptotic model described in section 3.2 does not deliver explicit information about the noise on real and imaginary parts of CS. Here, we introduce additional variables in order to investigate the behaviour of the noise for real and imaginary parts of CS.

$$\tilde{\rho}_L(\lambda) = \tilde{\rho}_L^r(\lambda) + j\tilde{\rho}_L^i(\lambda), \quad \tilde{\rho}_L^r(\lambda), \tilde{\rho}_L^i(\lambda) \in \mathbb{R},$$

$$\eta_L(\lambda) = \eta_L^r(\lambda) + j\eta_L^i(\lambda), \quad \eta_L^r(\lambda), \eta_L^i(\lambda) \in \mathbb{R},$$

Furthermore, the conditional noise variance of real and imaginary parts of CS are defined below to demonstrate the dependency between real and imaginary parts.

$$\sigma_{ry}^2(x) = \mathsf{E}\{|\eta_L^r(\lambda)|^2 | \rho_0^r(\lambda) = x, \rho_0^i(\lambda) = y\},$$

$$\sigma_{iy}^2(x) = \mathsf{E}\{|\eta_L^i(\lambda)|^2 | \rho_0^i(\lambda) = x, \rho_0^r(\lambda) = y\}.$$

As depicted in Figure 3.7, the simulation results of the conditional variances, $\sigma^2_{r1}(x)$ and $\sigma^2_{r2}(x)$, show that the noise on real and imaginary parts of signal are dependent. Hence, real and imaginary channels on CS cannot be considered as independent channels, but nonetheless, these two channels have identical noise behaviour. This is concluded from the fact that $\sigma^2_{ry}(x) = \sigma^2_{iy}(x)$ as demonstrated in Figure 3.7. The dependence of real and imaginary parts of signal means that the capacity estimation cannot be performed independently in real and imaginary channels. Even if it is considered that information is mapped on the amplitude and phase of the signal, it can be easily demonstrated that the noise on both quantities depend of the signal amplitude. Therefore, the capacity estimation here is not straightforward. It should be emphasized that despite dependence of real and imaginary channels, the variance of noise $\mathsf{E}\{|\eta_L(\lambda)|^2\}$ perfectly depends only on the amplitude of signal $|\rho_0(\lambda)|$ as shown in Figure 3.5. Therefore, it can be concluded that if signalling is only performed on the real channel ($\rho^i_0(\lambda) = 0$), the variance of the real noise would be perfectly dependent on the signal amplitude.

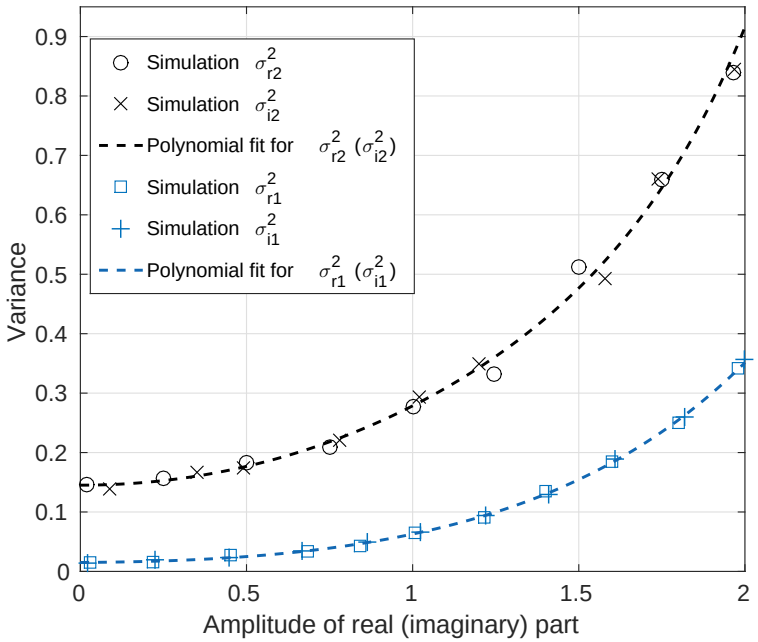

Figure 3.7: Dependence of variance of noise in real (imaginary) channel on the amplitude of signal in imaginary (real) channel.

It should be noted that the dependence of real and imaginary parts of the noise is

comprehensively studied using perturbation theory in [131]. It is specifically shown that, in asymptotic regime, the variance of real and imaginary parts of the noise are equal $\mathsf{E}\{|\eta_L^r(\lambda)|^2\} = \mathsf{E}\{|\eta_L^i(\lambda)|^2\}$ and depend on the signal amplitude. It is also demonstrated that the correlation $\mathsf{E}\{\eta_L^r(\lambda)\eta_L^i(\lambda)\}$ is non-zero and dependent to the amplitude. The results of [131] confirm the observations from the simulations presented in this section.

3.4 Capacity problem

In this section, the capacity of the CS channel is investigated based on the channel model introduced in the last section and using a variance normalizing transform, which will be defined next.

3.4.1 Variance Normalizing transform

In this section, a variance normalizing transform (VNT) is introduced that can be applied to any random variable with a variance that is a function of its mean to generate an approximately Gaussian random variable with a variance independent of its mean [132–134]. VNT can be essentially used to convert an additive (possibly non-Gaussian) noise channel with signal-dependent noise to a conventional additive Gaussian noise channel where signal and noise are independent [132–134]. In effect, the conventional coding and signal processing techniques would be sufficient for efficient communication over the transformed channel. Shot noise is an example of a signal-dependent noise and VNT has been recently used for efficient signalling and capacity approximation over shot-noise-limited channels [135, 136].

The variance normalizing transform that normalizes the random variable W, with mean μ_W and variance

$$\sigma_W^2 = f^2(\mu_W), \tag{3.10}$$

is defined as [132]

$$T(s) = \int \frac{1}{f(s)} \mathrm{d}s. \tag{3.11}$$

The normalized (i.e., transformed) random variable $Y = T(W)$ has then the statistics of $\sigma_Y^2 \simeq$

1 and $\mu_Y \simeq T(\mu_W)$ for sufficiently large values of μ_W. This arises from the fact that

$$\sigma_Y^2 = \mathsf{E}\{|Y-\mu_Y|^2\} = \mathsf{E}\{\left[T(\mu_W + T'(\mu_W)(W-\mu_W)\right]^2\} - T^2(\mu_W), \tag{3.12}$$

where the Taylor series expansion is used as

$$T(W) \simeq T(\mu_W) + T'(\mu_W)(W-\mu_W),$$

which indicates that $\mu_Y \simeq T(\mu_W)$. Thus, by applying the VNT (3.11) to (3.12), we have

$$\sigma_Y^2 = \left[T'(\mu_W)\right]^2 \sigma_W^2 = \left[T'(\mu_W)\right]^2 f^2(\mu_W) = 1.$$

For instance, if W has Poisson distribution with parameter μ_W, the VNT can be defined as $T(s) = \sqrt{s+c}$ for an arbitrary constant c at $s \geq -c$. This transform is called *square root transformation* [133, 135]. The distribution of random variable Y for $\mu_W \to \infty$ tends to Gaussian distribution with mean $\sqrt{\mu_W + c}$ and variance $1/4$ [133]. In [134], it was also shown that the probability distribution of the normalized random variable tends to Gaussian distribution for a family of originally non-Gaussian probability distribution.

It is obvious from (3.11) that the VNT exists for any well-behaving finite and positive function f. Thus, the VNT T exists and is injective. Also, inverse function T^{-1} exists that is an important factor in definition of communication channel based on VNT. Based on (3.11), the VNT is always a positive, but it can be a linear or nonlinear function.

Let random variable W be the output of a channel where the signal $S = \mu_W$ is corrupted by a zero-mean signal dependent noise N with variance as in (3.10). Applying VNT as defined in (3.11) to the noisy signal $W = S + N$ (i.e., $\mathsf{E}\{W\} = S$), we will have

$$Y = T(W) = T(S+N) \simeq T(S) + N_T,$$

where N_T is a zero mean Gaussian noise with unit variance independent of the transformed signal $T(S)$. Consequently, a communication channel can be defined as shown in Figure 3.8, in which the signal is originally generated in a *transformed* domain and then mapped into

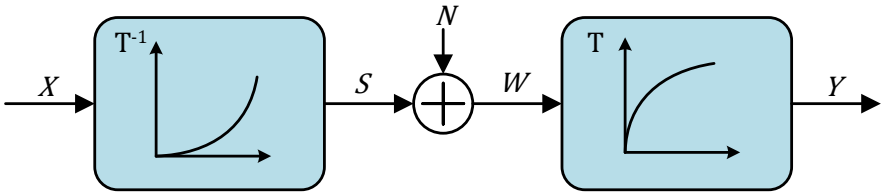

Figure 3.8: Transforming the communication channel with signal-dependent noise to an AWGN channel using VNT.

the original signal domain S using inverse VNT. After transmission through the channel and addition of signal-dependent noise N, VNT is applied, and the output signal can be expressed as

$$Y = X + N_T. \tag{3.13}$$

which defines a conventional additive white Gaussian noise (AWGN) channel. The following lemma shows that the capacity of this transformed channel is equal to the capacity of the original channel $W = S + N$ with signal-dependent noise.

Lemma 1. $I(X;Y) = I(S;W)$ *for the communication system in Figure 3.8.*

Proof. For the communication system in Figure 3.8 we have the Markov chain $X \leftrightarrow S \leftrightarrow W$. Thus, based on the data processing inequality [137], $I(S;W) \geq I(X;W)$. Since VNT is a deterministic injective function (i.e., $f(s) > 0$ and consequently $T(s_1) > T(s_2)$ for $s_1 > s_2$), the Markov chain $S \leftrightarrow X \leftrightarrow W$ also exists, and therefore $I(X;W) \geq I(S;W)$. Consequently, $I(X;W) = I(S;W)$. Similarly, for the two Markov chains $X \leftrightarrow W \leftrightarrow Y$ and $X \leftrightarrow Y \leftrightarrow W$, it can be shown that $I(X;W) = I(X;Y)$. Hence, the equation $I(X;Y) = I(S;W)$ is proved. □

Based on this lemma, the capacity of the original channel with signal dependent noise can be expressed in terms of transformed input and output as

$$C = \sup_{\mathsf{E}\{|T^{-1}(X)|^2\} \leq P} I(X;Y). \tag{3.14}$$

Note that the mutual information maximization is performed subject to a transformed average power constraint where P denotes the average power limit in the original channel.

The following section will study the capacity of the CS channel defined in (3.5) based on the

assumption that the signal bandwidth is not greater than the bandwidth for which the spectral density of noise remains constant, and consequently noise can be considered as white. In effect, using VNT, the CS channel can be transformed into an AWGN channel. We will further discuss the effect of correlation of noise in CS later.

3.4.2 Capacity of signalling on CS

The statistical behaviour of the noise in nonlinear spectral domain has been investigated concluding that the noise becomes signal-dependent and non-Gaussian in CS. In addition, real and imaginary parts of the noise in CS are dependent. In this section, we first consider real CS signalling ($\Im\{\rho_0(\lambda)\} = 0$), for which the noise variance is only dependent on the signal amplitude, and employ VNT as a tool to estimate the capacity of CS channel. We can then provide a bound for the capacity of complex signalling on CS.

We first start with the following theorem to show that if the dependency of the noise variance to signal is defined by a polynomial with an order higher than two, the signal space in the transformed channel (i.e., $X = T(S)$) is not only limited by the transformed average power constraint in (3.14) but also by an imposed peak power constraint. Note that both asymptotic analytical result in equation (3.9) and simulation results in Figure 3.5 confirm that the variance of noise in CS is dependent to signal's amplitude by a polynomial of order higher than 2.

Theorem 1. *Let the dependency of the variance of noise to the amplitude of the real valued signal s be approximated by a polynomial $f(s) = a_n|s|^{b_n} + a_{n-1}|s|^{b_{n-1}} + ... + a_1|s|^{b_1} + a_0$, where $a_i \geq 0$ for $i = 0, ..., n$ and $b_n > b_{n-1} > ... > b_1$ are not necessarily integers. Then, the transform function, $T(\cdot)$ defined in (3.11) is bounded if $b_n > 2$.*

Proof. It should be noted that the transform properties imposes $T(0) = 0$. For large values of $s > \Gamma > 0$ the polynomial can be approximated by its largest order, and thus for $\nu > 0$

$$\begin{aligned} T(\nu) &= \int_0^{\nu} \frac{1}{\sqrt{f(s)}} \mathrm{d}s \\ &\leq M_\Gamma + \int_\Gamma^{\nu} \frac{1}{\sqrt{a_n s^{b_n}}} \mathrm{d}s \\ &= M_\Gamma + \frac{1}{(1-b_n/2)\sqrt{a_n}} t^{\frac{-b_n}{2}+1} |_\Gamma^\nu \\ &= A_\rho + \frac{1}{(1-b_n/2)\sqrt{a_n}} \nu^{\frac{-b_n}{2}+1}. \end{aligned} \tag{3.15}$$

where M and A_ρ are finite values, and

$$M_\Gamma = \int_0^{\Gamma} \frac{1}{\sqrt{f(s)}} \mathrm{d}s,$$

$$A_\rho = M_\Gamma - \frac{1}{(1-b_n/2)\sqrt{a_n}} \Gamma^{\frac{-b_n}{2}+1}.$$

It can be further shown that

$$\lim_{\nu \to \infty} \nu^{\frac{-b_n}{2}+1} = \begin{cases} \infty & b_n \leq 2 \\ 0 & b_n > 2 \end{cases},$$

Considering the limit above and noting that the second term in (3.15) is negative for all $b_n > 2$, we can write $T(\nu) \leq A_\rho$. Replacing variable s with $-s$ in the equations above, it can be also shown that $T(\nu) \geq -A_\rho$ for $\nu < 0$. Finally, we can conclude that

$$|T(\nu)| \leq A_\rho$$

□

Note that VNT reveals an important consequence of the signal-dependency of the noise with an order higher than two which renders the signal space further limited by a peak power constraint. In other words, the signal dependency in nonlinear spectral domain is translated to peak-power-limited signal space in the transformed domain.

Applying the theorem above to the asymptotic statistics of the CS channel in (3.9), the signal

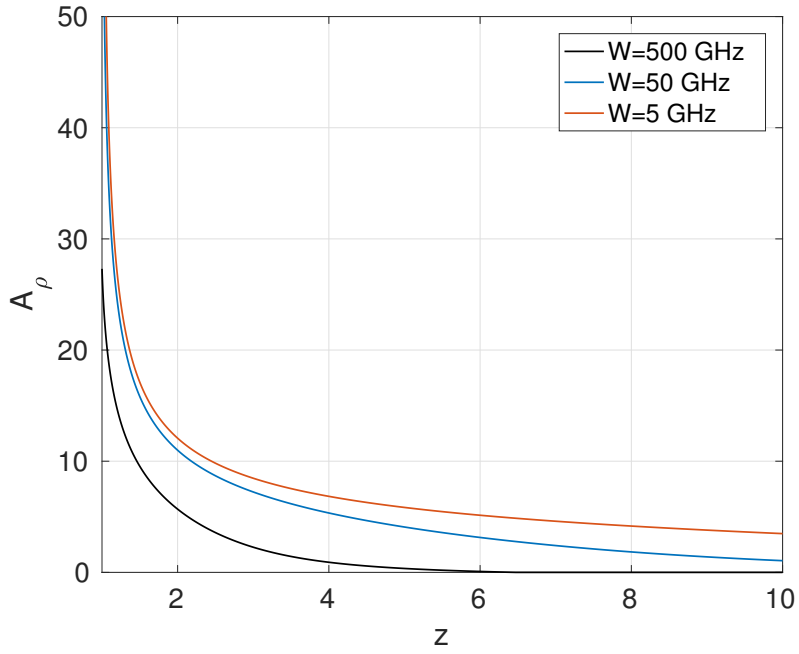

Figure 3.9: Asymptotic value of normalized peak amplitude constraint A_ρ for different signal bandwidth and normalized link length.

amplitude in the transformed channel is limited by

$$A_\rho = \int_0^\infty \frac{1}{\sqrt{(s^2+1)\left(\frac{(s^2+1)^{\frac{4\pi z}{c_\rho}}}{c_\rho \sigma_0^2} - 1\right)}} \mathrm{d}s, \tag{3.16}$$

which is determined by channel parameters z and c_ρ which are related to fibre length, signal bandwidth, and ASE noise spectral density. Note that although the value of A_ρ in (3.16) is only accurate at asymptotic regimes but it gives some insight about how the maximum value of signal in the transformed channel and consequently the capacity depends on the channel parameters. For instance, for longer fibre links the limiting amplitude would be smaller because the noise variance is higher. This is shown in Figure 3.9 for different bandwidths of signal. The same parameter as before are used here for calculating noise variance σ_0^2. It can also be seen that higher bandwidth limits A_ρ more becasue of increased dispersion and consequently larger noise variance in CS.

Here, some numerical results are presented on the effectiveness of the VNT approach before finalizing the capacity analysis. Figure 3.10 depicts the variance normalizing transforms

required to normalize the signal-dependent noise in CS for different fibre lengths. These are obtained directly from the simulation results, shown in Figure 3.5, without any approximation. It can be seen that the transforms are limited to certain values. For instance, maximum amplitude A_ρ for fibre lengths $L = 1000, 2000,$ and 3000 km are respectively 28.63, 14.35, and 9.11. Therefore, in the AWGN channel resulted from the VNT, the signal amplitude cannot be higher than a specific value determined by VNT.

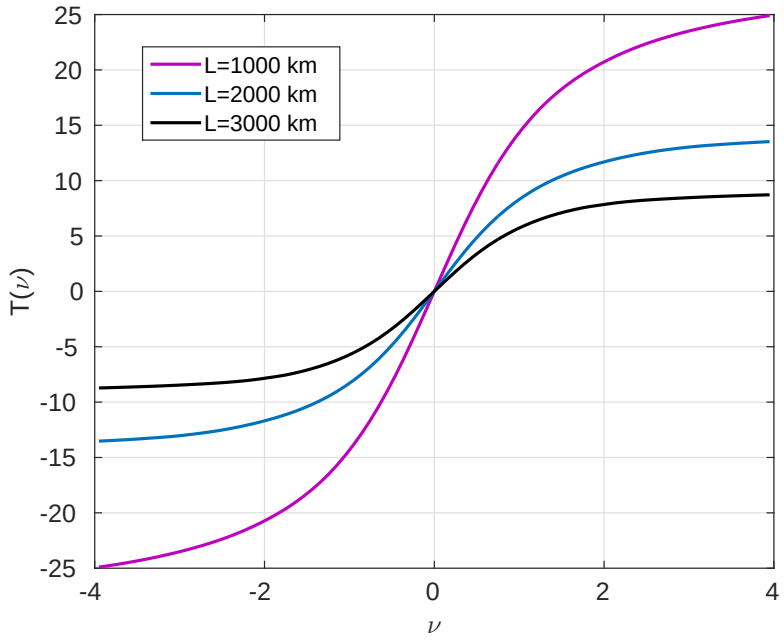

Figure 3.10: Variance normalizing transform for different fiber lengths.

In order to demonstrate the effectiveness of the VNT, the transform is performed on a symbol with amplitude $\rho_0 = 2$ for a 2000 km fibre. Applying the VNT the PDF of transformed samples tend to Gaussian distribution with mean $T(2) = 11.6$ and variance of approximately equal to one as demonstrated in Figure 3.11a. The quantile-quantile plot in Figure 3.11b confirms this statement.

Now, it is time to establish some results on the capacity of the CS channel. Letting $W = \tilde{\rho}_L(\lambda)$, $S = \rho_0(\lambda)$, and $N = \eta_L(\lambda)$ and considering Figure 3.8, the capacity of the CS channel can be derived based on the capacity of the equivalent AWGN channel in (3.13) as in (3.14). Assuming real signalling on CS, the variance of the noise N is dependent to the amplitude of signal S with a polynomial of an order higher than two. Therefore, based on the theorem presented

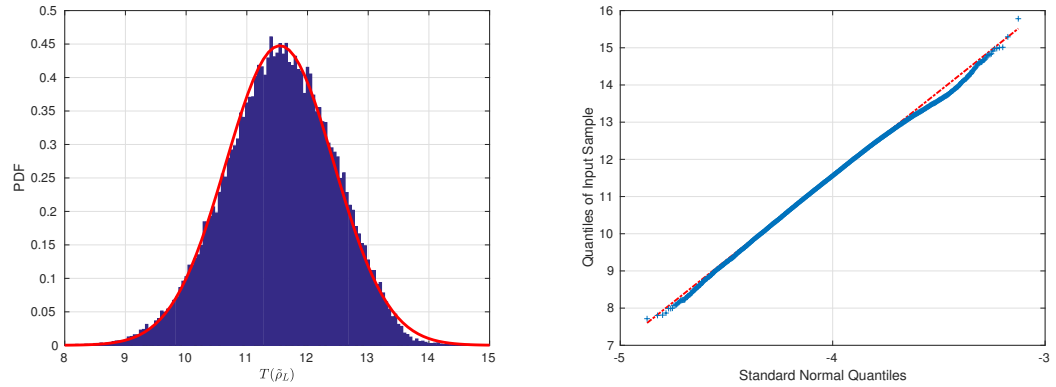

(a) (b)

Figure 3.11: (a) Probability density of transformed received signal when the noise-free amplitude is equal to 2. (b) quantile-quantile plot for the 2 samples.

earlier, the real signal space of the transformed CS channel is limited not only by an average power constraint but also by a peak amplitude constraint. Hence, (3.14) needs to be modified to determine the capacity C_R of the real CS channel by maximizing mutual information for the transformed AWGN channel with both peak amplitude and average power constraint as

$$C_R(P, A_\rho) = \sup_{\mathsf{E}|T^{-1}(X)|^2 \leq P, \quad |X| \leq A_\rho} I(X;Y). \tag{3.17}$$

The optimization problem (3.17) gives the capacity of a scalar Gaussian channel with peak and average power constraints. The average power constraint is modified according to the variance normalizing transform, but still has the same effect on the optimization problem. Obviously, a peak power constraint imposes a maximum for the capacity of channel at large average signal power because the average power cannot exceed the peak power. More importantly, as proved in [138], the introduction of the peak power constraint in problem (3.17) leads to a capacity-achieving input distribution that is a finite set of discrete points. For each fixed amplitude limit A_ρ, an optimal capacity-achieving input distribution exists which satisfies certain necessary and sufficient conditions [138]. Furthermore, it is known that this optimal distribution is discrete with finite number of points. The unknown variables are the number of points, their position, and the probability at each point. Therefore, the original problem of an optimal input distribution for the maximum average mutual information is essentially reduced to determination of a finite number of values (i.e., positions and probabilities). If the

number of points are known, called N_C, the capacity can be calculated using many available optimization algorithms for maximization of a function (i.e., mutual information) over a vector of size $2N_C$. This unknown vector is defined in a well-restricted region since the probability is bounded between zero and one, and the position of points (i.e., signal amplitudes) are also limited by peak amplitude constraint. However, the number of points is generally unknown. Thus, an algorithm can be used that increases the number of points, starting from 2 points corresponding to 4 unknown variables, until all necessary and sufficient conditions are met.

The optimal distribution and the resulting capacity for the CS can be calculated numerically using the algorithm proposed in [138]. Since the signalling is performed in nonlinear spectral domain, the maximum average signal power in CS (i.e., P) is considered as the constraint. However, the actual power in time domain cannot be readily expressed as a function of P. The relationship between P and signal power in time domain will be discussed later.

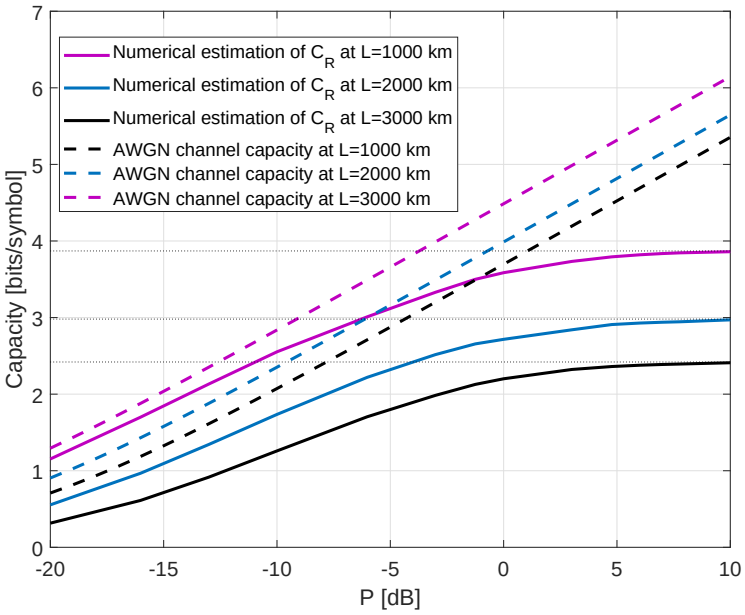

Figure 3.12: Capacity for different fibre lengths.

Figure 3.12 shows the capacity of the real CS channel, C_R, for different link lengths calculated by solving the problem (3.17) using the algorithm provided in [138]. Note that average power constraint needs to be converted to a constraint in the transformed domain. This imposes a modification to the algorithm in [138]. The results clearly demonstrate that the capacity saturates for high signal power for different fibre lengths. Similar saturation effects have been

previously observed for achievable data rates on nonlinear optical fibre channels [9]. The maximum capacity for each fibre length is equal to the capacity without an average power constraint or $P \to \infty$. These values are respectively 3.873, 2.981, and 2.425 bits per symbol for fibre lengths 1000 km, 2000 km and 3000 km. The capacity of an AWGN channel with power P and noise spectral density $\sigma^2 z$, defined in (2.11), is also demonstrated for comparison.

As shown in [138], for high values of A_ρ and P, the capacity-achieving distribution tends to a set of uniformly distributed discrete points for which the capacity can be derived in closed-form as

$$C_R = \log(2A_\rho/\sqrt{2\pi e}). \tag{3.18}$$

For instance, for the 1000 km fiber, the capacity achieving distribution for high average powers is approximately uniform and consequently the capacity tends to $\log(2A_\rho/\sqrt{2\pi e}) = 3.79$ which is close to the value (i.e., $C_R = 3.873$) numerically calculated in Figure 6.4 at high signal power.

In the previous section, it was demonstrated that the noise on real and imaginary parts of CS ($\eta_L^r(\lambda)$ and $\eta_L^i(\lambda)$) are correlated, and increasing real or imaginary amplitude increases the noise variance in both channels. Since, the details of this correlation is not yet known, we use the capacity results of real singling on CS to present bounds on the capacity of the complex CS signalling in bits per complex symbol as

$$C_R(P, A_\rho) \leq C(P, A_\rho) \leq 2\, C_R(P/2, A_\rho). \tag{3.19}$$

where we have used the fact that the real and imaginary channels are identical.

3.5 Approximation of achievable data rates

In the previous section, we derived an estimate on the capacity of CS channel in bits per symbol or, in other words, the capacity of the *discrete-λ channel*. It would be also beneficial to estimate achievable data rates by taking into account available time-frequency resources and addressing *continuous-λ channel* capacity. Due to nonlinear nature of the system, however, we cannot simply apply Nyquist theorem to relate these two quantities. Here, we briefly discuss how

this relationship looks like for the nonlinear fibre channel considering several properties of the NFT-based system.

Note that the simulation results presented in this section are derived based on the same simulation method explained in section 3.3. Here, the width of signal $\rho(\lambda)$ is called spectral width denoted by Λ. Unless otherwise stated, 64 random symbols are considered for CS with $\Lambda = 16$ and $T_0 = 0.1$ ns. Temporal width, bandwidth, and spectral width are calculated as the interval consisting 99% of energy.

3.5.1 Bandwidth

Considering a low power regime, $F(x)$ can be replaced by $\epsilon F(x)$ ($\epsilon << 1$) as the Fourier transform of $\rho(\lambda)$ in GLM equation (see (2.33)). As a result, it can be easily concluded that $q(t) = \text{INFT}\{\rho(\lambda)\} \simeq -2\epsilon F(2t)$. This shows that, for low signal energy, INFT behaves similar to ordinary inverse Fourier transform (IFT). Therefore, the bandwidth of signal after INFT is related to the spectral width as $B \simeq \Lambda/\pi$. For higher power, the INFT causes the bandwidth B to increase beyond Λ/π. Figure 3.13 shows the frequency spectrum of the signal after IFT and INFT for $P_\rho = 13.5$ dB. It is observed that the spectrum of signal after INFT is larger than twice that of IFT.

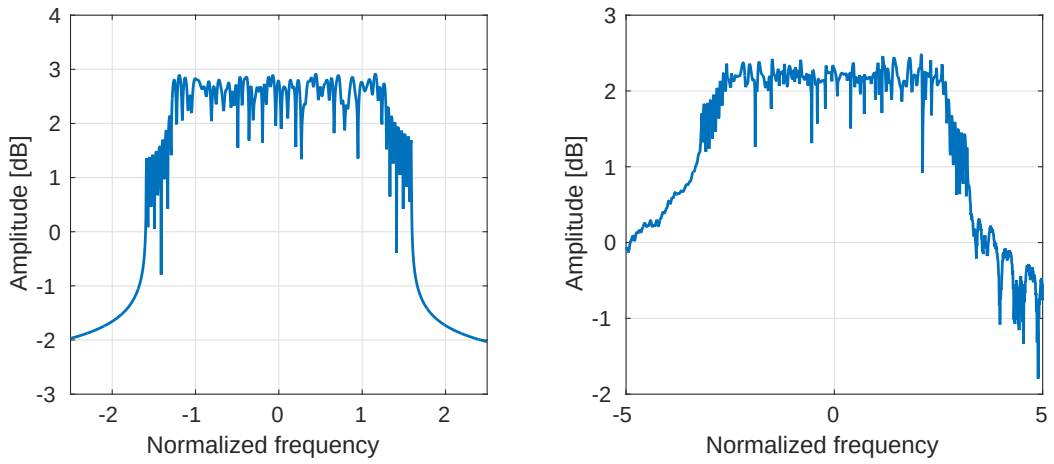

Figure 3.13: (a) Bandwidth of signal after ordinary inverse Fourier transform (IFT) (a) Bandwidth of signal after inverse nonlinear Fourier transform (INFT).

Table 3.1 shows simulation results for bandwidth for different values of signal power in nonlinear spectral domain (P_ρ). It can be seen that for the lowest power value, the measured bandwidth is very close to the actual value of $\Lambda/\pi = 5.09$ and for higher power values B increases. It should be noted that B is the normalized bandwidth, and the actual bandwidth of the signal would be $W = B/T_0$.

Table 3.1: Bandwidth for different CS powers

P_ρ [dB]	-10	-2	4	10	13.5	16
B	5.09	5.11	5.16	5.43	5.62	5.89

Moreover, the bandwidth of signal may increase during propagation along the fibre due to nonlinear spectral broadening [98]. Therefore, both INFT and fibre propagation result in increased signal bandwidth, and consequently, the nonlinear spectral width in CS available for information transmission is limited by the available bandwidth as $\Lambda \leq \pi B$.

3.5.2 Temporal width

Equation (3.3) shows that the width of signal in time domain at the receiver asymptotically equals to $\Delta t_\infty = 4z\Lambda$. This is based on the asymptotic scenario in which the dispersion effect is high and $\Delta T_L >> \Delta T_0$ where ΔT_L is the temporal width of signal at length L. In non-asymptotic distances, this approximation can be used as the added temporal width due to dispersion. Similarly, in linear fibre, the temporal width of signal can be estimated as $\Delta T_L = \Delta T_0 + 2\pi\beta_2 LW$ [98]. Table 3.2 presents the simulation results of the signal temporal width after propagation over different lengths of fibre for $P_\rho = 10$ dB. It is observed that the approximation $\Delta T_L = \Delta T_0 + 4z\Lambda T_0$ is slightly better (i.e., smaller) than the linear approximation in every fibre length because the spectral width $\Lambda \leq \pi W T_0$ is used instead of bandwidth W. Consequently, the effect of nonlinearity is somehow included in the approximation of the temporal width of the signal which leads to better results. Therefore, this estimate can be used to determine the temporal width at the receiver for an NFT-based communication system. Note that based on normalization (2.9) we have $z = L/2L_D$.

Following the linear approximation argument in section 3.5.1, it can be concluded that the temporal width for low power signals can be obtained as $\widetilde{\Delta T_0} = T_0\pi K/\Lambda$ based on Nyquist

Table 3.2: Approximation for temporal broadening

L [km]	z	ΔT_L [ns]	$\Delta T_0 + 4z\Lambda T_0$	$\Delta T_0 + 2\pi\beta_2 LW$
1000	1.05	8.62	10.57	11.04
3000	3.15	22.12	23.98	25.36
6000	6.30	42.82	44.09	46.84

theorem and denormalizing by T_0. Here, K is the number of symbols. However, when the signal power increases in nonlinear spectral domain, the temporal width after INFT increases beyond this linear estimate. Table 3.3 presents a comparison between the actual measured temporal width of signal after INFT and the linear estimate. Parameter $r = \Delta T_0/\widetilde{\Delta T_0}$ is defined which demonstrates the excess temporal width due to INFT. It can be seen that r increases beyond 1 as the signal power increases. It is also observed in Table 3.3 that the power in spectral domain (P_ρ) and time domain (P_q) are not linearly related. For instance, P_ρ increases 6 dB for twice the amplitude, but this is not the case for P_q. As a matter of fact, the power in time domain increases slowly compared to the power in nonlinear spectral domain since the temporal width after INFT, ΔT_0, increases for higher CS power. The Parseval's equality for NFT [24] when considering only CS gives an insight on this effect as the square of temporal signal is related to the logarithm of the square of CS.

Table 3.3: Time domain power and width for different CS powers

P_ρ [dB]	P_q [dBm]	ΔT_0 [ns]	r
-10	-12.12	1.26	1
-2	-5.99	1.47	1.17
4	-3.26	1.94	1.54
10	-1.73	2.59	2.06
13.5	-1.09	2.97	2.36
16	-0.76	3.26	2.56

3.5.3 Achievable rates

In order to estimate the effective data rates, we need to take into account the dispersion effect and the corresponding guard interval required for signal transmission using NFT based systems. We thus introduce a new parameter W_d which determines the number of symbols received per second as

$$W_d = \frac{K}{\Delta T_0 + \Delta T} \quad [\text{symbol/sec}], \tag{3.20}$$

Table 3.4: The effect of number of symbols on the data rate. ΔT_0 [ns], ΔT_L [ns], W_d [Gsymbol/sec], $\widetilde{W}_d$ [Gsymbol/sec] ,R [Gbps]

K	ΔT_0	ΔT_L	W_d	$\widetilde{W}_d$	$R = CW_d$
16	0.92	15.64	1.02	1.14	6.14
32	1.3	15.04	2.13	2.18	12.77
64	2.59	15.29	4.19	4.01	25.12
128	5.51	17.06	7.5	6.93	45.02
256	9.56	20.38	12.56	10.90	75.36

where ΔT is the increase in temporal width because of dispersion and K is number of symbols. Then, data rate in [bits/sec] can be estimated by $R = CW_d$, where C is the complex capacity bound derived in section 3.4.2 as $C = 2C_R$ and the capacity of real signalling, C_R, is shown in Figure 3.12. Parameter W_d can be derived by simulation considering different number of random symbols in a fixed nonlinear frequency interval. For instance, in Table 3.4, W_d is calculated for a 2000 km fibre link and $P_\rho = 10$ dB. It is also possible to estimate W_d based on the approximations for bandwidth and temporal width derived in previous subsections. The temporal width at the transmitter after INFT is approximated by $\Delta T_0 = rT_0\pi K/\Lambda$. Therefore, we have

$$\widetilde{W}_d \simeq \frac{K}{T_0\left(r\frac{\pi K}{\Lambda} + 4z\Lambda\right)}, \tag{3.21}$$

where r is given by Table 3.3, for instance, $r \simeq 2$ for $P_\rho = 10$ dB and $K = 64$. Table 3.4 compares W_d and $\widetilde{W}_d$ and also presents achievable data rate, For instance, $R = 75.36$ Gbps is achieved for $K = 256$. Note that this data rate is achieved taking into account the needed guard interval due to dispersion. This table also shows that increasing K results in higher data rate.

Using (3.18-3.21), a closed-form expression can be written for achievable data rate based on complex signalling on CS as

$$R \simeq C\widetilde{W}_d = \frac{2K\log(2A_\rho/\sqrt{2\pi e})}{T_0\left(r\frac{\pi K}{\Lambda} + 4z\Lambda\right)},$$

which can be simplified for large K as

$$R \simeq \frac{2\Lambda\log(2A_\rho/\sqrt{2\pi e})}{rT_0\pi}. \tag{3.22}$$

Considering the low power regime, we have $r = 1$ and $W = \Lambda/(\pi T0)$, and therefore (3.22) would tend to $R = WC$ where C is in bits per complex symbol which can be originally predicted by Nyquist theorem.

3.5.4 Correlation of noise

In section 3.4.2, we assumed that the noise in CS is white over the signal spectrum. Here, simulation results are presented to investigate the noise correlation. Figure 3.14 shows the average of absolute value of correlation coefficients for noise samples with their neighbouring samples for the fibre length of 2000 km. similar results have been observed for different fibre lengths. It can be seen that as the difference between the frequencies increases, the correlation decreases substantially. For instance, if the distance between two data samples is 0.03 (corresponding to approximately 95 MHz), the noise on the samples can be regarded as uncorrelated. Since the results presented here are based on simulations, part of the observed correlation can be caused by numerical errors in NFT and INFT. Since $\Lambda = 16$, the maximum number of symbols without correlation can be estimated as $K \simeq 512$ which lead to $R \simeq 92$ Gbps based on the capacity and achievable rate results.

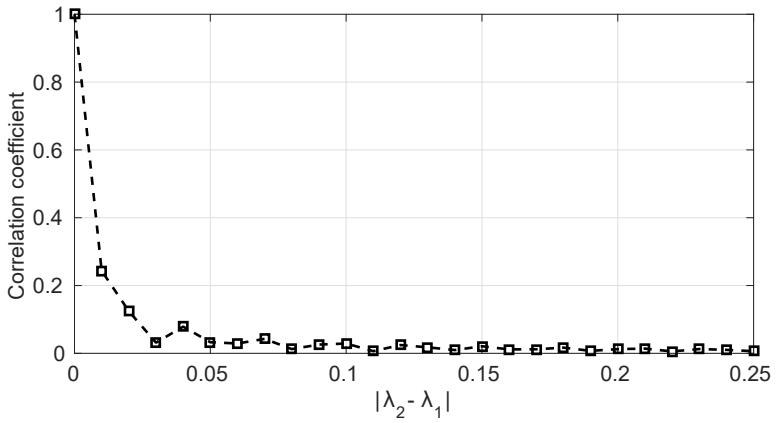

Figure 3.14: Average correlation coefficient plotted for frequency differences.

3.6 Summary

In this chapter, the noise characteristics of the channel for CS in NFT-based optical fibre communication systems were studied. The channel characteristics were derived analytically and confirmed by simulation. The noise for CS channel was observed to be dependent

on the signal amplitude by a polynomial with an order larger than two. Applying a variance normalizing transform, it is observed that the signal dependency of noise leads to peak-power-limited signal space. As a consequence, the CS channel capacity is saturated for high powers. However, it was demonstrated that remarkable data rates can be achieved by only signalling on CS.

Chapter 4

Signal processing techniques for the continuous spectrum

This chapter studies different signalling techniques for the continuous spectrum (CS) of nonlinear optical fibre defined by nonlinear Fourier transform (NFT). First, the effect of chromatic dispersion on the data rate and noise in nonlinear spectral domain is investigated, and an optimization method for minimizing such effect is suggested. Also, three different signalling techniques are proposed based on the specific noise behaviour in nonlinear spectral domain. The proposed methods, along with the basic signalling described in previous section, are compared in terms of error performance, distance reach, and complexity. At the end a simple but effective pre-compensation method is presented for further reducing the dispersion effect and improving data rates.

Different techniques were used for mapping data symbols on CS and detecting the received symbols. For instance, in [43, 44], data is directly mapped on the CS and detected by sampling or matched filtering. In a series of other research papers [38–42], nonlinear inverse synthesis was proposed and investigated numerically and experimentally. In this method, the linear spectrum of a predefined time domain signal (e.g., OFDM or Nyquist) rather than the signal itself is mapped on CS. The important point is that each of the aforementioned methods manifests a unique behaviour and performance level, but this has not been investigated thoroughly in the literature. Therefore, in this chapter, some novel methods are proposed based on the features of the CS channel as well as the effect of chromatic dispersion.

4.1 System model

In the low noise scenario, perturbation theory can be used to determine the characteristics of noisy CS. Recall from chapter 3 that the channel model in the nonlinear spectral domain can be expressed as

$$\tilde{\rho}_L(\lambda) = \rho_0(\lambda) + \eta_L(\lambda), \tag{4.1}$$

where $\tilde{\rho}_L(\lambda) = \rho_L(\lambda)\exp(4j\lambda^2 L/2L_D)$ refers to noisy CS signal after phase shift removal according to (2.26), and $\eta_L(\lambda)$ is a complex non-Gaussian noise, the variance of which is dependent on the initial signal as $\mathsf{E}\{|\eta_L(\lambda)|^2\} = f[|\rho_0(\lambda)|]$, where $f[|\rho_0(\lambda)|]$ can be approximated by a polynomial of order 4 [46]. This means that signals with higher amplitudes experience higher noise variance. Furthermore, the real and imaginary parts of the noise in CS may not be assumed independent after propagation over the nonlinear optical fibre unlike the conventional linear channels, and they can be modelled as $\mathsf{E}\{\Re[\eta_L(\lambda)]^2\} = \mathsf{E}\{\Im[\eta_L(\lambda)]^2\} = f[|\rho_0(\lambda)|]/2$. However, in many practical scenarios, the noise can be assumed white, i.e., $\mathsf{E}\{\eta_L(\lambda)\eta_L^*(\lambda')\} = f[|\rho_0(\lambda)|]\delta(\lambda - \lambda')$. The linearising effect of NFT makes the channel model of a nonlinear optical fibre much less complex in CS as in (4.1) than in time domain governed by NLSE (2.8). Nonetheless, due to the special statistical behaviour of the noise, novel techniques are required for capacity estimation, as we addressed in chapter 3, and signalling, which is the subject of this chapter.

The block diagram of the system is the same as chapter 3 (see Figure 3.1). We use complex modulation using sinc pulses as expressed in (4.2), where D_0^i is the ith symbol from vector $\mathbf{D}_0$.

$$\rho_0(\lambda) = \sum_{i=1}^{K} D_0^i \mathrm{sinc}(\frac{K}{\Lambda}\lambda + \frac{K}{2} - \frac{2i-1}{2}). \tag{4.2}$$

The width of CS signal in nonlinear spectral domain is called nonlinear spectral width and is denoted by Λ. Using sinc pulses for pulse shaping make the signalling spectrally efficient by placing the data symbols as close as possible together without introducing any additional required bandwidth similar to the OFDM. Note that the NFT operation at the receiver is only required at K symbol points $\lambda_i = -\frac{\Lambda}{2} + (2i-1)\frac{\Lambda}{2K}$.

For a given input symbol vector $\mathbf{D}_0$, the question arises that in what rate should the symbols be placed in nonlinear spectral domain. In other words, how should we choose the nonlinear spectral width of the signal, Λ, and if there is any optimal value for it? Note that this question originally arises since we are signalling in the nonlinear spectral domain, which does not have a linear duality with the time domain, unlike conventional OFDM systems. To answer this question, the effects of chromatic dispersion on data rate and performance of NFT-based systems are investigated in section 4.2. Furthermore, due to the signal-dependency of the noise in this domain, conventional signal processing techniques are no longer as efficient, and thus, new techniques are studied in section 4.3.

4.2 Dispersion effects and the optimum value of nonlinear spectral width

By mapping the data only on CS soliton formation is suppressed. In the absence of DS (e.g., solitons), the mechanism of cancellation of dispersion with nonlinearity no longer exists, and consequently excessive temporal broadening is expected. Therefore, large guard bands are necessary to avoid mixing of neighbouring signals [39, 40, 42]. This reduces the effective data transmission rate in bits per second. In this section, the effects of chromatic dispersion on NFT-based communication systems are evaluated. Note that, throughout this section, "bandwidth" refers to the width of Fourier transform of the time domain signal $Q_l(\tau)$ (i.e., linear bandwidth) rather than the width of $\rho(\lambda)$ in nonlinear spectral domain. Furthermore, the width (temporal or spectral) are calculated at the window, which consists 99.5% of signal energy. Using this definition, the numerical error due to truncation of the time domain signal is negligible.

Chromatic dispersion is an important effect, which cannot be avoided in time domain in current NFT-based systems because, based on the inverse scattering theorem, the signal in time domain needs to be separated from consecutive signals so that the NFT operation works properly and linearises the channel. The effect of dispersion is removed only after NFT operation (i.e., phase shift in the CS), and thus the broadening in time domain cannot be ignored. Therefore, it is beneficial to know how the broadening can be minimized in order to maximize the effective data rate. As an initial estimate on the dispersion effect, we consider the linear fibre channel as

in section 2.1.1, where broadening factor is derived for Gaussian pulses assuming a linear fibre. It is shown that an optimum initial temporal pulse width (or pulse rate) exists that minimizes the broadening effect of chromatic dispersion while the dispersion effect increases for a higher bandwidth and fibre length. The same phenomena can be also observed for the NFT-based system when the data is modulated on the CS.

For a given input symbol vector $\mathbf{D}_0$ with fixed number of symbols K, the signal bandwidth is directly related to the nonlinear spectral width Λ as explained in section 3.5.1. Similar to the argument about a single Gaussian pulse in the linear regime, it is expected that, for a fixed K, Λ (or, in other words, the symbol rate) can be adjusted to minimize the received temporal width of signal. The existence of an optimum nonlinear spectral width Λ in NFT-based systems can be shown through the asymptotic analysis presented in 3.2. Assuming the data is modulated on CS with the nonlinear spectral width Λ, the initial temporal width of the signal in time domain (after INFT and at $L = 0$) can be estimated as $\widetilde{\Delta T_0} = T_0 \pi K/\Lambda$ for low-amplitude signals by approximating INFT as a linear Fourier transform. When the amplitude of the signal increases this temporal width increases and cannot be accurately determined using the linear estimation any more. Recalling the parameter r as the ratio between the actual temporal width after INFT compared with the linear estimation above (i.e., $r = \Delta T_0/\widetilde{\Delta T_0}$), the actual temporal width can be expressed as $\Delta T_0 = rT_0\pi K/\Lambda$, where r has been shown to be increasing as a function of the signal power in nonlinear spectral domain and it is independent of Λ. In asymptotically long fibres, the received temporal width at length L denoted by ΔT_L can be expressed by

$$\Delta T_L = \frac{rT_0\pi K}{\Lambda} + 4zT_0\Lambda, \tag{4.3}$$

It can be readily seen from (4.3) that the received temporal width ΔT_L can be minimized at $\Lambda = \sqrt{r\pi K/4z}$. Consequently, for a given sequence of K CS symbols containing fixed amount of information, an optimal Λ (or equivalently symbol rate) can be selected to minimize the required guard interval leading to higher packet rates and effectively higher data rates in bit per second.

It can be also confirmed numerically that an optimal value exists for spectral width Λ that minimizes ΔT_L in practical (non-asymptotic) scenarios. The same can be shown for linear bandwidth BW since BW and Λ are directly related. Assuming that $K = 128$ random QPSK

modulated symbols are mapped on CS using sinc pulses as in (4.2), Figure 4.1 shows the existence of the optimal bandwidth for different fibre lengths. The optimal bandwidth decreases for longer fibres. Furthermore, it is confirmed that the initial width (i.e., ΔT_L at $L = 0$ km) decreases when the bandwidth increases. It is also confirmed by simulation that r is constant for all values of spectral width Λ (or bandwidth BW). Signal power in nonlinear spectral domain used in this simulation corresponds to $r = 1.99$.

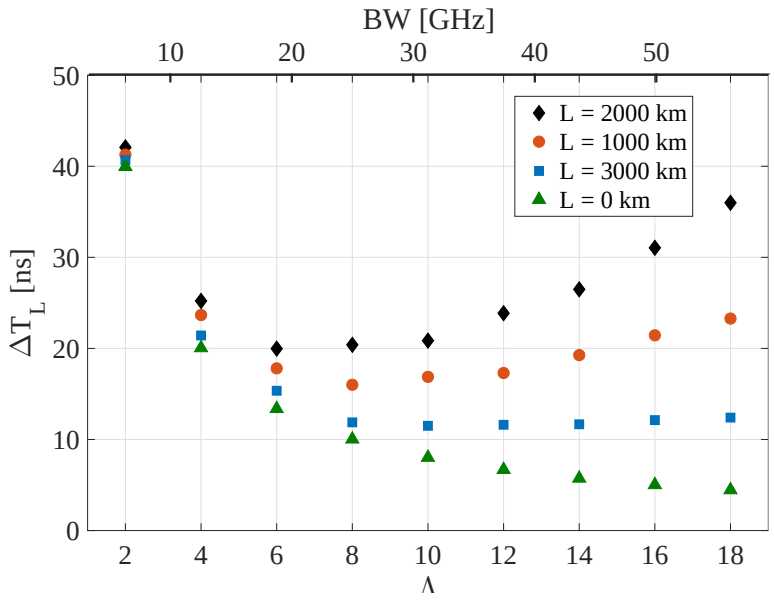

Figure 4.1: The temporal width of the propagated signal after distance L for different BW and Λ.

It should be noted that, as stated in Table 3.4, by increasing K, the effect of dispersion can be reduced and higher overall data rates are achieved even when Λ remains fixed rather than being adjusted to the optimal value for the new K. On the other hand, the computational complexity increases for larger K and thus K and Λ (or bandwidth) should be optimized based on the trade-offs between performance metrics such as computational complexity and effective data rate. Such optimization problems will be the subject of future research.

Another crucial consequence of minimizing the received temporal width by choosing the optimal value for Λ is the noise reduction in nonlinear spectral domain, which may lead to higher achievable data rates by reducing the number of errors. In NFT-based systems, each single sample of data at a nonlinear frequency λ receives signal and noise contributions from all the components within the received temporal width of signal. Therefore, a larger received temporal width results in higher noise in nonlinear spectral domain. This is similar to ordinary

linear communication systems, in which the noise power in time domain is directly related to the signal bandwidth. In effect, if the received temporal width, over which the NFT operation is performed, shrinks, the effective noise added to CS in nonlinear spectral domain decreases.

Here, a simulation is performed for different values of $\Lambda = 4, 8, 12$, which shows that the largest received temporal width (corresponding to the smallest $\Lambda = 4$) results in higher noise in nonlinear spectral domain. Figure 4.2 illustrates this result by plotting the noise variance for different values of Λ against the amplitude of the signal, which also shows the signal dependency of the noise. The results in Figure 4.2 demonstrate that the noise induced in nonlinear spectral domain is directly related to the received temporal width at any amplitude of CS. This figure is obtained by calculating the noise variance for more than 2×10^6 symbols (2×10^7 samples) in different nonlinear frequencies. Figure 4.2 suggests that choosing the optimum Λ not only minimizes the dispersion effect, but also reduces the noise. Therefore, improved error performance and achievable data rate is expected.

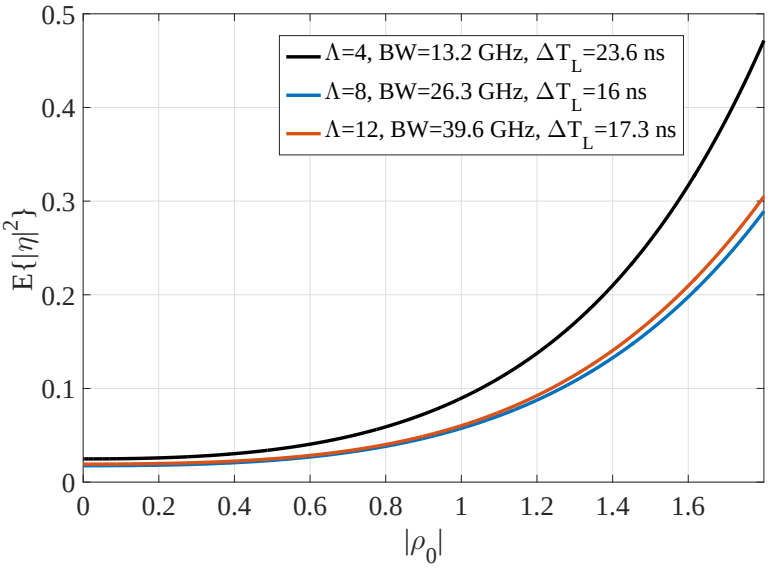

Figure 4.2: The variance of the noise in nonlinear frequency domain for different Λ

4.3 Signalling methods

In this section, different methods of mapping data on CS are investigated. In order to properly understand the effect of signal dependent noise, a ring constellation is used for modulation. It

should be noted that even in conventional fibre optic systems ring constellation is a popular choice [9, 139, 140]. In this section, three different methods are introduced for performance enhancement of the continuous spectrum channel (4.1). The method "direct mapping on CS" refers to the block diagram shown in Figure 3.1 and channel model (4.1). Unless otherwise stated, $K = 128$ random symbols are mapped on CS using sinc pulses as in (4.2) for $\Lambda = 8$. The fibre length is $L = 2000$ km and the signal bandwidth is 26 GHz.

4.3.1 Nonuniform signalling

Using nonuniform levels for constellation diagram is an effective method for improving the performance of a channel with signal-dependent noise [139, 141]. If the statistics are known, the optimum levels can be found by solving an optimization problem such as minimization of BER. For the CS channel model (4.1), unfortunately, a closed-form description of the noise statistics is not known. Therefore, deriving and solving an optimization problem for this channel would be cumbersome. Here, we propose another approach based on the variance normalizing transform (VNT) which was used in chapter 3 as a tool to approximate the capacity of CS channel.

Applying VNT to the noisy signal $\tilde{\rho}_L = \rho_0 + \eta_L$, we have

$$Y = T(\tilde{\rho}_L) = T(\rho_0 + \eta_L) \simeq T(\rho_0) + \eta_T, \tag{4.4}$$

where η_T can be well approximated as a zero mean Gaussian noise with unit variance independent of the transformed signal $T(\rho_0)$. Consequently, a communication channel can be defined, in which the signal is originally generated in a *transformed* domain and then mapped into the original signal domain ρ_0 using inverse VNT. After transmission through the channel (4.1) and addition of signal-dependent noise η_L, VNT is applied, and the output signal can be expressed as $Y = T(\rho_0) + \eta_T$, which defines a conventional AWGN channel. As in Lemma 1, the capacity of this transformed channel is equal to the capacity of the original channel (4.1) with signal-dependent noise. Moreover, the optimal signalling techniques for the conventional AWGN channels would be also optimum for the transformed channel (4.4).

The analysis above is valid for real signalling on CS and can be extended to complex signalling

only if the real and imaginary channels of CS are independent. However, when signal is modulated on CS, the real and imaginary channels are not independent. Moreover, although the noise on the phase of the signal is not dependent to its mean (i.e., input phase), but it depends on the input amplitude. Therefore, VNT with the scaler form (3.11) can not be applied to the complex plane. However, if only real channel is used ($\Im\{\rho_0\} = 0$), the noise variance would only depend on the mean (i.e., input signal), and VNT would be applicable. The signalling can be performed in the transformed channel, but this requires the forward and inverse VNT to be performed each time a signal is transmitted and received. Alternatively, the nonuniform signal levels defined by VNT and the corresponding decision boundaries required for detection at the receiver can be determined for a known channel at the beginning of the communication and then the determined optimum levels can be used for mapping data on CS.

In this section, first it is assumed that $\Im\{\rho_0\} = 0$, and uniform levels are considered for $T(\rho_0)$. Then, inverse VNT is applied to obtain the nonuniform levels for ρ_0. Then, the complex modulation format is defined on the rings with radius equal to the levels found. This makes our approach a sub-optimal method for complex signalling on CS because of the dependence of real and imaginary channels. Note that the number of constellation points on each ring can be chosen based on the variance of the phase of the noise and the required performance. The variance normalizing transform for the 2000 km link is shown in Figure 4.3a, where it is observed that $T(u)$ converges to 16.32 at $u \to \infty$ implying that a peak amplitude constraint exists for the transformed variable $T(\rho_0)$. In other words, the signal space is limited in the transformed domain because the variance of noise depends on the signal amplitude by a polynomial of order larger than 2 (see Theorem 1). For demonstration purposes, four uniform levels for $T(\rho_0)$ are chosen between 0 and 16.1, and nonuniform levels of ρ_0 are calculated using inverse VNT. The corresponding rings and decision boundaries are shown in Fig. 4.3b. It is expected that if nonuniform levels in Figure 4.3b are used, the error rate will be lower compared to uniform levels with the same average power.

4.3.2 Direct mapping on CS and filtering

The second method, which can potentially improve the performance of NFT-based systems, is the application of linear filtering at the receiver in the original signal space, i.e., continuous spectrum. This method is similar to match filtering when detecting pulse modulation in the

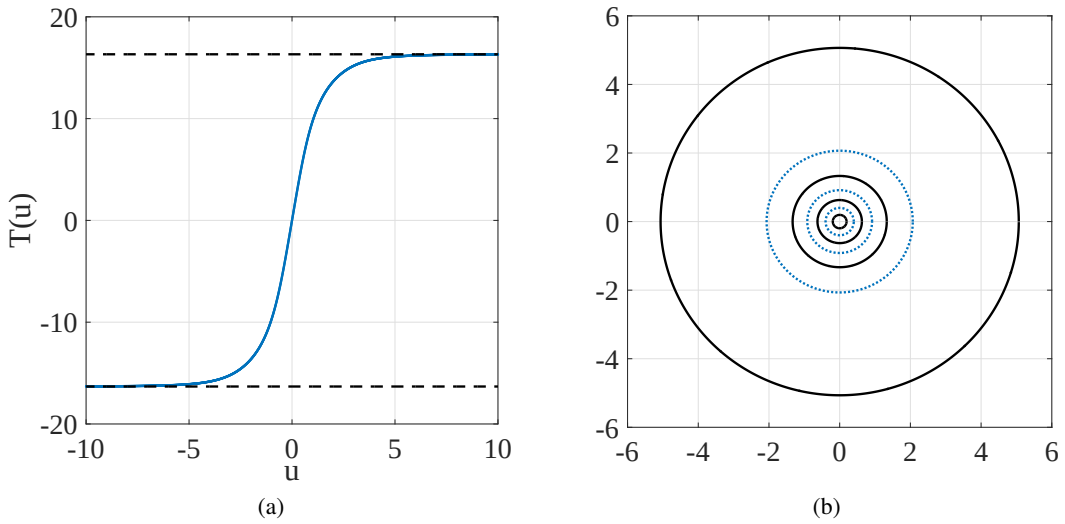

Figure 4.3: (a) Variance normalizing transform for 2000 km (b) Nonuniform levels (solid) and decision boundaries (dotted) derived from VNT.

nonlinear frequency domain [44] and requires oversampling of $\tilde{\rho}_L(\lambda)$ at the receiver. If INFT is applied to $\tilde{\rho}_L(\lambda)$ after removing the dispersion induced phase shift according to equation (2.26), the signal is squeezed into the temporal width of the unpropagated signal $q_0(t)$ because of dispersion compensation in CS and while noise is still present over the uncompensated temporal width of $q_L(t)$. To get back to the signal space, we can then apply an NFT to the time domain signal after windowing the signal component distributed only within the unpropagated temporal width thereby removing the excess noise. However, this method requires complex numerical computation because of the extra NFT/INFT operations on the oversampled signal, and thus, we use ordinary Fourier transform instead of NFT, which allows for linear filtering of the CS signal. In other words, linear inverse Fast Fourier transform (IFFT) is applied to $\tilde{\rho}_L(\lambda)$, the noise out of the signal's window is removed, and then forward linear Fast Fourier transform (FFT) is applied. It should be noted that I/FFT should not be almost equivalent to I/NFT (i.e., asymptotic linear regime) to be effective in noise cancellation as significant amount of noise is observed outside the signal interval even after IFT. In fact, employing FFT and NFT would result in different signal (and noise) power distributions. For example, as explained in section 4.2, so-called low-amplitude and long "tails" [96] typically appear after INFT while compact (finite duration) and much more uniform signal power distribution is observed after linear Fourier transform operation. Therefore, the employment of a simple

constant-gain windowing operation can more effectively mitigate the noise effect for linear filtering compared to the NFT-based filtering which leads to long tails.

Assume $H(t)$ as the ideal filter with width equal to the width of IFFT$\{\rho_0(\lambda)\}$, then the output can be described as

$$\hat{\rho}_L(\lambda) = \text{FFT}\{H(t)\text{IFFT}\{\tilde{\rho}_L(\lambda)\}\}. \tag{4.5}$$

For the simulation, an oversampled version of $\tilde{\rho}(\lambda)$ by a factor of 20 is first generated using NFT, and then $\hat{\rho}_L(\lambda)$ is obtained from equation (4.5). The probability distribution of noise are demonstrated here before and after filtering for signal amplitudes of $\rho_0(\lambda) = 1, 2$. It can be seen that the variance of noise after filtering (Figures 4.5a and 4.5b) is substantially reduced compared to the original noise (Figures 4.4a and 4.4b). Note that although the signal dependency of noise is not eliminated by filtering, its effect is reduced considerably.

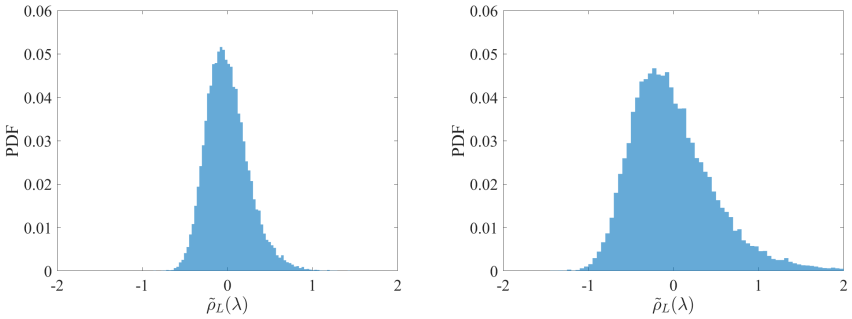

Figure 4.4: The histogram of noise on the CS signal (a,b) $\tilde{\rho}_L(\lambda)$ for amplitudes $\rho_0(\lambda) = 1, 2$.

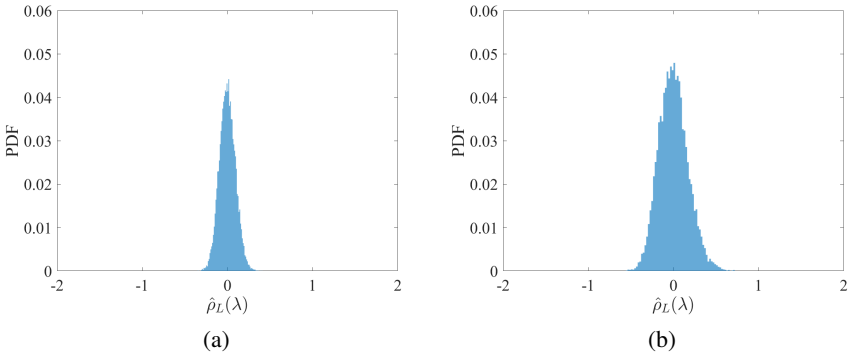

Figure 4.5: The histogram of noise on the CS signal (a,b) $\hat{\rho}_L(\lambda)$ (i.e., filtered signal) for amplitudes $\rho_0(\lambda) = 1, 2$.

4.3.3 GLM-based Signaling

The signal modulated on the continuous spectrum $\rho(\lambda)$ is related to the time-domain signal $q(t)$ by the GLM equation

$$K(x,y)+\int_{x}^{\infty}\int_{x}^{\infty}K(x,s')F^{*}(s+y)F(s'+s)\mathrm{d}s\mathrm{d}s'=F^{*}(x+y), \tag{4.6}$$

where

$$F(t)=\frac{1}{2\pi}\int_{-\infty}^{\infty}\rho(\lambda)e^{j\lambda t}\mathrm{d}\lambda \tag{4.7}$$

is the inverse Fourier transform (IFT) of $\rho(\lambda)$. One can interpret that the GLM equation performs a nonlinear mapping on the linear inverse Fourier transform of $\rho(\lambda)$ (i.e. $F(t)$), so that the time-domain signal $q(t)=-2K(t,t)$ only contains CS and no DS. This means that if GLM is applied to any arbitrary input signal, the output signal would not include any soliton components. Therefore, GLM can be used as a transformation, based on which a signalling method can be designed for the CS channel.

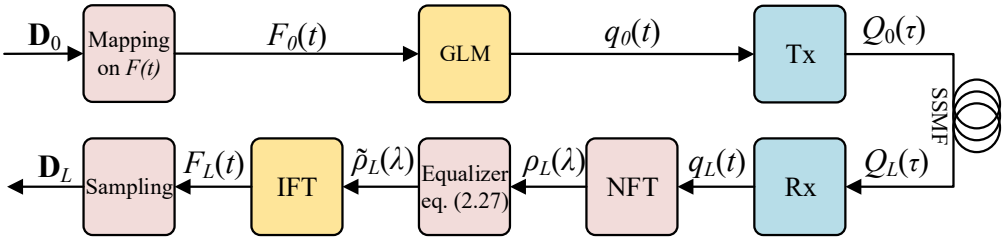

Figure 4.6: The block diagram of the GLM-based signalling system.

In this section, a NFT-based structure is proposed for GLM-based signalling as shown in Figure 4.6. The main difference of the system in Figure 4.6 compared to the direct signalling on CS (as in Figure 3.1) is that the Fourier transform operation included in INFT operation is transferred from transmitter to the receiver, and, effectively, data is mapped on $F(t)$ (i.e., linear Fourier transform of CS) defined as

$$F_0(t)=\sum_{i=1}^{K}D_0^i\mathrm{sinc}(\frac{K}{\tau}t+\frac{K}{2}-\frac{2i-1}{2}), \tag{4.8}$$

where τ is the corresponding signal window in time domain determined based on system constraints, such as bandwidth and power. Consequently, an IFT block is needed at the receiver after NFT operation to return to the original signalling space, where the noisy version of (4.8) is sampled at the center of pulses and are decoded to the original data. It should be also noted that this GLM-based signalling using sinc pulses is in fact equivalent to the nonlinear inverse synthesis method with Nyquist pulse shaping studied in [39–42]. However, either in (4.2) or (4.8), using sinc pulse shapes are not necessary, and more efficient pulse shapes may be found by optimizing the trade-off between performance and numerical error. A similar method was also proposed independently in [142], in which data are mapped on the *kernel of GLM equations* for discrete and continuous spectrum.

Using the law of large numbers, we can show that applying (inverse) Fourier transform on the received CS diminishes the signal dependency of the noise [135] while the probability distribution of the transformed symbols tends to Gaussian according to the central limit theorem [143]. Therefore, conventional modulation and signal processing techniques should perform efficiently if applied in the system illustrated in Figure 4.6.

As discussed in earlier, the variance of noise sample on CS, $\eta_L(\lambda)$, depends on the input sample $\rho_0(\lambda) = \mathsf{FT}\{F_0(t)\}$. Let κ denote the number of samples in nonlinear spectral domain, $h_\kappa = \Lambda/\kappa$ be the distance between subsequent samples, and λ_k be the kth sample point. The noise for GLM-based signalling is defined as $\Gamma_L(t) = F_L(t) - F_0(t)$. Therefore, for a given input signal $F_0(t) = \mathrm{IFT}\{\rho_0(\lambda)\}$ and by using the discretized version of (4.7), we have

$$\begin{aligned}
\mathsf{E}\{\Re[\Gamma_L(t)]^2\} &\approx \left(\frac{h_\kappa}{2\pi}\right)^2 \sum_{k=1}^{\kappa}\sum_{p=1}^{\kappa} \mathsf{E}\{\Re[\eta_L(\lambda_k)]\Re[\eta_L(\lambda_p)]\}\cos(\lambda_k t)\cos(\lambda_p t) \\
&= \frac{1}{2}\left(\frac{h_\kappa}{2\pi}\right)^2 \sum_{k=1}^{\kappa}\sum_{p=1}^{\kappa} \delta(k-p) f[|\rho_0(\lambda_k)|]\cos(\lambda_p t)\cos(\lambda_k t) \\
&= \frac{1}{2}\left(\frac{h_\kappa}{2\pi}\right)^2 \sum_{k=1}^{\kappa} f[|\rho_0(\lambda_k)|]\cos(\lambda_k t)^2 \\
&= \frac{h_\kappa \Lambda}{16\pi^2}\frac{1}{\kappa}\sum_{k=1}^{\kappa} f[|\rho_0(\lambda_k)|] + \frac{h_\kappa \Lambda}{16\pi^2}\frac{1}{\kappa}\sum_{k=1}^{\kappa} f[|\rho_0(\lambda_k)|]\cos(2\lambda_k t) \qquad (4.9) \\
&\approx \frac{h_\kappa \Lambda}{16\pi^2}\mathsf{E}\{f[|\rho_0|]\}. \qquad (4.10)
\end{aligned}$$

For the last equality, the law of large numbers can be used (at large κ) so that the first sum term in (4.9) can be described as the expected value of $f[|\rho_0|]$, and the second term tends to zero because of the presence of the cosine term. A similar result can be demonstrated for $\Im[\Gamma_L(t)]$, and it is observed from (4.10) that the variance of $\Re[\Gamma_L(t)]$ and $\Im[\Gamma_L(t)]$ at every sampling time of t are independent of signal $F_0(t)$ at that time. In other words, noise variance is constant for every sample $F_L(t)$ regardless of the original amplitude $F_0(t)$. However, it is clear that the variance of noise $\Re[\Gamma_L(t)]$ and $\Im[\Gamma_L(t)]$ depend on average value of $f[|\rho_0|]$, indicating that higher energy (i.e., higher average power) results in larger noise variance. This will be investigated in terms of error rate in Section 4.4.1. Also, according to the central limit theorem [143], the probability distribution of $\Gamma_L(t)$ tends to Gaussian.

Here, a simulation is performed in order to compare the statistics of the noise added to $\rho_0(\lambda)$ (i.e., direct mapping) and $F_0(t)$ (i.e, GLM-based signalling) after fibre propagation and addition of ASE noise. NFT is applied to the received signal at the output of the fibre, and also an additional IFT operation is performed to obtain the noise on the signal $F_0(t)$. The same simulation parameters as previous sections are used here, and statistics of $\eta_L(\lambda)$ are compared with that of $\Gamma_L(t)$. Note that oversampling ($\kappa > K$) leads to smaller noise variance as a result of averaging effect of Fourier transform operation [135]. From (4.10), it can be seen that smaller h_κ (larger number of samples κ) results in noise reduction. However, in practical scenarios, noise samples become correlated if they are so close to each other as shown in section 3.5.4. Thus, reducing h_κ is effective up to the point, for which the noise samples are correlated. In this simulation and later in this chapter $h_\kappa = 0.01$ is chosen based on observations of noise correlation. In order to investigate the effect of signal dependency two additional parameters are defined, which represent signal-to-noise ratio (SNR) associated with $\rho(\lambda)$ and $F(t)$ at a specific amplitude of x.

$$\mathrm{SNR}_\rho(|x|) = \frac{|x|^2}{\mathsf{E}\{|\eta_L|^2\}|_{|\rho_0|=x}},$$
$$\mathrm{SNR}_F(|x|) = \frac{|x|^2}{\mathsf{E}\{|\Gamma_L|^2\}|_{|F_0|=x}}.$$

Figures 4.7a and 4.7b show the values for SNR parameters defined above. It can be seen clearly in Figures 4.7a and 4.7b that SNR_F is increasing while SNR_ρ has a maximum. Also,

the values of SNR_F are higher than SNR_ρ. Thus, better error performance is expected if data is mapped on $F_0(t)$. Furthermore, the probability distribution for $\Gamma_L(t)$ has a Gaussian-like distribution with constant variance for all signal amplitudes, as shown in Figure 4.8b, while the distribution of $\eta_L(\lambda)$ is non-Gaussian, as depicted in Figure 4.8a. We can therefore conclude that if data is mapped on $F_0(t)$ (i.e. GLM-based signalling), it is distorted by an approximately additive signal-independent Gaussian noise as in the conventional AWGN channels where the underlying uniform amplitude signalling remains efficient. On the other hand, in the direct mapping scheme, the uniform distribution of the symbol amplitudes causes low SNR at higher amplitudes rendering it essentially inefficient at high energy levels.

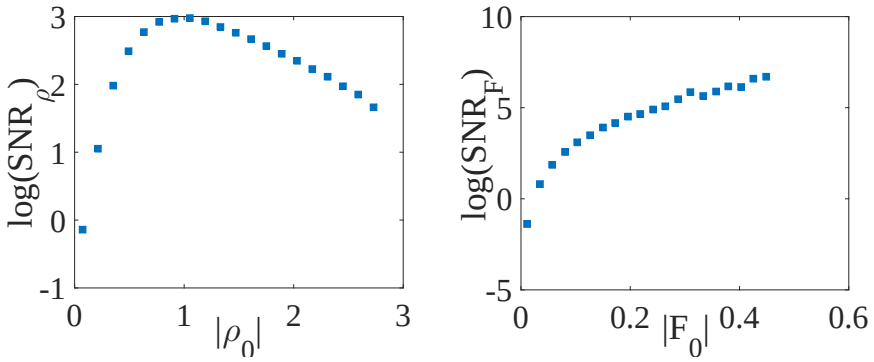

(a) (b)

Figure 4.7: (a) SNR_ρ *for different values of* $|\rho_0(\lambda)|$. *(b)* SNR_F *for different values of* $|F_0(t)|$.

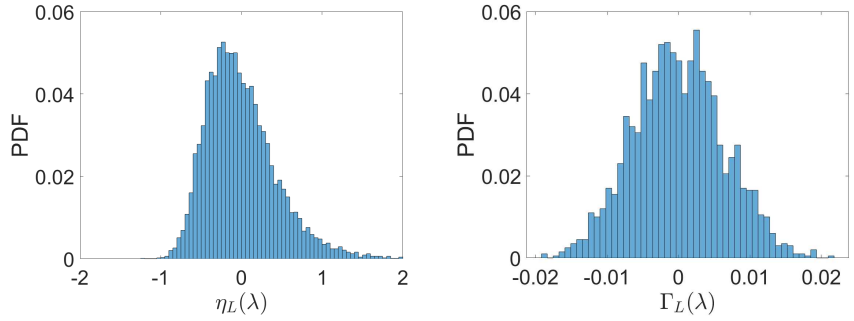

(a) (b)

Figure 4.8: (a) Distribution of noise $\eta_L(\lambda)$ *for* $|\rho_0(\lambda)| = 2$. *(b) Distribution of noise* $\Gamma_L(t)$ *for all values of* $|F_0(t)|$.

4.4 Numerical results and discussions

In this section, we present numerical results on the performance of different signalling techniques discussed earlier for NFT-based systems. Two-ring constellations are used for modulation in order to demonstrate the effect of dependence of noise to the signal amplitude. Unless otherwise stated, 128 symbols are mapped on the nonlinear spectral width of $\Lambda = 8$, which are chosen randomly based on the two-ring constellation. First, the methods described in previous section are compared regarding symbol error rate (SER) only taking into account the error due to noise on the amplitude of two particular symbols. Then, bit error rate (BER) performance is investigated based on different constellation formats on two rings. The performance results are presented against the energy of the CS signal denoted by E. The channel bandwidth is 26 GHz for the simulations.

4.4.1 Error rate performance

In the first simulation, SER is compared for different signalling methods assuming only two symbols on the two rings with an equal phase of zero. This allows us to investigate the effect of signal-dependency of noise. Figure 4.9 shows the received noisy symbols at the end of a $L = 2000$ km fibre for different signalling methods with $E = 2$. Figure 4.9a shows the result for the benchmark scheme, where the symbols are directly mapped on CS as explained in section 4.1. It is observed that the variance of both real and imaginary parts (or amplitude and phase) of the noise is dependent on the amplitude of the original transmitted symbol. Figure 4.9b demonstrates the received symbol for the same energy but for nonuniform levels determined by VNT. In Figure 4.9a, ring radii are 0.8 and 1.6, and the midpoint decision boundary is at 1.2. However, in Figure 4.9b, ring radii are 0.575 and 1.685 with the decision boundary 0.975. Note that the statistics of the noise in CS does not change by applying the VNT method, but the performance improvement is achieved as a results of choosing optimal levels and decision boundary for the rings. For the next two signalling methods in Figures. 4.9c and 4.9d, the magnitude of both amplitude and phase of the noise changes. As shown in Figure 4.9c, when the linear filtering is applied, as described in section 4.3.2, the noise is significantly reduced. For this simulation, an oversampling of 20 CS samples per symbol is considered. Ring radii and decision boundaries are the same as Figure 4.9a. It should be noted that the the noise is

still signal dependent although significantly reduced. Figure 4.9d depicts, the received symbols when GLM-based signalling is employed. The levels are determined so that the energy E is the same as previous methods. It can be observed that the noise statistics are almost uniform for two levels as predicted in section 4.3.3.

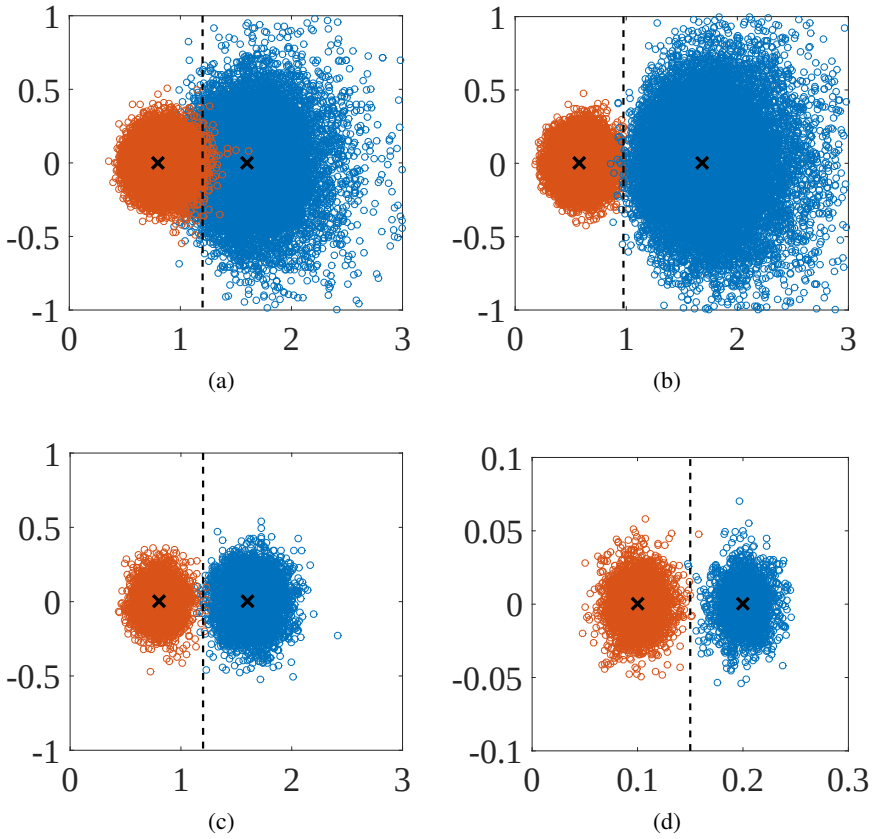

Figure 4.9: Received noisy symbols at $L = 2000$ km based on (a) Direct mapping on CS, (b) Nonuniform signalling, (c) Mapping on CS and filtering, (d) GLM-based signalling.

Symbol error rate for two symbols considered in Figure 4.9 are calculated and shown in Figure 4.10 for different signal energies. It is observed that all proposed methods result in improved performance compared to the direct signalling on CS. The minimum SER is achieved at similar energies for three out of the four methods, but for VNT-based nonuniform signalling the optimum point is different. We conjecture that after $E = 3.7$ the VNT is not effective because the noise variance is very large, and the large mean condition for the VNT is not satisfied. For the filtering method, despite noise reduction, the signal dependency of noise is not eliminated, and thus performance is degraded after a specific energy. For the GLM-based

signalling, although signal dependency is eliminated for a constant energy, the noise variance increases for signals with a higher energy based on (4.10), where higher error rate is expected.

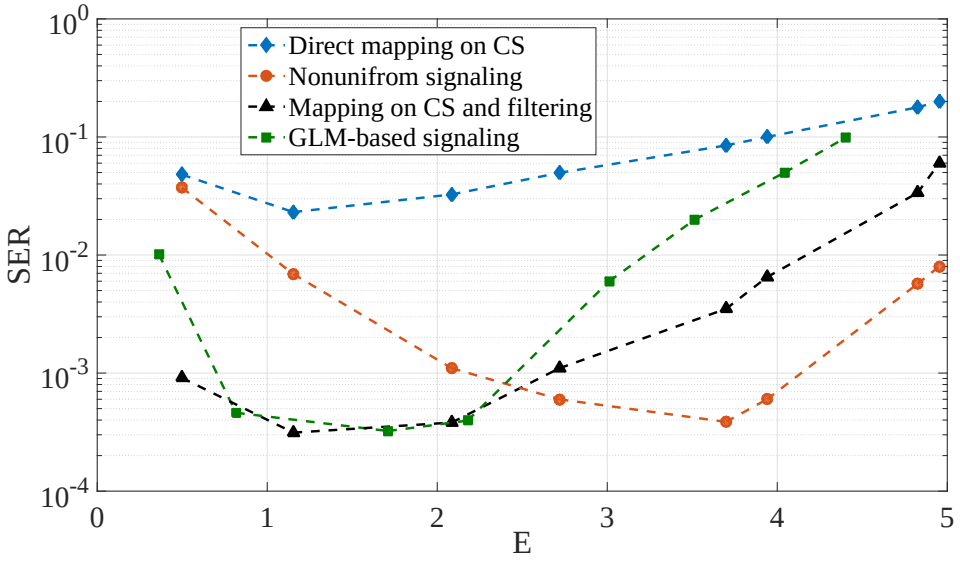

Figure 4.10: SER for different signalling methods on the CS channel.

Here, the BER performance for three different constellation designs based on the two-ring pattern is depicted. In general, lower BER are achieved compared to direct mapping on CS, when each of the proposed methods is employed, and therefore, higher achievable data rates are expected. However, since NFT-based transmission only eliminates the signal-signal nonlinear interactions, it is expected that signal-noise and noise-noise nonlinear interactions in time domain would eventually limit the performance. Soft decision forward error correction (SDFEC) threshold of 2×10^{-2} is also shown in Figures. For constellation (I) in Figure 4.11b, the minimum BER is achieved with similar values for the filtering method and GLM-based signalling. Since the symbols are well separated in each ring the behaviour of BER for different methods is similar to SER in Figure 4.10. Nevertheless, when the outer ring is $\pi/4$ shifted in phase all the methods results in better BER except the nonuniform signalling based on VNT. This is because the decision boundary levels for nonuniform signalling are defined based on the one dimensional (i.e., real) signal space considered in Section 4.3.1, which are not optimum for the complex constellation (II) in Figure 4.12a. An optimal set of decision boundaries could be only determined based on maximum likelihood requiring full analytical description of the noise statistics, which are not available or through exhaustive numerical search. Note that, unlike constellation (II), the decision boundary levels defined based on one dimensional signal space

are nearly optimal for constellation (I) since errors dominantly occur in the radial directions.

In Figure 4.12b, 8 symbols are chosen on each ring, and BER is obtained by simulation. For constellation (III), error originated from the noise on the phase is dominant, which causes the BER for nonuniform signalling not to be as low as other proposed methods. For the GLM-based signalling, the slope of the performance degradation is higher compared to all other methods. This can be explained by referring to equation (4.10). Based on this equation the noise variance increases for higher signal energies with a polynomial of order 4, and this happens equally for all symbol amplitudes. However, for other methods, the inner ring always experiences lower error rate compared to the outer ring resulting in a slower increase of BER on average.

Note that, in this section, operating bandwidth is constant and BER is obtained for various energies, but the effective data rates vary for different signalling methods and constellations. In fact, the required temporal window for NFT operation without numerical error is different for each signal energy E and signalling methods. This happens because of the effect of residual tail at the output of INFT and the different effect of dispersion. For instance, at $E = 2$, taking into account the dispersion effect, for Figures 4.11b and 4.12a the effective bit rate is 21.9 Gpbs for first three methods and 20.7 Gbps for GLM-based signalling, while for constellation in Figure 4.12b these values are respectively 29.2 and 27.6 Gpbs.

The corresponding launch power levels in this section range from -17 dBm to -10dBm. Not that, due to optimization performed for $K = 128$ in Section 3, the dispersion effect is significantly reduced and in turn the nonlinear effect is intensified such that the CS channel with power levels above can reach the high nonlinearity regimes where the BER performances start declining. Assuming a larger K, the optimal bandwidth increases, which leads to higher launch power; however, studying such a scenario would also require dealing with significantly more time-consuming simulation of NFT and INFT operations.

It is worth mentioning that better performance for techniques presented here are obtained with a cost of computational complexity. In order to compare the complexity of different methods, the number of NFT operations at the receiver are taken into account. For direct mapping on CS and nonuniform signalling, the number of NFT operations is equal to the number of symbols, which, in our case, is $K = 128$. For GLM-based signalling, $6 \times K$ samples of $\tilde{\rho}_L(\lambda)$

(corresponding to $h_\kappa = 0.01$) are computed (768 NFT operations) for calculation of $F_L(t)$. Also for the linear filtering method, as stated earlier, $20 \times K$ samples of $\tilde{\rho}_L(\lambda)$ are computed (2560 NFT operations), and also additional FFT and IFFT operations are performed.

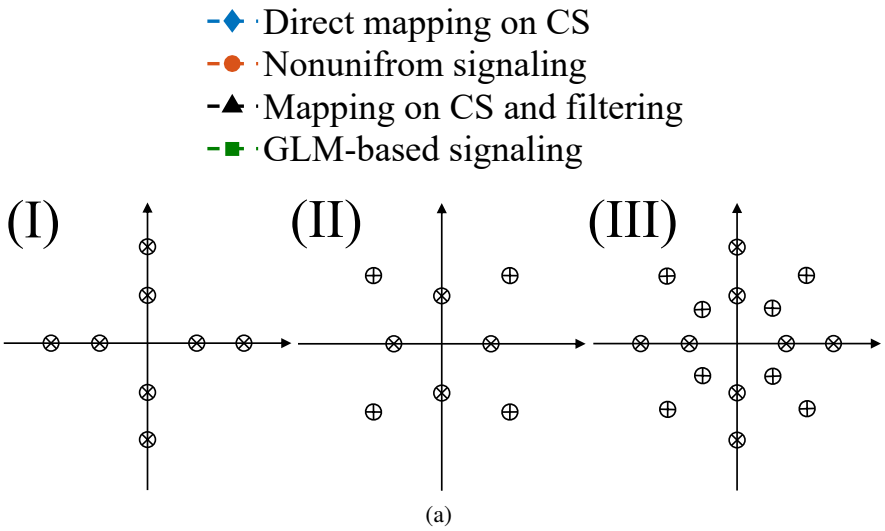

(a)

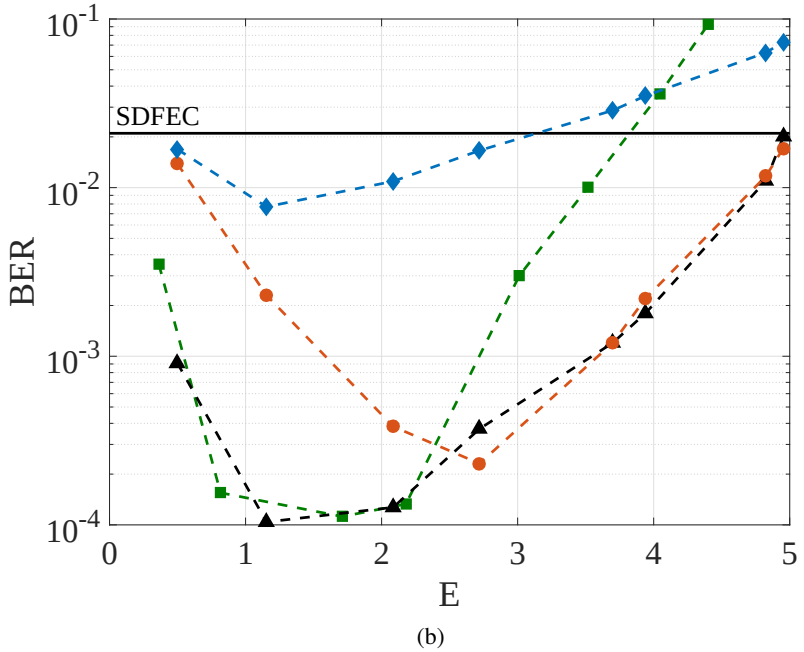

(b)

Figure 4.11: (a) Figure legends and constellation diagrams. (b)BER for different signalling methods at $L = 2000$ km for constellation (I).

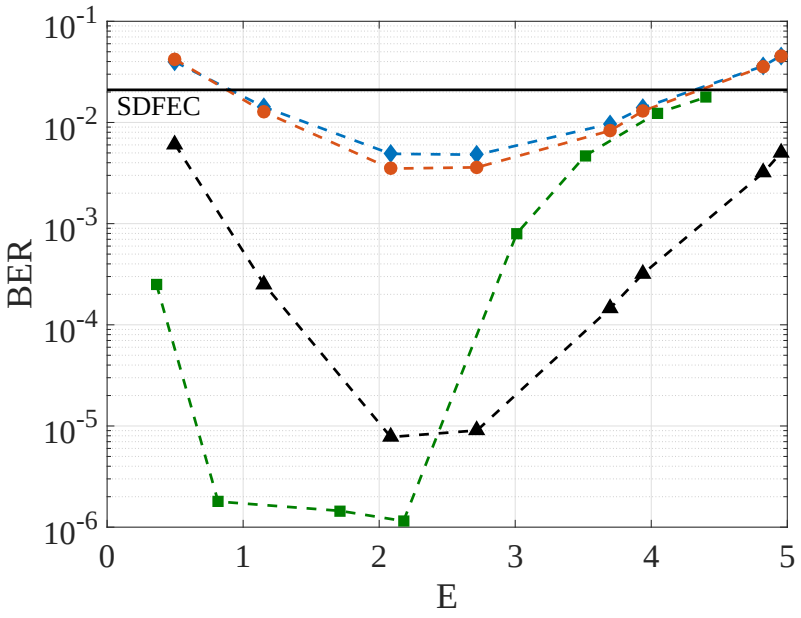

(a)

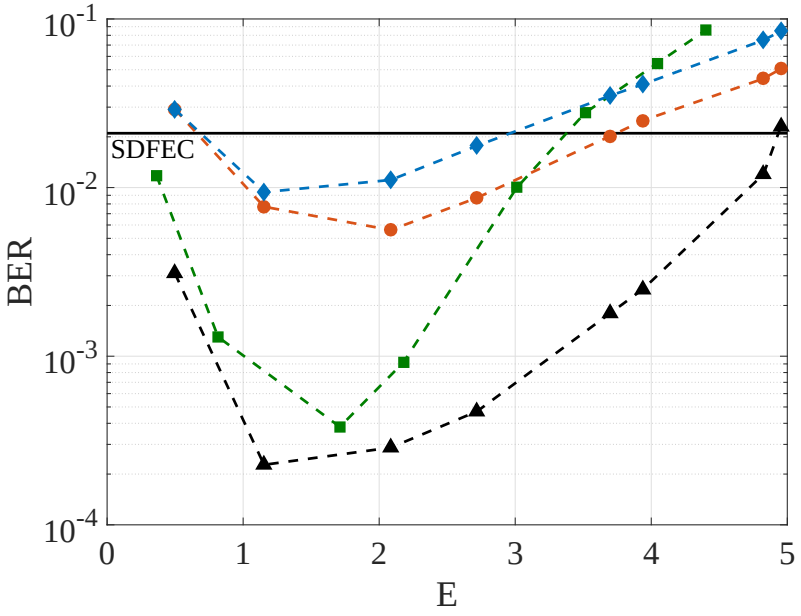

(b)

Figure 4.12: (a),(b) BER for different signalling methods at $L = 2000$ km for constellation (II),(III) respectively. (Legends as in Figure 4.11a)

4.4.2 Reach distance

Considering soft and hard decision FEC thresholds the reach distance are compared for different methods. For all methods shifted constellation (II) in Figure 4.11b is used except

for the nonuniform signalling based on VNT, for which constellation (I) is selected. The input energy E is chosen for the minimum achieved BER figures for each technique. Considering SDFEC and ignoring the redundant bits due to FEC coding, the simulation results demonstrate that distances as long as 7100 km can be reached by applying the linear filtering technique. The effective bit rate at distance 7100 km is 9.6 Gbps. At second place, with GLM-based signalling, a reach distance of about 5900 km with effective bit rate 11.7 Gpbs is obtained. When the levels are optimized using VNT, the achieved reach distance and effective bit rate are 5000 km and 12.7 Gbps. The corresponding values are respectively 3000 km and 18.5 Gpbs for direct mapping on CS. Moreover, considering hard decision forward error correction code (HDFEC) with 7% overhead with threshold of 3.8×10^{-3}, reach distances of 1900, 3300, 4300, and 5300 are achieved respectively for direct mapping on CS, nonuniform signalling, GLM-based signalling, and filtering. It should be noted that, for simplicity and better presentation, E and Λ are considered to be fixed for all fibre lengths and are chosen based on the best performance of a 2000 km link. However, for further performance improvement, E and Λ should be optimized for each individual fibre length. This analysis requires extensive numerical simulation and marginal improvement is expected.

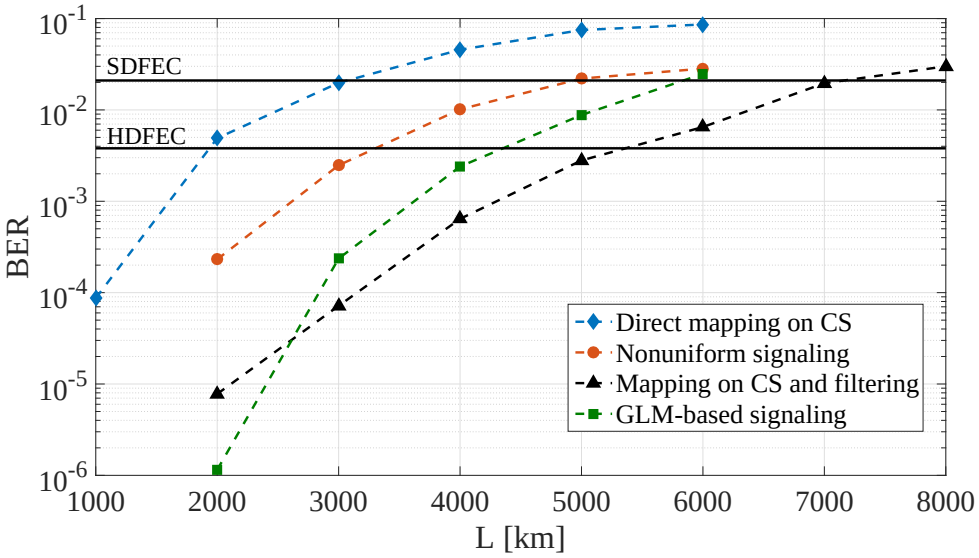

Figure 4.13: Reach distance for different methods

4.5 A dispersion pre-compensation method

It was demonstrated in section 4.2 that dispersion can be minimized by choosing the optimum value of bandwidth for a NFT-based communication system. However, dispersion affects the signal even if the optimum value of bandwidth is picked. Moreover, there might be other reasons that require another system parameter which are not necessarily optimum or near optimum regarding the induced dispersion. Thus, in this section, a dispersion pre-compensation (DPC) method is proposed by pre-equalizing the CS signal by the factor of $\exp(j2\lambda^2 L/2L_D)$ and post-equalizing the received signal with the factor of $\exp(j2\lambda^2 L/2L_D)$. This method can reduce the effective dispersion and increase overall data rate up to 100%. Note that we do not include noise in the analysis of this section.

Assume that the input signal is pre-equalized by an exponential factor as $\rho_0(\lambda).\exp(-j4\lambda^2(-l_1)/2L_D)$, which does not affect the system structure. Consequently, the received CS after propagation over length L of fibre would be equal to $\rho_0(\lambda).\exp(-j4\lambda^2(L - l_1)/2L_D)$, and thus a post-equalization factor as $\exp(+j4\lambda^2(L-l_1)/2L_D)$ yields the original signal. The signal $\rho_0(\lambda)\exp(-j4\lambda^2(-l_1)/2L_D)$ can be regarded as the CS as if the signal is sent backward in the fibre from $l = 0$ to $l = -l_1$. As a result, the signal propagation using DPC over the fibre of length L is equivalent to the propagation of the pre-equalized signal from $l = -l_1$ to $l = L - l_1$. This means that the pre-equalized signal shrinks in the first l_1 meter of the fibre (equivalent to the virtual negative part of the fibre) and then expands until the end of the fibre.

Let ΔT_l denote the temporal width of the signal when the propagation starts from $l = 0$ without DPC. Then, the initial temporal width with DPC would be $\Delta T_{-l_1} = \Delta T_{l_1}$, and it would be equal to ΔT_{L-l_1} at the end of propagation. Therefore, the maximum symbol duration with DPC would be $\max\{\Delta T_{-l_1}, \Delta T_{L-l_1}\}$. It is clear that the optimum value for l_1 is $L/2$ because if the signal is pre-compensated with a value other than $L/2$, either ΔT_{-l_1} or ΔT_{L-l_1} would have a value higher than $\Delta T_{L/2}$, and consequently the effective dispersion would always be higher. As a result, this method effectively reduces dispersion effect such that the effective dispersion using DPC is the same as that of a fibre with length $L/2$. Along with increasing the bit rate, DPC can reduce the peak power of input signal in time domain since the input signal

is already dispersed at the input of fibre. In other words, the peak-to-average-power (PAPR) of the signal at the transmitter is reduced with DPC. This is important because lasers have a limited region of linear operation. Therefore, less PAPR would result in less distortion due to the laser nonlinearity. Note that DPC method has no effect on the Kerr nonlinearity of fibre, and these two types of nonlinearity should not be confused.

Since the amount of dispersion increases with bandwidth or fibre length, it is expected that increasing bandwidth or fibre length would increase the effectiveness of the method because simply the difference between the dispersion of signal at $l = L/2$ and $l = L$ increases. The simulation results for bit rates are compared for systems with and without DPC for different fibre lengths and signal bandwidth. Here, 64 symbols with 16QAM modulation are considered. Figure 4.14 shows the achieved bit rates for fibre lengths from 1000 km to 6000 km. The simulation is performed for a signal with bandwidth of 26 GHz. As expected, the achievable data rate decreases as the fibre length grows, but data rate is significantly higher with DPC. It can be seen that the ratio of bit rate with DPC (R_{DPC}) to bit rate without DPC (R) increases for longer fibre links, and it reaches 1.65 at 6000 km. In Figure 4.15, the ratio R_{DPC}/R is shown for optical fibre links with lengths 4000 km and 6000 km. As the bandwidth grows, R_{DPC}/R increases and tends to 2 at large bandwidth (1.98 for 4000 km and 1.99 for 6000 km at 96 GHZ). Since dispersion is higher for longer fibre, R_{DPC}/R approaches faster to 2 for length 6000 km. Fig. 4.16 shows the simulation results for PDF of PAPR of input signal for a fibre link with length 4000 km and signal bandwidth 26 GHz with and without DPC. The values of PAPR and its variance is significantly decreased with DPC. The average PAPRs are 14dB for the DPC method compared to 27dB without DPC.

Further reduction in noise variance of the nonlinear spectral domain is also expected if DPC method is used because the received temporal width and the required guard interval are decreased. Also, it is possible to introduce a complete pre-compensation by performing INFT on $\rho_0(\lambda)\exp(+4j\lambda^2 L/2L_D)$ at the transmitter side. It is expected that this method further reduces the noise in nonlinear spectral domain, but the required guard interval would remain equivalent to the case, in which no dispersion pre-compensation is used.

As a drawback of DPC, the numerical complexity of INFT increases. As the signal is pre-compensated the bandwidth increases due to the nonlinearity, and also the temporal width

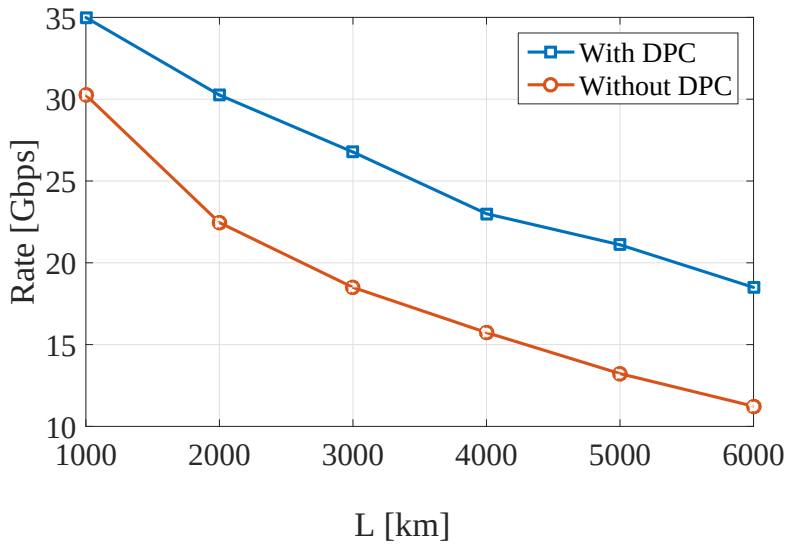

Figure 4.14: The bit rates for different fibre length at 26 GHz bandwidth

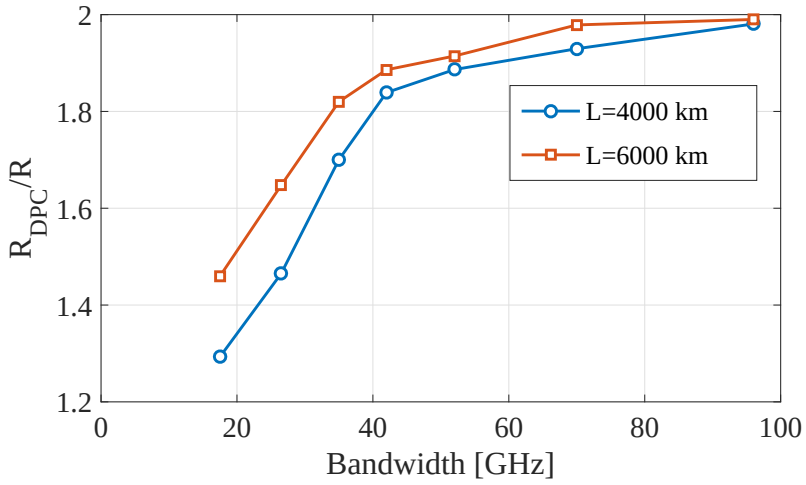

Figure 4.15: The ratio R_{DPC}/R for 4000 km and 6000 km fibre links

increases because of the dispersion. Therefore, higher complexity (i.e., larger number of calculation points and resolution in both domains) is required to maintain the same level of numerical error compared to the non-compensated system.

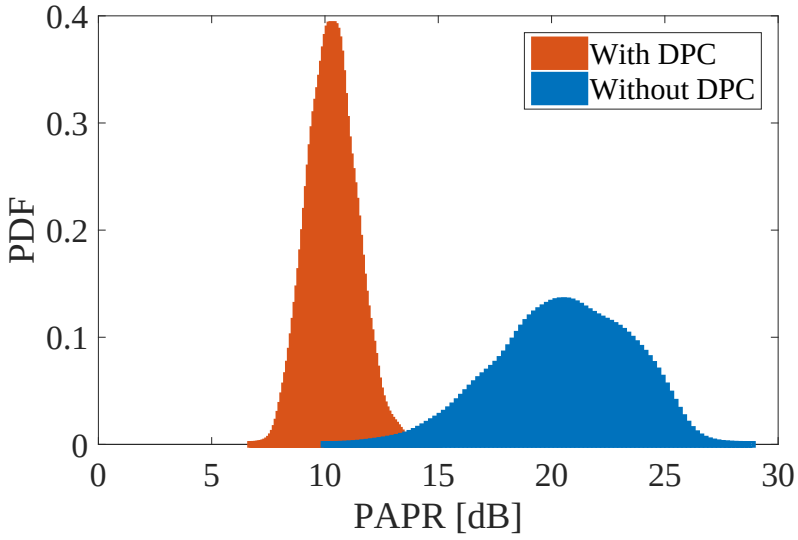

Figure 4.16: PDF of PAPR for fibre link of 4000 km and bandwidth 26 GHz

4.6 Summary

Efficient signalling on CS was studied in this section. First, the effect of chromatic dispersion on NFDM systems was studied. It was demonstrated that the signal bandwidth can be chosen so that the temporal signal broadening at the end of the fibre is minimized. By correctly selecting the bandwidth, not only the data rate is maximized, but also the noise variance is minimized in nonlinear spectral domain. Moreover, three different techniques were investigated for improving error performance compared to direct mapping on CS. For instance, our analysis showed that applying a linear filter on CS at the receiver significantly reduces the noise and improves the BER performance so that 9.6 Gbps can be transferred over 7100 km of fibre by only mapping the data on CS. The signal bandwidth was considered 26 GHz in our numerical results, however, data rates beyond values presented here may potentially be achieved by exploiting higher bandwidth and mapping data on DS as well. At the end a simple dispersion pre-compensation method was proposed for scenarios, for which using the optimum value of bandwidth is not possible, and it was demonstrated that data rate increase up to 100% is possible.

Chapter 5

Effect of polarization mode dispersion on the continuous spectrum

As stated earlier in chapter 2, a major assumption is needed in the definition of NFT based on NLSE, which is the absence of randomly varying birefringence or polarization mode dispersion (PMD). Nevertheless, this is usually not a practical assumption specifically in long-haul optical fibre systems, where fibres are subject to unavoidable environmental stress (e.g., pressure on fibres laid on the sea bed). Although expensive polarization maintaining and PMD-free fibres can be manufactured, current installed fibres often have high PMD factors [98]. Therefore, it is crucial to investigate the effect of PMD for the newly proposed NFT-based systems. In this chapter, the optical fibre model including the PMD is reviewed, and the effect of PMD on the CS is studied analytically and by simulation for the first time. In a few recent related works polarization multiplexing for NFT-based systems was studied, for DS in [83, 85] and for CS in [84]. The feasibility of polarization multiplexing using CS was demonstrated in [84] using Manakov equation. Also, the effect of PMD was studied on such systems by simulation.

5.1 Fibre propagation model in the presence of PMD

Two orthogonally polarized modes (e.g., x and y) can travel through the single mode fibre at the same time. These modes are degenerate in the sense that their refractive index are identical as long as the fibre is perfectly cylindrical and free from environmental stress. In real conditions, fibre is subject to random effects which violate the ideal condition of perfect symmetry. This causes random variation of the propagation constants (or refractive indexes) as well as the orientation of two orthogonally polarized modes along the fibre. Consequently, the fields in

the two polarization states would randomly interact as the light propagates down the fibre. The random birefringence results in pulse broadening which is referred to as PMD. In addition, the random change of polarization axes, which may not be a major concern in direct detection, becomes an issue in coherent communication systems such as NFT-based structures.

Assuming that the nonlinear effects are not large enough to stimulate the intensity dependant birefringence (nonlinear birefringence), the coupled nonlinear Schrödinger equation for constant linear birefringence are expressed as [102, 144]

$$\frac{\partial U}{\partial l} = -\Delta\beta_1 \frac{\partial U}{\partial \tau} - j\frac{1}{2}\beta_2 \frac{\partial^2 U}{\partial \tau^2} + j\gamma\left(|U|^2 + \frac{2}{3}|V|^2\right)U \tag{5.1a}$$

$$\frac{\partial V}{\partial l} = +\Delta\beta_1 \frac{\partial V}{\partial \tau} - j\frac{1}{2}\beta_2 \frac{\partial^2 V}{\partial \tau^2} + j\gamma\left(|V|^2 + \frac{2}{3}|U|^2\right)V \tag{5.1b}$$

where $U \equiv U(\tau, l)$ and $V \equiv V(\tau, l)$ are the slowly varying complex envelope of optical fields in the two orthogonal polarization directions. The coupled nonlinear Shcrödinger equations (CNLSE) (5.1) are derived for the practical physical case of small beat length compared to the other length scales (i.e., nonlinearity, chromatic dispersion, and polarization induced differential group delay), for which the effect of rapid variations due to the birefringent beating is cancelled out by averaging over the rapidly varying term (containing $\exp(\pm\Delta\beta_0 l)$) [102]. This condition is almost always satisfied for practical scenarios of optical fibre communication. In (5.1), $2\Delta\beta_1$ is the inverse group velocity difference between two polarizations and is randomly varying along the fibre.

Propagation of signal along the fibre accounting for random birefringence and PMD can be modelled by considering (5.1) for random $\Delta\beta_1$. In order to include random alteration of polarization directions, the fibre is split into segments of correlation length l_c (the length over which two polarization components remain correlated), and at each segment the fields are rotated randomly by a unitary complex rotation matrix as

$$\begin{pmatrix} U(\tau, l+l_c) \\ V(\tau, l+l_c) \end{pmatrix} = \begin{pmatrix} \cos(\theta) & \sin(\theta)e^{j\phi} \\ -\sin(\theta)e^{-j\phi} & \cos(\theta) \end{pmatrix} \begin{pmatrix} U(\tau, l) \\ V(\tau, l) \end{pmatrix} \tag{5.2}$$

where $-\pi \leq \theta \leq \pi$ and $-\pi/2 \leq \phi \leq \pi/2$ are uniform random variables. Therefore, if the initial signal is polarized in one of the orthogonal polarization states, about half of the energy

is coupled to the other polarization state at the end of a sufficiently long fibre link. Note that the split-step Fourier method can be easily modified for numerical evaluation of CNLSE (5.1). It is only needed to include the term proportional to $\Delta\beta_1$ in the dispersion operator (see section 2.3.1) and include the rotation (5.2) at the proper length steps.

5.2 Effect of PMD on CS

The NFT is defined based on single-polarization transmission without PMD, and this is an inherent assumption in all the research on the NFT-based systems. Here, we intend to study the PMD effects on such NFT-based system, specifically the CS[1]. Based on (5.1), even if the signal is transmitted only in one of the orthogonal polarizations, almost half of the energy is coupled to the other polarization mode at the receiver. Therefore, some kind of compensation is essential which reverses this random process. For linear scenarios, several techniques are proposed which require finding the principal polarization states and compensating the delay between two polarization modes [145, 146]. However, there is no straightforward method for compensating the polarization effects in the presence of nonlinearity [102]. Thus, we use the ideal linear all-order PMD compensation method here. It should be mentioned that we expect such a linear PMD compensation method to work reasonably well for the CS because, in the absence of soliton component, the large dispersion would push the system to near linear regime after propagating over an initial distance over the fibre.

5.2.1 Linear all-order PMD compensation

In linear case, the effect of PMD in the fibre is modelled as a concatenation of randomly oriented birefringent segments, which can be represented by frequency dependent Jones matrices as [145]

$$\mathbf{A}(\omega) = \prod_{k=1}^{K} \mathbf{A}_k(\omega), \tag{5.3}$$

[1]Note that it is possible to redefine NFT (in vector form) for the polarization multiplexed system using the Manakov equation [37, 83, 84], but even in that case the random perturbation effect of PMD should to be studied separately.

where

$$\mathbf{A}_k(\omega) = \begin{pmatrix} e^{i\omega\Delta\beta_{1k}l_c} & 0 \\ 0 & e^{-i\omega\Delta\beta_{1k}l_c} \end{pmatrix} \begin{pmatrix} \cos(\theta_k) & \sin(\theta_k)e^{j\phi_k} \\ -\sin(\theta_k)e^{-j\phi_k} & \cos(\theta_k). \end{pmatrix} \tag{5.4}$$

Obviously, in the absence of nonlinearity ($\gamma = 0$ in (5.1)), multiplication of $\mathbf{A}^{-1}(\omega)$ in the fields at the receiver would recover the signal as if no PMD exists [145]. This is called all-order PMD compensation and requires channel state information or, in other words, the matrix $\mathbf{A}(\omega)$ at every frequency. However, when the nonlinearity is not negligible, part of the energy would remain in the other orthogonal polarization state since the linear PMD compensation, even the all-order method, would not be totally effective.

As stated earlier, to the best of our knowledge, a PMD compensation method for coherent nonlinear fibre channel is not available yet. Thus, we use all-order linear PMD compensation method for the NFT-based system in Figure 3.1. A dual polarization coherent optical receiver is needed as shown in Fig. 5.1. Then, PMD compensation is performed digitally, shown by the polarization mode dispersion compensation (PMDC) block in Figure 5.1, as

$$\begin{pmatrix} \hat{U}_L(\omega) \\ \hat{V}_L(\omega) \end{pmatrix} = \mathbf{A}^{-1}(\omega) \begin{pmatrix} U_L(\omega) \\ V_L(\omega) \end{pmatrix} \tag{5.5}$$

where $U_L(\omega)$ and $V_L(\omega)$ are the fields in frequency domain. It is assumed that the matrix $\mathbf{A}(\omega)$ is already available at the receiver by some estimation method, such as, estimation using a training sequence. Any kind of imperfect or distorted estimation (e.g., due to ASE noise) of channel matrix $\mathbf{A}(\omega)$ leads to another channel matrix $\tilde{\mathbf{A}}(\omega) = \mathbf{A}(\omega) + \Delta\mathbf{A}(\omega)$, where $\Delta\mathbf{A}(\omega)$ is the estimation error. Therefore, and additional source of performance degradation will be added to the system by imperfect channel estimation. In this chapter, we assume that the channel estimation is error-free. Assuming that input optical signal is linearly polarized in the x direction, the output of PMDC block $q_L(t)$ is chosen as $\mathrm{IFFT}[\hat{U}_L(\omega)]$ (after proper normalization according to (2.9)). The rest of the system is identical to conventional structure in Figure 3.1. Our purpose is to study the effect of PMD after such compensation.

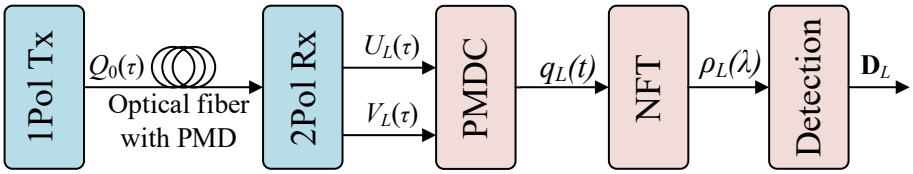

Figure 5.1: Block Diagram of a NFT-based system with PMD compensation.

We use the relation $D_P = 2\Delta\beta_1\sqrt{8l_c/3\pi}$ to determine average value of $\Delta\beta_1$ [144]. For demonstration purpose, the outputs of blocks in Figure 5.1 are shown in Figure 5.2, for a simple simulation with PMD parameter $D_P = 0.4\ \mathrm{ps}/\sqrt{\mathrm{km}}$ for a 16QAM modulated CS signal over the length of $L = 2000$ km of fibre. In this chapter, $T_0 = 0.25$ ns is chosen, and signal bandwidth is 52 GHz.

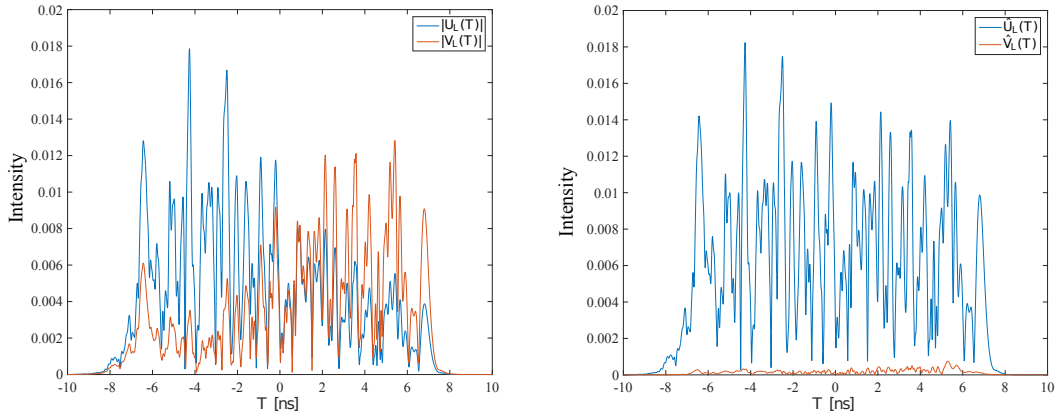

Figure 5.2: (a) Received signals in two polarization before PMDC. (b) Signals in two polarizations after PMDC.

During the propagation of signal along the fibre, the birefringence causes the signal energy to transfer to the other polarization state. Almost half of the signal energy would be coupled into the non-original polarization state. Thus, before any PMD compensation, each of the received two polarization components consist almost equal energies. Then, by applying the linear all-order PMD compensation, most of the signal energy is recovered at the original polarization state, and only a small portion of energy remains in the other polarization state as a result of nonlinearity. However, the recovered CS is slightly distorted which may affect the performance of the system. In the following subsections, the distortion caused by nonlinearity

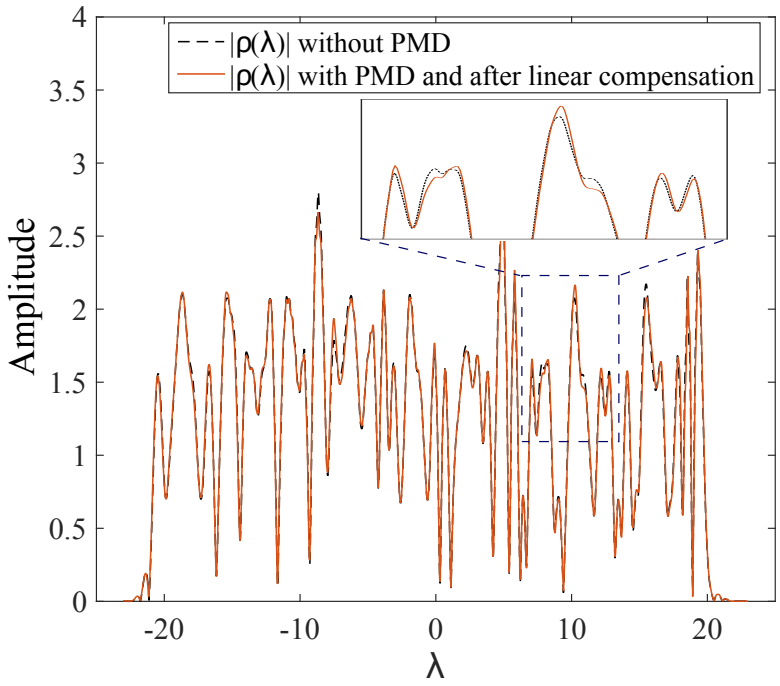

Figure 5.3: Continuous spectrum after PMDC in comparison to PMD-free case.

after the PMDC is investigated on different types of modulation formats.

5.2.2 Single-level modulation

Without nonlinearity the all-order linear PMD compensation perfectly reverses the effects of PMD. However, when the nonlinearity is not negligible some effects of the PMD remain uncompensated. Therefore, it can be assumed that the scaler channel mode, defined by NLSE, is valid but is perturbed by the uncompensated effects of PMD as a consequence of nonlinearity. As a result, we consider a modified NLSE given by

$$jq_z(t,z) = q_{tt}(t,z) + 2|q(t,z)|^2 q(t,z) + n(t,z) + h(t,z), \tag{5.6}$$

where $h(t,z)$ is the small perturbation term as a result of interactions of nonlinearity and PMD. Our simulation results, which will be presented later in this section, show that the impact of PMD depends on the link parameters and signal itself. Apart from the fibre specifications (such as PMD parameter D_p), the perturbation term depends on the fibre length as well as signal amplitude at symbol points $|\rho_0(\lambda_k)|_{k=1}^K$ (i.e., the sequence of amplitudes of input symbols),

and thus we assume $h(t,z)$ follows the model

$$h(t,z) = G(z, |\rho_0(\lambda_k)|_{k=1}^K)q(t,z) + e(t,z). \tag{5.7}$$

Here, the real deterministic function $G(z, |\rho_0(\lambda_k)|_{k=1}^K)$ represents the dependence of perturbation to the fibre length and input symbols at λ_k[1] (input energy). Also, signal-independent term $e(t,z)$ shows the noise-like error after linear all-order PMD compensation, due to the random nonlinearity and PMD, which has an effect similar to the ASE noise. Such a model for PMD effects is based on our observations, and it will be demonstrated later in this chapter that this model agrees with the simulation results.

First, the effect of first part of the perturbation term in (5.7) (i.e., $G(z, |\rho_0(\lambda_k)|_{k=1}^K)q(t,z)$) is investigated, and then the effect of error $e(t,z)$ is added. In single level modulation formats (i.e., all symbols have the same amplitude, such as QPSK), $G(z, |\rho_0(\lambda_k)|_{k=1}^K)$ can be represented by a function which only depends on the fibre length $P_E(z)$ for a fixed signal energy E. It is expected that even in single-level modulation the effect of PMD would be more significant for larger energies. Therefore, the perturbed NLSE (without ASE noise $n(t,z)$ and error $e(t,z)$) is expressed as

$$j\frac{\partial q(t,z)}{\partial z} = \frac{\partial^2 q(t,z)}{\partial z^2} + 2[|q(t,z)|^2 + \frac{1}{2}P_E(z)]q(t,z). \tag{5.8}$$

In [147], it was demonstrated that for inhomogeneous media (e.g., propagation of electromagnetic waves in an inhomogeneous plasma) the NLSE is also defined in the same form as in (5.8). It was shown that for the real function $P_E(z)$ that the inverse scattering method holds without major modifications. After some simple manipulation of Zakharov-Shabat eigenvalue problem and the corresponding evolution problem, the evolution of CS can be derived as [100, 147]

$$\rho_L(\lambda_k) = \rho_0(\lambda_k)e^{-4i\lambda_k^2 z + \psi_P(z)},$$

[1] In this chapter, $\lambda_k \in \mathbb{R}$ is the nonlinear frequency at symbol points and should not be mistaken with eigenvalues $\lambda_m \in \mathbb{C}^+$

where

$$\psi_P(z) = -i \int_0^z P_E(\zeta) \mathrm{d}\zeta.$$

Therefore, for the small perturbation term $h(t, z)$, the effect of first part of the perturbation term in (5.7) can be modelled as an additional phase shift of the CS. Consequently, when noise $n(t, z)$ and error $e(t, z)$ are included, the channel model for the CS signal after linear dispersion compensation according to (2.26) is expressed as

$$\tilde{\rho}_L(\lambda_k) = \rho_0(\lambda_k) e^{\psi_P(z)} + \eta'_L(\lambda_k)$$

where $\eta'_L(\lambda)$ describes the combined effect of noise and error in the nonlinear spectral domain which is signal dependent as discussed in chapter 3.

Thus, the effect of PMD on CS in single level modulation format can be described as an energy and distance dependent phase shift and a contribution to the additive signal dependent noise in CS. In order to validate this model, a simple simulation is performed here in noise-free case ($n(t, z) = 0$). Channel parameters are the same as before ($D_P = 0.4\ \mathrm{ps}/\sqrt{\mathrm{km}}$ and $L = 2000$). The received symbols are demonstrated in Figure 5.4 for two different launch powers. It is observed that the constellation diagram is rotated as a result of the phase shift ψ_P, and the symbols are received with random errors caused by $e(z, t)$. Moreover, it can be seen that both the value of phase shift and noise cloud are larger for higher launch power. The direct dependence of $P_E(z)$ to the signal power or energy is confirmed by such an observation.

In this chapter, we evaluate the performance degradation, as a results of ASE noise or PMD, by error vector magnitude (EVM) which is defined as

$$\mathrm{EVM} = \frac{\sqrt{\frac{1}{I} \sum_{i=1}^{I} |D_L^i - D_0^i|^2}}{|D_0^{\max}|} \tag{5.9}$$

for total number of simulation samples I. Here, D_0^i and D_L^i respectively represent the ith transmitted and received symbols. In (5.9), $|D_0^{\max}|$ is the maximum symbol amplitude in the constellation. Table 5.1 shows the average EVM and average rotation angle of the constellation diagram. It is observed that both quantities increase for larger values of power and fibre length. Therefore, both effects of PMD on CS and their dependence to the power and fibre length are

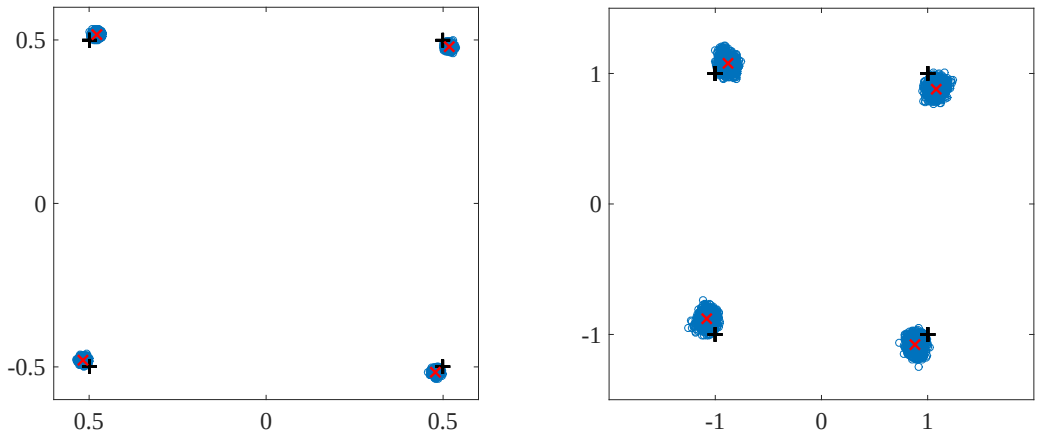

Figure 5.4: Detected symbols after PMDC and NFT operation for QPSK modulation at launch powers (a) -9 dBm and (b) -6 dBm. Blue circle are the detected symbols, black pluses are the original symbols, and red crosses are mean values of detected symbols.

confirmed for single level modulation.

Table 5.1: The average EVM and average rotation angle of the constellation ψ_P for QPSK modulation format with launch powers -9 and -6 dBm for $D_P = 0.4$ ps/$\sqrt{\text{km}}$.

	$L = 1000$ [km]		$L = 2000$ [km]	
P [dBm]	ψ_P [Rad]	EVM [%]	ψ_P [Rad]	EVM [%]
-9	0.0306	3.18	0.0387	3.99
-6	0.0812	8.55	0.1026	10.77

5.2.3 Multi-level modulation

In the perturbation model presented for single level modulation, the term $G(z, |\rho_0(\lambda_k)|_{k=1}^K)$ was expressed by $P_E(z)$ because the symbol amplitude were identical. It was confirmed by simulation that such model can describe effects of PMD on the CS at least in the range of interest. However, in multi-level modulation (i.e., symbols have different amplitudes, such as 16 QAM), such assumption is no longer valid, and consequently, the general form $G(z, |\rho_0(\lambda_k)|_{k=1}^K)$ should replace $P_E(z)$ in (5.8). Thus, the analysis in [147], is not straightforward any more, and major modifications are required for application of inverse scattering method. Since such problem is cumbersome and the purpose of this chapter is to only provide an understanding of the effect of PMD, the simulation results are presented here

for a 16QAM modulation format. Figure 5.5 shows the received symbols after 2000 km of fibre length with PMD parameter $D_P = 0.4\ \mathrm{ps}/\sqrt{\mathrm{km}}$. It is observed that similar to the QPSK format, the effect of PMD depends on the launch power. Also, it can be seen that the rotation angle of the constellation diagram and noise cloud size depend on the symbol amplitude as well as launch power.

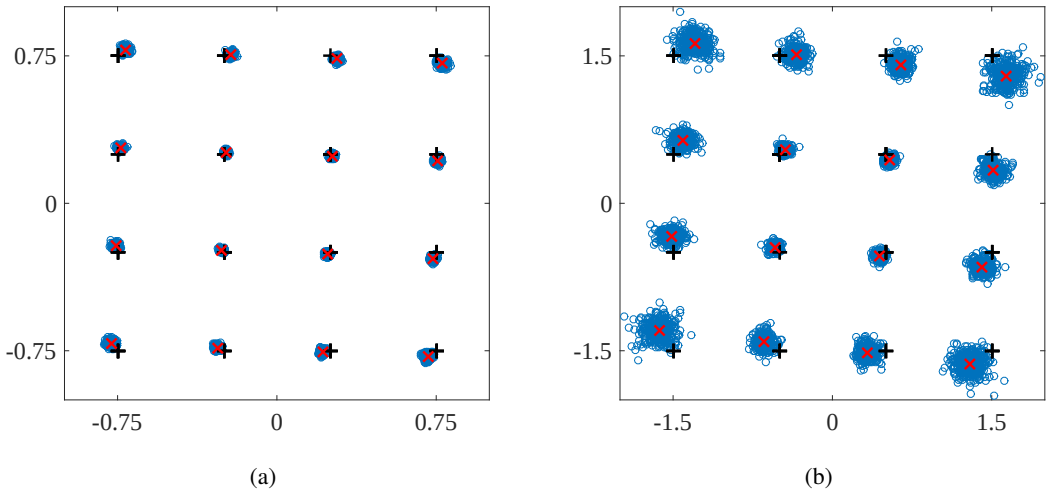

Figure 5.5: Detected symbols after PMDC and NFT operation for 16QAM modulation at launch powers (a) -9 dBm and (b) -6 dBm. Blue circle are the detected symbols, black pluses are the original symbols, and red crosses are mean values of detected symbols.

For more detailed investigation, average EVM and average rotation angles of constellation are calculated for three different symbol amplitudes in 16QAM modulation format, shown by r_j, where $j = 1, 2, 3$ determines the ring associated for each amplitude. The definition of EVM for each ring is

$$\mathrm{EVM}^j = \frac{\sqrt{\frac{1}{I_j}\sum_{i=1}^{I_j} |D_L^{ij} - D_0^{ij}|^2}}{|D_0^{\max}|} \tag{5.10}$$

where I_j is the total number of the simulation samples for corresponding ring j. The results presented in Table 5.2, indicate that both quantities directly depend on the symbol amplitude as well as power and fibre length.

The observations in this section suggest that the effects of PMD in multi-level modulation format are similar to the single level modulation format with the exception that phase shifts are

Table 5.2: The average EVM and average rotation angle ψ_P for 16QAM modulation format with launch powers -9 and -6 dBm for $D_P = 0.4\ \mathrm{ps}/\sqrt{\mathrm{km}}$ and $L = 2000$ km.

P [dBm]	ψ_P [Rad]			EVM [%]		
	r_1	r_2	r_3	r_1	r_2	r_3
-9	0.0424	0.0442	0.0466	1.55	3.41	4.8
-6	0.1004	0.1093	0.1178	3.61	8.5	12.45

dependent to the instantaneous CS signal amplitudes, and the channel model is given by

$$\tilde{\rho}_L(\lambda_k) = \rho_0(\lambda_k) e^{\psi_P(z,\rho_0(\lambda_k))} + \eta'(\lambda_k), \tag{5.11}$$

which shows that the phase shift $\psi_P(z, \rho_0(\lambda_k))$ is generally dependent to the fibre length and symbol amplitude. However note that, unlike the single level modulation format, this model for multi-level is not necessarily regarded as a solution of NLSE perturbed by PMD.

5.2.4 Detection in the presence of PMD

In previous subsections, it was demonstrated that, after the all-order linear PMD compensation, the CS signal is affected by a constellation rotation as well as a noise-like error as a result of PMD. The error part is combined with the ASE noise and will be investigated in the next section. The constellation rotation however can be estimated for a communication link before data transmission because it only depends on the constant PMD parameter associated to the particular link and transmission system. Therefore, the decision boundaries can be modified accordingly as schematically depicted in Figure 5.6 for QPSK modulation format. Note than only the treatment of the effect of phase rotation is studied in this section. For a single level modulation, the boundaries are rotated equal to the ψ_P estimated for the specific link parameters as shown in Figure 5.6. For the multi-level modulation, such as 16QAM, the boundaries should be determined based on the dependence of rotation angle to the symbol amplitude. Since the phase shift induced by PMD increase for higher symbol amplitudes, the decision boundaries deviate more from straight lines as the symbol amplitudes grow. Derivation of the modified decision boundaries for 16QAM modulation format requires complex calculations, as also discussed in [148] for the phase noise generated by nonlinearity. Therefore, either Maximum-Likelihood detection is applied at the receiver or pre-rotation of the constellation points at the transmitter is considered given the average rotation of each

constellation point is known.

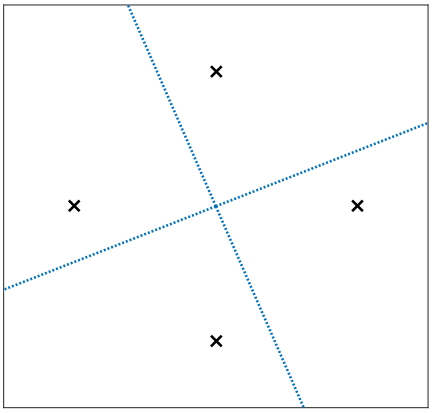

Figure 5.6: Decision boundaries for QPSK modulation formats in presence of PMD and after linear all-order compensation. (The figure are only for demonstration and are not based on actual data or simulation.)

Although the decision boundaries can be modified or Maximum-Likelihood detection can be employed at the receiver to compensate the effect of constellation rotation, a simpler way is to pre-compensate such effect by rotating the constellation at the transmitter backward with proper angles at each symbol amplitude. Since the rotation angle only depends on the specific link parameters (e.g., fibre length and PMD parameter), such approach can be applied assuming that the rotation angles are known at the transmitter for each symbol amplitude. Later, in the section 5.3.2, the combined effects of ASE noise and PMD are studied with assumption that required information is available and compensation is conducted at the transmitter.

5.3 Numerical analysis

In this section, the effect of PMD for different fibre lengths and PMD parameters are investigated. Also, system performance is studied when the signal is affected by both ASE noise and PMD.

5.3.1 Effect of PMD for different fiber lengths and PMD parameters

It was demonstrated in previous section that larger power leads to increased effect of PMD due to higher nonlinearity. Likewise, it is expected that PMD effects on the CS channel are more severe for longer fibre length or larger PMD parameter. We investigate this by simulation. The 16QAM modulation format and -6dBm launch power is chosen. Fibre length and PMD parameter are changed, and the resulted average rotation angle of the constellation diagram and EVM (average on all amplitudes) are measured. The results are demonstrated in Fugures 5.7 and 5.8, where it is confirmed that the average value for both EVM and ψ_P increases for longer fibre or larger D_P. Note that for simulations in this chapter a CS signal containing $K = 64$ randomly modulated symbols is transmitted through the fibre 100 times. In other words, 6400 samples are used for each measurement.

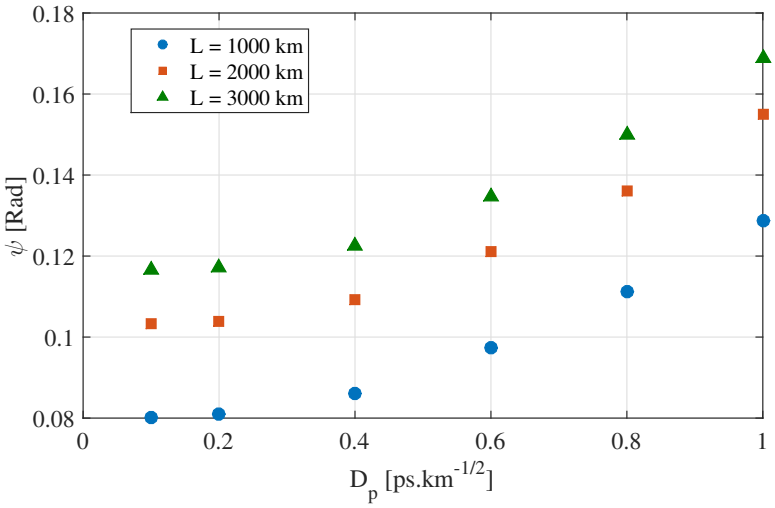

Figure 5.7: Average rotation angle for different fibre lengths and PMD parameters for 16QAM modulation and -6dBm launch power.

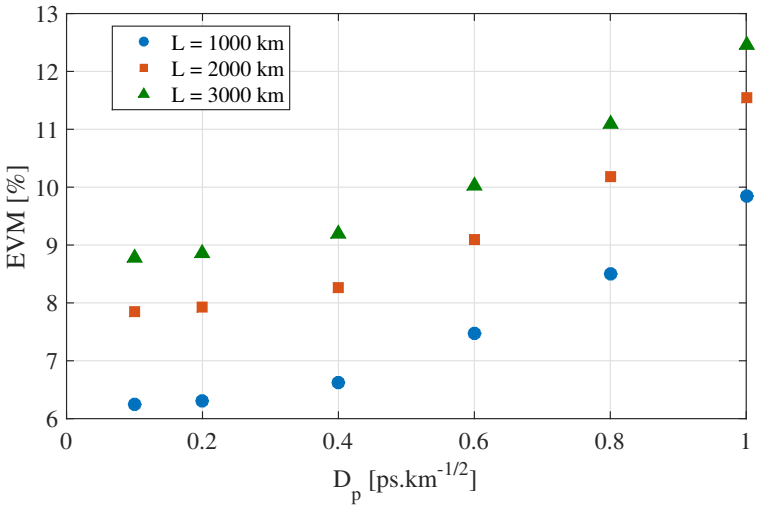

Figure 5.8: Average EVM for different fibre lengths and PMD parameters for 16QAM modulation and -6dBm launch power.

It is observed that EVM and ψ_P follow similar trends. It can be seen that the figures can be divided in two parts, for which PMD effect linearly increases with D_P. We call the scenarios with $D_P \leq 0.2$ ps/$\sqrt{\text{km}}$ the *low* PMD and otherwise *high* PMD. This threshold can be related to nonlinearity, which means that the effect of PMD is almost constant for low PMD case where effect of nonlinearity is minimal, and it increases linearly with D_P for high PMD case. The other interesting observation is that the difference between the 1000-km link and 2000-km link is larger than the difference between the 2000-km and 3000-km links. This effect can be explained by taking into account the effect of the chromatic dispersion. As the fibre length grows, the signal in time domain is dispersed more, and its amplitude is reduced. As a consequence, the impact of nonlinearity is smaller. In other words, it may be expected that the influence of PMD does not increase after an asymptotically long fibre length, in case of using the linear all-order PMD compensation.

5.3.2 Effect of PMD in the presence of ASE noise

The effect of PMD on the CS signal was studied in previous sections without including the ASE noise. The rotation of the constellation diagram can be compensated by pre-compensating at the transmitter because for a fixed link parameters the average rotation angle can be assumed to be known or estimated in a NFT-based optical fibre communication system. In this section,

we assume that such information is available, and the rotation of constellation diagram is compensated at the transmitter. We intend to study the combined effects of ASE noise and PMD by measuring the average EVM by simulation. Obviously, for multi-level modulation formats, the performance is degraded in case the average rotation angles are unknown and pre-compensation is impossible. Again, $D_P = 0.4\ \mathrm{ps}/\sqrt{\mathrm{km}}$ is considered as the PMD parameter of optical fibre. Apart from sampling the CS for detection, equivalent to direct signalling on CS in chapter 4, the performance with the linear filtering method introduced in chapter 4 is also presented, which is expected to improve the performance. The results are presented in Table 5.3.

Table 5.3: Average EVM after pre-compensation for different fibre lengths L [km] and launch power P_{in} [dBm].

		Sampling			Filtering		
P_{in}	L	PMD	ASE	ASE+PMD	PMD	ASE	ASE+PMD
	1000	0.83	9.97	10.22	0.81	4.21	4.31
-9	2000	0.95	17.3	17.54	0.92	6.09	6.14
	3000	1.01	24.77	25.36	0.98	8.82	9.04
	1000	2.73	11.41	11.85	2.53	4.37	5.09
-6	2000	3.14	20.96	21.97	2.93	6.46	7.19
	3000	3.33	31.96	33.43	3.08	10.86	11.63

It can be seen that the average EVM values for only PMD are much smaller than the values obtained for only ASE noise. However, PMD definitely affects the overall system performance because the EVM values including both PMD and noise are always larger than noise-only case. As expected, the average EVM increases for higher power or longer fibre. The linear filtering method has marginal effect on the PMD alone but significantly improves the performance in presence of ASE noise, with or without PMD. For the linear filtering method here, 18 samples per symbol are calculated by NFT. We infer that, while the effect of noise is generally dominant, the impact of PMD definitely should be taken into account particularly for long-haul optical fibre links. It can be seen in Table. 5.3 that the average EVM for the ASE+PMD case is smaller than the addition of average EVMs for cases when only one of the effects exists. This implies that there is a correlation between the error originated from PMD and ASE. Note that the values shown in Table 5.3 are obtained including the pre-compensation of constellation rotation. As an example, without such compensation and any other modified detection according to the PMD induced phase shift, average EVMs are equal to 23.02 and 9.86, respectively for direct

sampling and linear filtering, for $P_{in} = -6$ dBm and $L = 2000$ km for ASE+PMD case. This happens because the EVM in this case is calculated considering the original unrotated constellation points.

5.4 Summary

In this chapter, the effect of PMD, as an inevitable phenomena in long-haul optical fibre communication, on the CS channel was studied. Due to lack of effective PMD compensation method for nonlinear fibre link, the ideal linear PMD compensation method was exploited. It was demonstrated that, although the energy is returned to the original polarization using this method, the CS signal is affected by the interaction of nonlinearity and PMD which is not compensated by the all-order linear PMD compensation method. A perturbation model was used for single and multi-level modulation formats to understand the impact of PMD after the proposed compensation. A constellation rotation as well as noise-like error was observed for the CS channel. The results were confirmed by simulation, and different scenarios were examined in terms of average rotation angle and EVM. It was also shown that the effect of noise is dominant even in presence of PMD, but, for long-haul systems, evaluation the PMD surely should be considered since it degrades the performance and require extra signal processing.

Chapter 6

Achievable data rates for soliton communication

This chapter investigates the achievable data rates for nonlinear optical fibre channel with soliton amplitude modulation. First, the capacity in bits per symbol is numerically calculated using VNT and based on the signal dependent noise model for the imaginary part of eigenvalue (i.e., soliton amplitude) calculated by NFT. Physical constraints such as limited bandwidth, peak power, and temporal window, are also included in the analysis. By considering the dominant factor of timing error (i.e., the Gordon-Haus effect) a guard interval is defined, which allows us to calculate achievable rates in bits per second. At the end, a NFT-based system is studied in which data are mapped on CS as well as eigenvalues.

Bounds for the nonlinear optical fibre channel with only a single eigenvalue, which is equivalent to soliton communication, have been derived in [53, 57–60]. In these works, however, information rates in bits per second were not presented. Also, some intrinsic limitations, such as dependence of bandwidth on the amplitude, were ignored. In [54], spectral efficiency of coherent soliton communication was estimated by optimizing ratio of the pulse width to the bit slot. More recently, the performance of communication system using only a single eigenvalue was studied in [71]. A multi-level modulation format was used for modulating data on norming constant and optimization techniques were exploited which resulted in 6 bits/symbol rate at 24 Gbps over 1000 km. However, the capacity and achievable data rates for soliton amplitude communication is still unknown which is addressed in this chapter.

6.1 Soliton communication with amplitude modulation

For the DS, data can be mapped on the amplitude and phase of eigenvalues and norming constants. Here, we assume that the data is mapped only on the imaginary part of the single eigenvalue (i.e., soliton amplitude), which makes the system equivalent to the conventional soliton communication discussed in section 1. However, we look at this type of optical fibre communication from a NFT point of view. In other words, the estimation of capacity for soliton communication with amplitude modulation, which is still an open problem, is an step forward to find the capacity of nonlinear optical fibre through the NFT framework.

In order to estimate the achievable data rates, first, the noise variance predicted by perturbation theory [131] is validated by simulation. The VNT is then applied to transform the channel defined for soliton amplitudes into an AWGN channel. Capacity is estimated in bits per symbol taking into account physical limitations, such as bandwidth and peak power constraints. Finally, by considering the dominant factor of the timing error and determining an appropriate guard time, data rates in bits per second are estimated.

6.1.1 Channel Model

If only one eigenvalue exists at $z = 0$ and $\rho(\lambda, 0) = 0$, the solution of the NLS equation has an analytical form [100]

$$q(t,z) = 2\eta e^{-2i\zeta t + 4i(\zeta^2-\eta^2)z - i(\arg C_1 + \pi/2)} \operatorname{sech}(2\eta t - 8\eta\zeta z - 2\delta). \tag{6.1}$$

where $\lambda_1 = \zeta + i\eta$ is the only eigenvalue ($\eta > 0$). Also, we have $e^{2\delta} = \frac{C_1}{2\eta}$ where C_1 is the norming constant corresponding to the eigenvalue λ_1. For single soliton communication, we assume that discrete spectrum only consists one point $(M = 1)$ for each transmission, and the data symbol is mapped on the imaginary part of the eigenvalue $A = \Im\{\lambda_1\} > 0$ (soliton amplitude, or soliton energy). Assuming $\arg C_1 = -\pi/2$, $\delta = 0$ and $\zeta = 0$ the initial single soliton pulse is expressed as

$$q(t,0) = 2A \operatorname{sech}(2At). \tag{6.2}$$

The input signal $q(t,0)$ is launched into the fiber. After propagation along the fiber and addition of ASE noise, the NFT is applied on the received noisy signal to recover the received value of data symbol $\bar{A}$ which is the imaginary part of the eigenvalue calculated by NFT.

The conditional PDF $p_{\bar{A}|A}(\bar{a}|a)$ is non-Gaussian with signal-dependent variance [131]. Some works proposed distributions such as Chi-squared to describe the non-Gaussian noise [59, 60, 131]. However, as described in section 6.1.2, our analysis only requires the first and second moments of the noise description regardless of the exact PDF. Based on the first order perturbation theory [53, 57, 58], first two conditional moments of the received symbol $\bar{A}$ are approximated as

$$\mu_{\bar{A}}(A) = \mathsf{E}\{\bar{A}|A\} \simeq A, \tag{6.3}$$

$$\sigma^2_{\bar{A}}(A) = \mathsf{E}\{\left(\bar{A} - \mathsf{E}\{\bar{A}|A\}\right)^2 |A\} \simeq \sigma^2_N A, \tag{6.4}$$

where the accumulated noise power spectral density at the fibre length $l = L$ is (see (2.11))

$$\sigma^2_N = \frac{1}{2}\sigma^2 \frac{L}{2L_D} = \frac{\alpha h \nu_0 K_T \gamma L_D L}{2T_0}. \tag{6.5}$$

We conduct numerical simulations here to confirm the theoretical relationship between the moments given in (6.3)-(6.5). The split-step-Fourier method is used for simulating the propagation of perfectly separated single solitons over $L = 2000$ km of fibre with 200-meter steps and $T_0 = 0.1$ ns. Noise variance on the imaginary part of eigenvalue after NFT is shown in Figure 6.1 for different values of A. It can be seen that the relationship between the moments of the noise is well predicted by the perturbation theory.

The eigenvalues are calculated using NFT here. Unlike conventional soliton communication, in which direct detection is used, the NFT is a general tool that can be used to detect other degrees of freedom, such as norming constant, if they are used for data modulation. However, the soliton amplitude can be detected using other methods as well. The simplest way is sampling the received soliton at its time centre, yet this requires precise evaluation of time centre. Due to the timing jitter (Gordon-Haus effect [49]) additional signal processing is needed, and also filtering the noise out of signal's bandwidth is also essential. Nonetheless, soliton amplitudes can be detected efficiently by calculating the energy of received pulse since the energy of

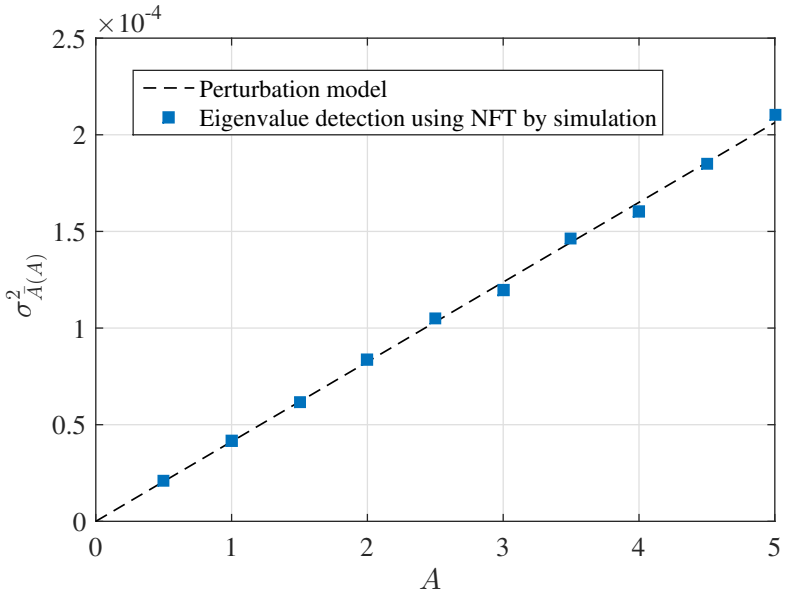

Figure 6.1: Noise variance on the imaginary part of eigenvalue.

soliton pulse is equal to 4A using (6.2). Energy detection results are almost the same as NFT, and simulated noise variance fits the perturbation theory perfectly similar to the NFT results in Figure 6.1. The histogram of detected soliton amplitudes are shown in Figure 6.2 using either NFT or energy detection. The signal-dependency of noise can be clearly observed in Figure 6.2, but the non-Gaussianity is not obvious, probably because of the moderate fibre length or soliton amplitude. However, the Kolmogorov-Smirnov test with significance level 5% is applied for the observed data (shown as histogram in 6.2), and the test decision is 1 for all the input amplitudes. The test decision 1 corresponds to the state that the test rejects the null hypothesis that the observed data comes from a Gaussian distribution. In other words, the distribution of the observed data is not Gaussian.

6.1.2 Capacity

In soliton communication, apart from an average energy constraint, a peak amplitude constraint should also be considered because the signal bandwidth is directly related to the soliton amplitude (see (6.1)). Moreover, in practical scenarios, peak power is also a constraint due to device limitations. On the other hand, there is a minimum amplitude constraint because the temporal width is inversely related to the soliton amplitude, and it tends to infinity when $A \to 0$.

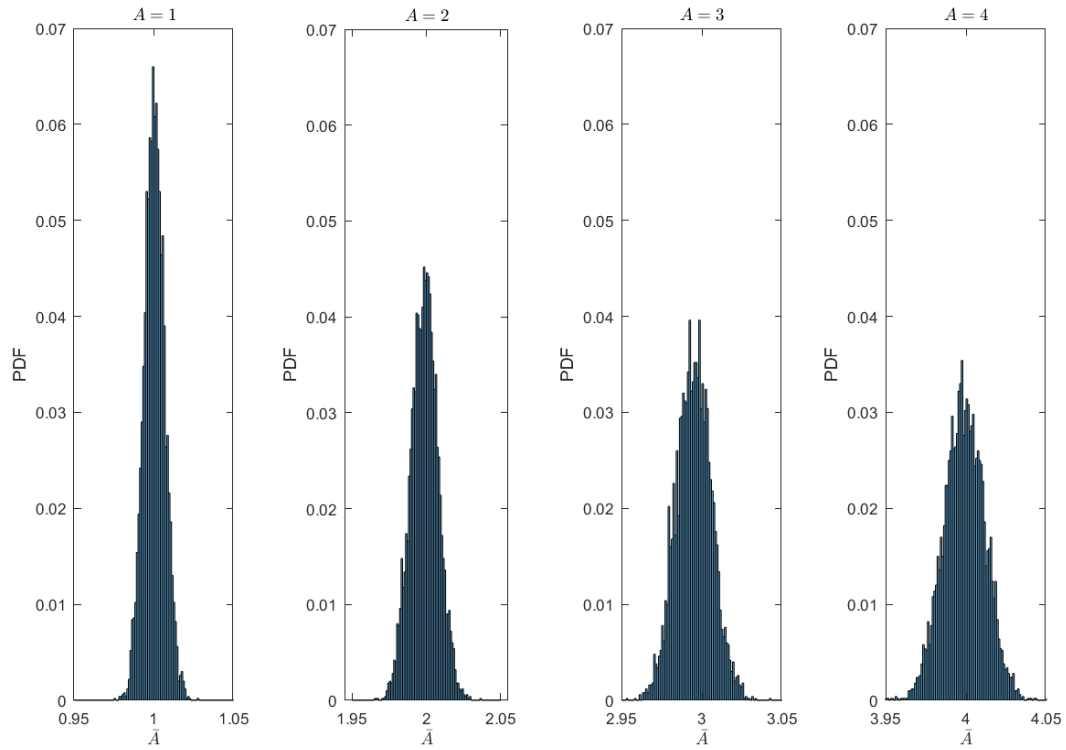

Figure 6.2: Histogram of received soliton amplitudes for transmitted amplitude $A = 1, 2, 3, 4$ from left to right, respectively.

The capacity problem for soliton communication with modulation on the soliton amplitude is defined as

$$C \triangleq \sup_{p_A(a):\mathsf{E}\{A\}\leq E_A/4,\ \mathrm{supp}\{A\}=[A_{\min},A_{\max}]} I(A;\bar{A}), \tag{6.6}$$

where $I(A;\bar{A})$, $A_{\min}$, and $A_{\max}$ are respectively the mutual information, minimum amplitude, and maximum amplitude. We also define the signal-to-noise ratio as $\rho = E_A/\sigma_N^2$ where E_A is the average input energy. Note that the energy of soliton pulse, as in (6.1), is equal to $4A$.

Following section 3.4, we use VNT [132] to make the capacity analysis more tractable. Recall that, the VNT $T(\cdot)$ should be applied on the random variable $\bar{A}$, with mean A and variance that can be written as a function of its mean as $\sigma^2_{\bar{A}}(A)$. The normalized random variable $Y = T(\bar{A})$ has then the statistics of $\sigma_Y^2 \simeq 1$ and $\mu_Y \simeq T(A)$ for sufficiently large values of A. Also, the PDF of Y tends to Gaussian as demonstrated for a family of non-Gaussian PDFs in [134] and for the continuous spectrum of nonlinear optical fibre in section 3.4. Based on (6.4), the VNT

is calculated as

$$T(u) = \int \frac{1}{\sqrt{\sigma_N^2 u}} \mathrm{d}u = \frac{2}{\sigma_N}\sqrt{u}, \tag{6.7}$$

which is similar to the Square-root transform previously used for the Poisson channel in [132, 135, 136].

The block diagram of channel using VNT is demonstrated in Figure 6.3, in which data is mapped on the variable $X = T(A)$. Consequently, the input soliton amplitude is $A = T^{-1}(X) = \sigma_N^2 X^2/4$. After propagation of the corresponding soliton pulse according to NLSE and recovering $\bar{A}$ using NFT, the VNT is applied to obtain the noisy version of the transmitted signal X as $Y = X + \Gamma$, where $\Gamma \sim \mathcal{N}(0,1)$, meaning that the equivalent channel between X and Y is an AWGN channel. In lemma 1 in section 3.4, it was proved that $I(X;Y) = I(A;\bar{A})$ for the system in Figure 6.3. Therefore, the optimization problem for the capacity in (6.6) can be expressed as

$$C = \sup_{p_X(x):\mathsf{E}\{X^2\}\leq\rho,\ \mathrm{supp}\{X\}=[X_{\min},X_{\max}]} I(X;Y). \tag{6.8}$$

where, $X_{\min} = T(A_{\min})$, and $X_{\max} = T(A_{\max})$.

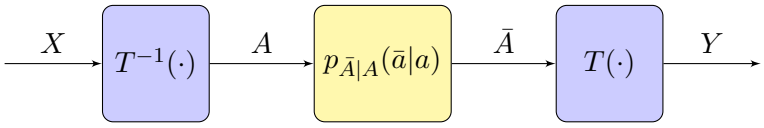

Figure 6.3: Block diagram of the system using VNT.

The problem (6.8) can be solved using the algorithm presented in [138] for the AWGN channel with peak and average power constraint, where it was proved that the capacity-achieving distribution is discrete with a finite number of mass points. The obtained capacity for different values of $X_{\max}$ and $X_{\min} = 0$ is shown in Figure 6.4. As expected, higher capacities are achieved for larger $X_{\max}$. It should be noted that for a fixed $\Delta X = X_{\max} - X_{\min}$ the capacity saturates to a fixed value at high average power, but the power in which the saturation occurs differs for different values of $X_{\min}$. The best lower bound recently derived in [59, Fig. 5] is also included in Figure 6.4. About 4 dB gain in signal-to-noise ratio is observed for almost all values of capacity compared to the Half-Gaussian distribution considered in [59]. Also, the capacity achieving input distribution is shown in Figures 6.5 and 6.6 for $X_{max} = 20$, which tends to uniform distribution for large values of ρ.

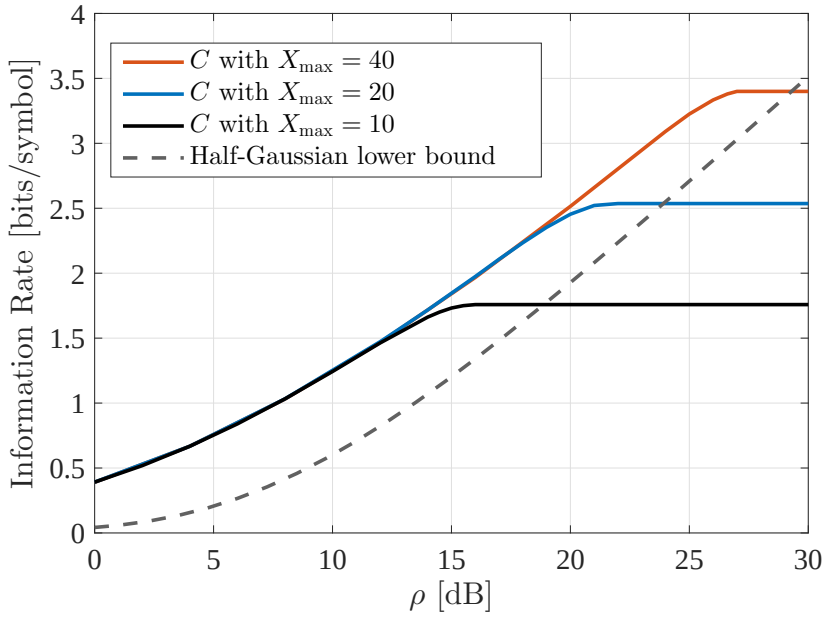

Figure 6.4: Capacity using VNT transform for $X_{\min} = 0$.

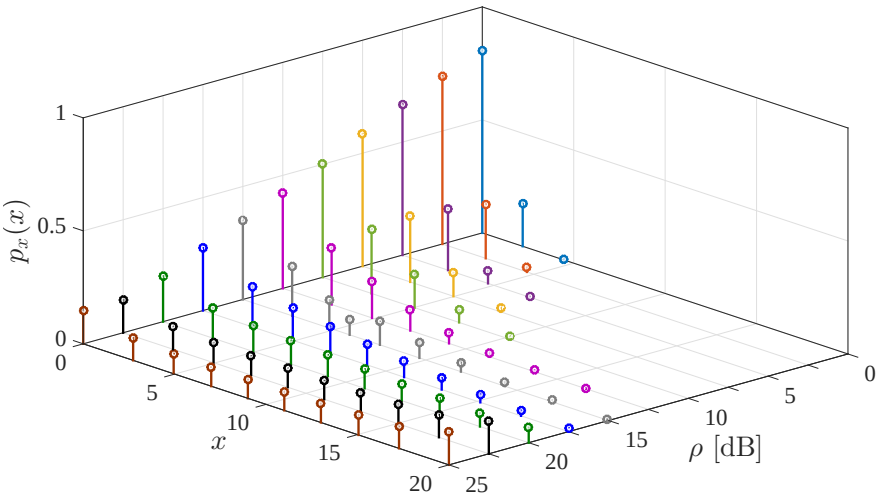

Figure 6.5: Capacity achieving distributions for fixed $X_{max} = 20$.

The average power can not be larger than the peak power determined by the peak amplitude constraint. Therefore, for sufficiently large average power constraint, where the capacity is limited by peak power instead of average power, we have

$$C \leq C_{PP} = \sup_{p_X(x):\ \mathrm{supp}\{X\}=[X_{\min},X_{\max}]} I(X;Y) \quad . \tag{6.9}$$

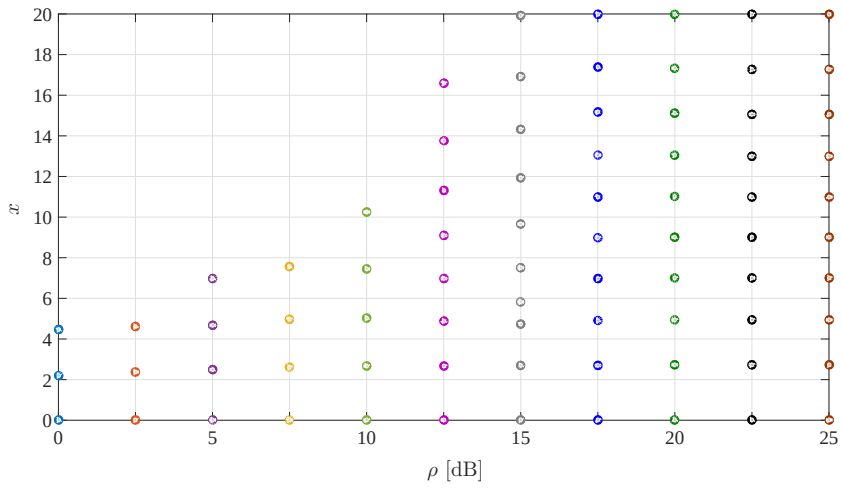

Figure 6.6: Capacity achieving distributions for fixed $X_{max} = 20$.

As it is observed in Figure 6.5, the capacity-achieving input distribution tends to uniform distribution for large values of ρ relative to ΔX, and thus the capacity C_{PP} can be estimated by the information rate for a uniformly distributed input [138].

$$C_A = \log \frac{\Delta X}{\sqrt{2\pi e}}. \tag{6.10}$$

The solution of problem (6.8) for large values of ρ, where average power constraint is inactive (C_{PP} which is equivalent to C at saturation point in Figure 6.4), is shown in Figure 6.7 as well as C_A for different values of ΔX. It can be seen that, while being a lower bound, C_A tends to C_{PP} for large values of ΔX.

6.1.3 Achievable Rates

The statistical model in (6.3)-(6.5) is derived based on the assumption that there is no soliton interactions due to timing error. Therefore, the temporal window should be defined based on the shift of the time center of soliton pulse due to noise, so that such interactions are avoided. The temporal width of the original input pulse is equal to $3/A$, calculated for the interval consisting 99.5% of the energy of soliton pulse (6.1). The temporal window required for input A is then defined as

$$T_w(A) = 3/A + 2T_g(A), \tag{6.11}$$

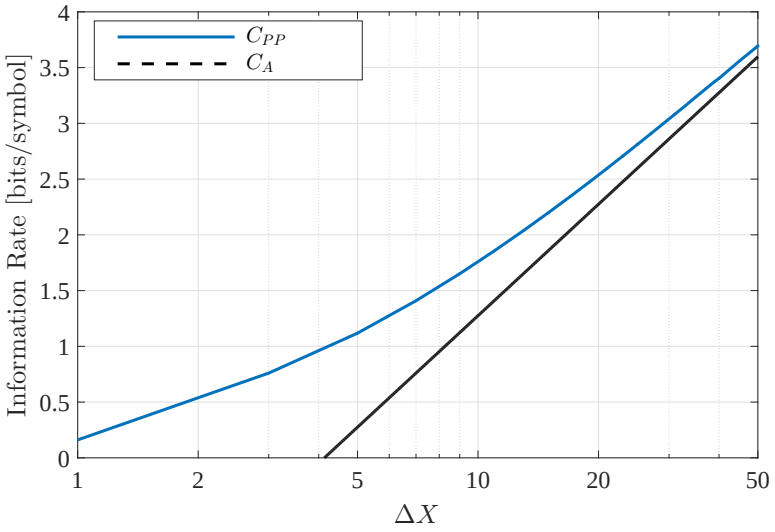

Figure 6.7: Capacity for large average power and different ΔX.

where $2T_g(A)$ is the required guard time. By properly defining $T_g(A)$, it can be assumed that neighboring soliton pulses will not interact with each other.

We define such guard time by taking into account the dominant factor of timing error (i.e., Gordon-Haus effect [49]). Centre of time for a soliton pulse is derived as $T_c(A, L) = \frac{1}{2A} \ln \frac{|C_1(\lambda_1, L)|}{2A}$ [36]. The dominant factor of the noise on the logarithm of the amplitude of norming constant $\ln |C_1(\lambda_1, L)|$ is modelled as a Gaussian process $\mathcal{N}(0, 4\sigma^2 L^3 A^3 / 9L_D^3)$, obtained via perturbation theory [49, 57]. Therefore, for the centre of soliton pulse, we have

$$\mathsf{E}\{T_c(A, L)^2\} = \frac{2\alpha h \nu_0 K_T \gamma}{9 L_D T_0} L^3 A. \tag{6.12}$$

Assuming that the noise on the norming constant $C_1(\lambda_1, L)$ is Gaussian [49, 53, 57], the guard time $T_g(A)$ is defined as $\Pr\{T_c(A, L) > T_g\} < \epsilon$ for amplitude A, where the parameter ϵ determines the probability that the soliton pulse moves beyond the defined guard time. Thus, we have

$$T_g(A) \geq \sqrt{\frac{4\alpha h \nu_0 K_T \gamma}{9 L_D T_0} L^3 A}\, \mathrm{erfc}^{-1}(2\epsilon). \tag{6.13}$$

Considering (6.13), the soliton width $3/A$ is smaller than or equal to $2T_q(A)$ for

$$A \geq \sqrt[3]{\frac{81 L_D T_0}{16\alpha h \nu_0 K_T \gamma L^3 \operatorname{erfc}^{-1}(2\epsilon)}}, \tag{6.14}$$

which indicates that $2T_g(A) \geq 3/A$ for $A \geq 0.015$ for long-haul fibre links $L \geq 1000$ km. Therefore, the soliton width is not the dominant factor in determining the temporal window, and the guard time (i.e., the timing jitter) limits the achievable data rate.

Assuming that A_{max} is given based on the available bandwidth of the channel, we first need to find the optimal A_{min} which maximizes the achievable data rate R. The choice of $A_{\min}$ along with given A_{max} determine both the capacity in bits per symbol and the temporal window. We define the achievable data rate as $R = C/T_w$, where $T_w = \mathsf{E}\{T_w(A)\}$ is the average temporal window calculated using (6.11) and (6.13) based on the capacity achieving distribution in (6.6). The maximum achievable data rates are obtained using Algorithm 1 considering enough large average power constraint, for which the capacity is derived from (6.9).

Algorithm 1 Find the maximum achievable rate

1: $R = 0$;
2: **for** $A_{\min} = 0^+$ to $A_{\max}$ **do**
3: Find C_{PP} for $\Delta X = T(A_{\max}) - T(A_{\min})$;
4: Calculate T_w for the input distribution found in step 3;
5: **if** $R < C/T_w$ **then**
6: $R = C/T_w$;
7: **end if**
8: **end for**

Figure 6.8 demonstrates the achievable rates as a function of fibre length for different available channel bandwidth obtained using Algorithm 1. In Figure 6.8, bandwidth (BW) is defined based on 99.5% of energy, which is equal to $1.214A$ for soliton pulse (6.1), and $\epsilon = 0.001$ is assumed. It can be seen that, as expected, higher bandwidth results in larger achievable data rates, and longer fibre length decreases the achievable data rates. For instance, 52.5 Gbps is achieved for 4000 km and 100 GHz. Note that these values are based on C_{PP} or, in other words, operation at saturation points in Figure 6.4, which do not require infinitely large powers.

Achievable data rates without timing jitter is also shown in Figure 6.8. A huge gap is observed for achievable rates with and without timing jitter particularly in long fibres. Two different

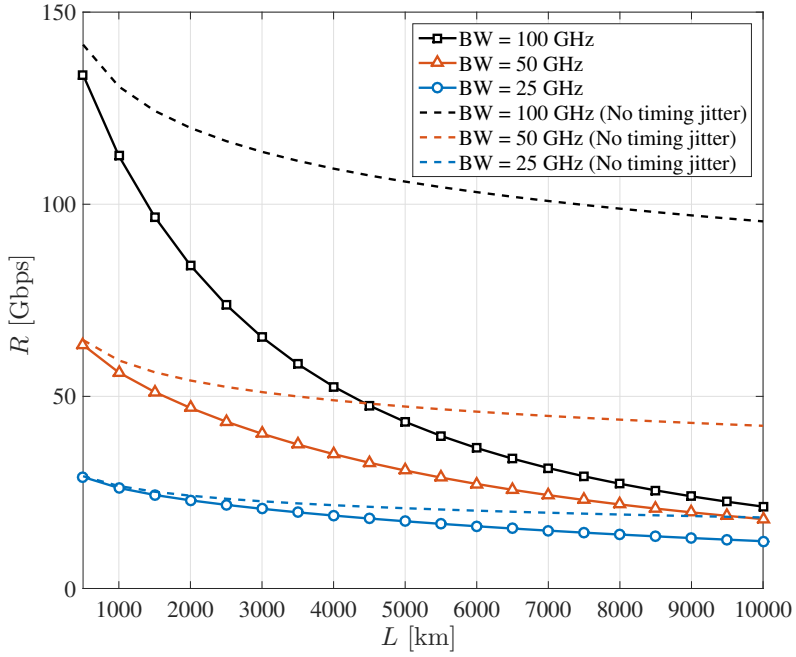

Figure 6.8: Achievable data rates for soliton communication with and without considering timing error.

points are deduced from this observation. One is that achievable data rates can potentially increase significantly if some efficient method is developed for suppressing the timing jitter. On the other hand, Figure 6.8 shows that without including the timing jitter (as in some of previous works) the estimated achievable data rates are far from practical implementation.

Note that the obtained data rates in this section are for the single soliton communication only. Finding the achievable rates for multi-eigenvalue communication as well as other signalling methods such as combined discrete and continuous spectrum modulation is left for future investigation.

6.2 Feasibility of communication system utilizing discrete and continuous spectra

In previous chapters, the CS channel was studied comprehensively, and in previous section the capacity of single soliton communication was estimated. Thus, it seems natural to examine the possibility of transmitting both CS and DS simultaneously. Here, we consider transmission of a 32 bit pseudo-random data stream which is first demultiplexed into continuous (30 bits) and

discrete (2 bits) spectral data streams. The continuous spectral data is modulated using pulse amplitude modulation (PAM) scheme with 8 levels (8PAM) over a sequence of 10 Gaussian pulses, and the discrete spectral data is modulated using OOK on two specific eigenvalues ($\lambda_1 = 1j$ and $\lambda_2 = 2j$). Eigenvalues are detected directly after the NFT block, while a matched-filter is utilized for data recovery for the continuous spectrum. Examples of time domain signal $q_L(t)$ are shown in Figures 6.9 and 6.10, respectively for CS signalling (i.e., no eigenvalue) and simultaneous signalling on CS and DS. The same random symbols for CS are chosen for both figures. It is observed that the amplitude of time domain signal increases due to the existence of solitons in Figure 6.10, and the signal power increases about 6 dBm compared to Figure 6.9. While the signal amplitude decreases when solitons are absent, it may periodically change during propagation because of the periodical behaviour of multi-soliton part of the signal. For instance, the peak amplitude is larger at 2000 km compared to 1000 km in Figure 6.10.

The detected symbols are observed in Figures 6.11 and 6.12. It can be seen that the eigenvalues are detected without error even in the presence of continuous spectrum. Figure 6.12 shows the 8-PAM levels and the received symbols. The probability of error tends to be higher for greater levels due to the signal-dependency of noise. Considering Gray coding, a bit error rate of 0.0027 was calculated. It is important to know that in this simulation the percentage of the

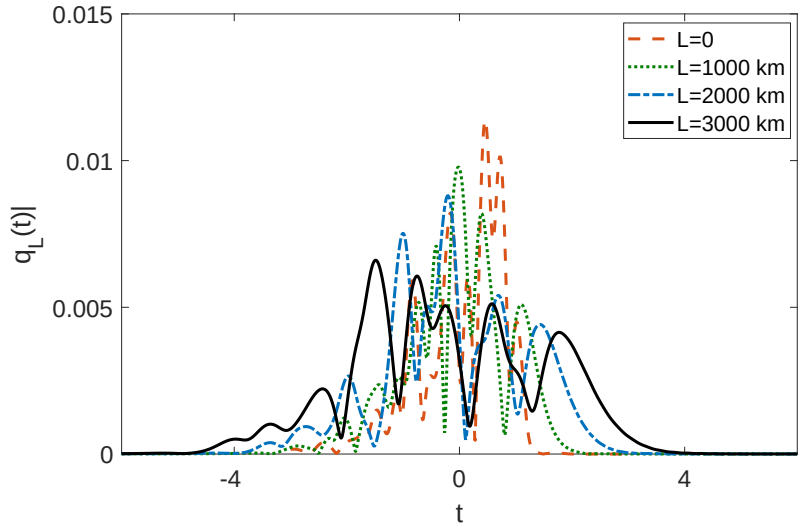

Figure 6.9: Normalized amplitude of time domain signal without solitonic part at different lengths. t is the normalized time.

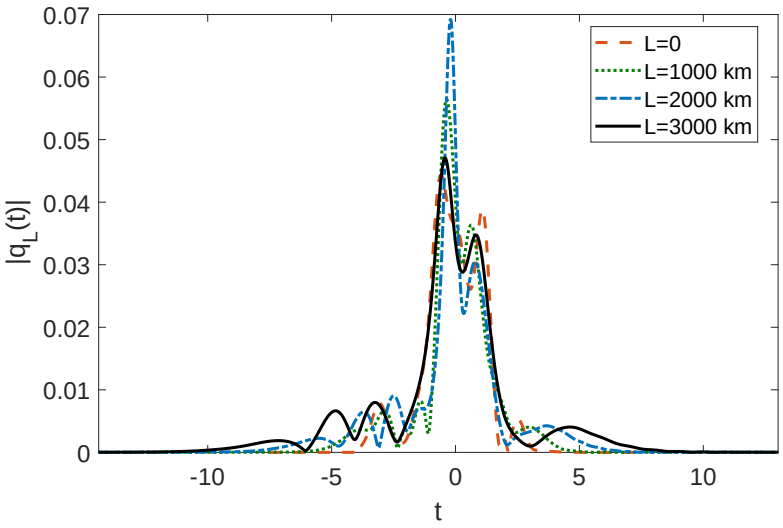

Figure 6.10: Normalized amplitude of time domain signal with eigenvalues $\lambda_1 = 1j$ and $\lambda_2 = 2j$ at different lengths. t is the normalized time.

numbers of errors for the levels 1, 1.25, 1.5, and 1.75 are 12 %, 14 %, 41 %, and 33 %, respectively, while no error has occurred for the first four levels. Notice that since there is just one error threshold for the last level, its percentage of error is not higher than the previous one.

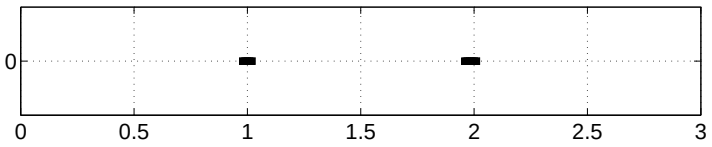

Figure 6.11: Detected eigenvalues at the receiver

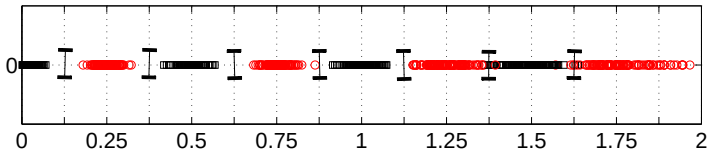

Figure 6.12: Received symbols from continuous spectrum

The presented results are only a demonstration of feasibility of combined signalling on CS and DS, and we do not intend to optimize the error rate or achieve high data rates. There are many factors that change the performance of an NFT-based system with simultaneous signalling on CS and DS. Similar to the single soliton in Section 6.1.1, the noise variance of the DS part

depends on the selection of eigenvalues in the system presented in this section [58, 61]. The signal dependency of noise in a multi-eigenvalue system is not derived yet, but it is known that the noise on all eigenvalues increases if higher values of imaginary part is selected. For instance, if $\{2j, 3j\}$ are selected instead of $\{1j, 2j\}$, the detected eigenvalue will be more noisy. The simulations here show that the CS is almost independent of the accompanied eigenvalues. However, the correlation between CS and DS was not studied. In [149], it was shown the CS and DS are uncorrelated when only purely imaginary eigenvalues are selected. On the other hand, in [150], a significant crosstalk between CS and DS was reported for a selection of eigenvalues with non-zero real parts. Therefore, a comprehensive study of crosstalk between CS and DS is required in future works. In this section, the INFT was performed using the same numerical method as before, explained in Section 2.3.3, including the eigenvalues. We observe that larger number or higher values of eigenvalues would lead to large numerical error. Such error occurs due to the exponential terms in the kernel of GLM equation (see (2.32)) that happen to be very large in some cases, while the other part of the GLM equation, associated with CS, usually has low values. Therefore, more efficient numerical method is required for simultaneous signal on CS and DS. In conclusion, based on the results presented in this chapter and previous chapters, it can be inferred that high data rates can potentially be achieved via efficient signalling on both spectra. As a simple alternative application, a few error-free eigenvalues can be transmitted as pilot sequence or error correction bits along with the CS signal that carries the data.

6.3 Summary

Achievable data rates for soliton communication with amplitude modulation were presented in this chapter. For evaluating the corresponding channel capacity, impaired with signal-dependent noise, VNT was used as a tool to make the analysis tractable. Similar problems also appear in other types of optical communication. Physical constraints such as peak power and maximum bandwidth were also included. The channel capacity was evaluated numerically, and also an asymptotic relation was given. It was demonstrated that high data rates can be achieved by considering an appropriate guard time. Since soliton communication exploits only a small portion of available degrees of freedom, it is expected that more advanced modulation schemes such as multi-eigenvalue communication or simultaneous signalling

on both CS and DS would result in even higher data rates. The first steps for the latter was demonstrated by a simple simulation of data transmission using CS along with a couple of purely imaginary eigenvalues.

Chapter 7

Conclusions and future works

In this thesis different aspects of NFT-based communication systems, as a promising approach for data rate enhancement in long-haul fibre links, were studied. Most of the contributions were focused on the continuous spectrum (CS) of the nonlinear optical fibre channel, and the discrete spectrum was investigated briefly at the end. The results of this thesis confirm huge potentials of nonlinear Fourier transform (NFT) for estimating the capacity of nonlinear optical fibre links and developing efficient signal processing methods for long-haul optical fibre communication. However, many questions remain unanswered which can be subject for future research projects. The detailed summary and conclusions of this thesis are presented hereafter, followed by potential future research directions.

7.1 Capacity of the CS channel

Using NFT, the communication channel for the nonlinear spectra (i.e., CS and DS) is effectively linear. Signalling on the CS is an attractive approach since the CS basically consists of a continuous complex waveform, and thus many known conventional communication techniques can be applied on it. However, specific statistics of noise on the CS channel make it impossible to simply use known methods. Therefore, as an initial step, the effective noise statistics on the CS channel were studied. The analysis was first performed using the asymptotic solution of NLSE for long fibre length. It was shown that the noise variance depends on the signal amplitude, and this dependence may be approximated by a polynomial with an order larger than 2. Also, it was predicted that the noise would generally be non-Gaussian on the CS channel. Simulation results for non-asymptotic scenarios confirmed these main features. In addition, it was observed that the noise on the real and imaginary parts of the the CS channel

were also dependent to each other. In other words, the nonlinearity of the optical fibre channel affects only the noise in nonlinear spectral domain, in such a way that the effective noise becomes non-Gaussian and signal dependent. Therefore, new approaches are needed for capacity analysis and signal processing.

The variance normalizing transform (VNT) can be used to transform a channel with signal dependent noise to an approximately additive Gaussian channel with constant noise variance. Such transformation using VNT does not change the channel capacity (proved in chapter 3), and thus can be used for capacity estimation of CS channel. Moreover, the signal dependency of noise with an order larger than 2 (approximately equal to 4 based on simulation), leads to limited signalling space after applying the VNT. Therefore, the capacity of CS channel can be derived by solving an optimization problem for mutual information with average and peak power constraint. This was performed numerically, and capacities were derived for different fibre lengths. For instance, about 6 bits/symbol is predicted for a fibre length of 2000 km when about 50 GHz bandwidth is available and data is mapped only on the CS. It should be noted that due to the signal dependency the capacity would be saturated for enough large powers. Finally, a closed form equation (3.22) was derived, including the bandwidth broadening and temporal dispersion, for the data rates in bits per second. It was shown that the data rate is directly related to the bandwidth and logarithmically to the maximum amplitude constraint determined by VNT, which itself depends on channel parameter such as fibre length. To summarize, noise statistics were studied and a method for capacity estimation was presented for the CS in chapter 3 which can be used for different scenarios of practical interest. The parameters considered in chapter 3 showed remarkable capacity for CS only. Therefore, high capacities for long nonlinear fibre links may be expected if all degrees of freedom (CS and DS) are exploited efficiently.

7.2 Signal processing techniques for the CS channel

Most of data transmission techniques using CS in the literature were based on conventional methods, and specific noise characteristics and the effect of chromatic dispersion played no role in development of such methods. In chapter 4, first, the effect of chromatic dispersion on the received temporal width of the signal was studied, and it was shown that the symbol

rate in nonlinear spectral domain or equivalently the bandwidth for a fixed number of data symbols can be determined to minimize the received temporal width. Such optimization would also lead to smaller noise variance in nonlinear spectral domain. Another simple method was also proposed regardless of the mentioned optimization, which can result in 100 % improved data rate by applying a simple pre-compensation. Since the temporal broadening as a result of chromatic dispersion significantly impacts the data rate, when data is mapped on CS only, the proposed methods can be hugely beneficial for future practical system designs.

Moreover, by considering the noise behaviour on the CS channel, different signalling techniques were proposed compared to the method of direct signalling on CS and sampling for detection. First, VNT was used for determining the sub-optimum 2-ring constellation diagram. In addition, a linear filtering method was also suggested which eliminates the impact of excessive noise added to the CS due to temporal broadening as a result of chromatic dispersion and INFT operation. At last, the GLM-based signalling was suggested, in which the data is mapped on the inverse Fourier transform of CS. Using GLM-based signalling, the instantaneous signal dependency of noise is avoided and the probability distribution is close to Gaussian. The latter two techniques are effective provided that enough samples of the received signal are available (increased computational complexity). These methods were compared regarding the BER and reach distance for different modulation formats. All methods demonstrated improved performance compared to the basic method of direct signalling on CS. For instance, using the linear filtering method a reach distance of 7000 km can be achieved at a 10 Gbps rate. The results of chapter 4 imply that the channel capacity and achievable data rates, when solely CS is used for data transmission, can be significantly improved by using an appropriate signal processing technique and channel parameter optimization.

7.3 Effect of PMD on the CS channel

The impact of PMD on the NFT-based system with signalling on CS was studied in chapter 5. Coupled nonlinear Shcroödinger equations were considered to model the PMD. It was observed that two orthogonal polarization components would be mixed due to the random birefringence. Since no effective PMD compensation method is available including the nonlinearity, the all-order linear PMD compensation method was used. As a result, the received signal can

be considered to be equal to the PMD-free case but slightly perturbed as a consequence of the interaction of nonlinearity with PMD. Such perturbation depends on the fibre length, PMD parameter, and signal itself. Next, the effect of such perturbation on the CS was investigated. A phase shift of constellation diagram as well as a noise-like error was observed for the CS signal in nonlinear spectral domain, both of which dependent to the signal energy, fibre length, PMD parameter, and instantaneous CS signal amplitude. The effect of constellation rotation can be mitigated by simple pre-compensation at the transmitter, Maximum-Likelihood detection, or modification of decision boundaries at the receiver. Finally, the combined effect of PMD and ASE noise considering the pre-compensation was studied which showed minimal impact of PMD. In conclusion, in chapter 5, it was demonstrated that the effect of PMD must be considered in system designs, but it can be small if some PMD compensation technique is used.

7.4 Soliton Communication and simultaneous signalling on both spectra

After a comprehensive analysis of the CS, a special case of signalling on the DS was studied in chapter 6. It was assumed that the data is mapped only on the imaginary part of a single eigenvalue (i.e., soliton amplitude or energy) which is equivalent to soliton amplitude communication. First, the signal-dependent noise statistics were verified by simulation, and, then, VNT was used to transform the channel with signal-dependent noise to an additive Gaussian noise channel. Due to the dependence of soliton pulse bandwidth to its amplitude, a peak amplitude constraint should also be considered for capacity evaluation. Channel capacities were calculated for the first time, using numerical methods as in chapter 3, for different available bandwidths, which showed 4 dB gain in SNR compared to the best available lower bound. More importantly, the achievable data rates were calculated by defining a proper temporal window for each pulse considering the induced timing jitter (i.e., Gordon-Haus effect). It was observed that the achievable data rates dramatically decrease for longer fibres because of the timing jitter, but higher available bandwidth results in larger achievable data rate. Finally, as a basic demonstration, data was mapped simultaneously on CS and DS, and it was observed that these spectra are almost independent and can carry the data successfully. It

is finally concluded that using the efficient techniques proposed in this thesis and mapping the data on both spectra can potentially lead to high data rates needed for current demands.

7.5 Future directions of the research

There is a huge range of topics and research directions in the field of optical fibre communication using NFT. However, several open problems exist which can be immediately looked into following this thesis. The capacity derived in this thesis and some other works are based on the direct signalling on CS and sampling for detection. It is obvious that any of the signal processing techniques proposed here, which reduce the error rate, can lead to higher channel capacity and achievable data rates. Therefore, estimating the channel capacity and achievable data rates using the methods proposed in this thesis can be a fruitful future research subject. Moreover, the techniques proposed in this thesis (for capacity analysis and signal processing) can potentially be applied to the polarization multiplexed system as well as NFT-based systems using both spectra. This, however, requires efficient numerical techniques for NFT and INFT operations to make it possible to perform extensive simulations. Another important topic can be the development of NFT-based systems using CS and/or DS for dispersion compensating fibre links. Such research project can be hugely beneficial because most of the currently installed fibres are dispersion compensating fibres. The optical fibre communication techniques proposed in this thesis and other works can immediately be implemented practically because all can be performed digitally without any additional requirement. However, different issues, which are not considered in the theoretical analysis, may affect the system. For instance, higher order dispersion, nonlinearity, and polarization effect, which are not included in NLSE, may reduce the system performance. Other potentially degrading effects can be named as imperfect Raman amplification, noises added during photo-detection, and device limitation. It should be noted that the recent observed experimental results, such as in [149, 150], confirm that NFT can indeed be implemented practically despite reduced performance compared to simulation results. Generally, since NFT is a new topic, many works can be done in future, a few of which were mentioned here.

Bibliography

[1] K. Kao and G. A. Hockham, "Dielectric-fibre surface waveguides for optical frequencies," in *Proceedings of the Institution of Electrical Engineers*, vol. 113, pp. 1151–1158, Jul 1966.

[2] E. Agrell, M. Karlsson, A. Chraplyvy, D. J. Richardson, P. M. Krummrich, P. Winzer, K. Roberts, J. K. Fischer, S. J. Savory, B. J. Eggleton, *et al.*, "Roadmap of optical communications," *Journal of Optics*, vol. 18, p. 063002, May 2016.

[3] T. Li, "Advances in optical fiber communications: A historical perspective," *IEEE Journal on Selected Areas in Communications*, vol. 1, pp. 356–372, Apr. 1983.

[4] R. J. Sanferrare, "Terrestrial lightwave systems," *AT&T technical journal*, vol. 66, pp. 95–107, Jan. 1987.

[5] A. R. Chraplyvy, A. H. Gnauck, R. W. Tkach, and R. M. Derosier, "8*10 Gb/s transmission through 280 km of dispersion-managed fiber," *IEEE Photonics Technology Letters*, vol. 5, pp. 1233–1235, Oct 1993.

[6] P. J. Winzer and D. T. Neilson, "From scaling disparities to integrated parallelism: A decathlon for a decade," *Journal of Lightwave Technology*, vol. 35, pp. 1099–1115, Mar. 2017.

[7] D. Qian, M.-F. Huang, E. Ip, Y.-K. Huang, Y. Shao, J. Hu, and T. Wang, "101.7-Tb/s (370× 294-Gb/s) PDM-128QAM-OFDM transmission over 3× 55-km SSMF using pilot-based phase noise mitigation," in *National Fiber Optic Engineers Conference*, p. PDPB5, Optical Society of America, Mar. 2011.

[8] A. Sano, T. Kobayashi, S. Yamanaka, A. Matsuura, H. Kawakami, Y. Miyamoto, K. Ishihara, and H. Masuda, "102.3-Tb/s (224× 548-Gb/s) C-band extended L-band all-Raman transmission over 240 km using PDM-64QAM single carrier FDM with digital pilot tone," in *Optical Fiber Communication Conference and Exposition (OFC/NFOEC), 2012 and the National Fiber Optic Engineers Conference*, pp. 1–3, Mar. 2012.

[9] R. Essiambre, G. Kramer, P. J. Winzer, G. J. Foschini, and B. Goebel, "Capacity limits of optical fiber networks," *Lightwave Technology, Journal of*, vol. 28, pp. 662–701, Feb. 2010.

[10] E. Desurvire, "A quantum model for optically amplified nonlinear transmission systems," *Optical Fiber Technology*, vol. 8, no. 3, pp. 210–230, 2002.

[11] P. P. Mitra and J. B. Stark, "Nonlinear limits to the information capacity of optical fibre communications," *Nature*, vol. 411, no. 6841, p. 1027, 2001.

[12] P. Poggiolini, G. Bosco, A. Carena, V. Curri, Y. Jiang, and F. Forghieri, "The GN-model of fiber non-linear propagation and its applications," *Journal of lightwave technology*, vol. 32, pp. 694–721, Feb. 2014.

[13] M. Secondini and E. Forestieri, "On XPM mitigation in WDM fiber-optic systems," *IEEE Photonics Technology Letters*, vol. 26, pp. 2252–2255, Nov. 2014.

[14] G. Kramer, M. I. Yousefi, and F. R. Kschischang, "Upper bound on the capacity of a cascade of nonlinear and noisy channels," in *Information Theory Workshop (ITW), 2015 IEEE*, pp. 1–4, IEEE, 2015.

[15] R. Dar and P. J. Winzer, "Nonlinear interference mitigation: methods and potential gain," *Journal of Lightwave Technology*, vol. 35, pp. 903–930, Apr. 2017.

[16] J. C. Cartledge, F. P. Guiomar, F. R. Kschischang, G. Liga, and M. P. Yankov, "Digital signal processing for fiber nonlinearities," *Optics Express*, vol. 25, pp. 1916–1936, Feb. 2017.

[17] D. Rafique, "Fiber nonlinearity compensation: commercial applications and complexity analysis," *Journal of Lightwave Technology*, vol. 34, pp. 544–553, Jan. 2016.

[18] E. Ip and J. M. Kahn, "Compensation of dispersion and nonlinear impairments using digital backpropagation," *Journal of Lightwave Technology*, vol. 26, pp. 3416–3425, Oct. 2008.

[19] L. B. Du and A. J. Lowery, "Improved single channel backpropagation for intra-channel fiber nonlinearity compensation in long-haul optical communication systems," *Optics Express*, vol. 18, pp. 17075–17088, Aug. 2010.

[20] N. V. Irukulapati, H. Wymeersch, P. Johannisson, and E. Agrell, "Stochastic digital backpropagation," *IEEE Transactions on Communications*, vol. 62, pp. 3956–3968, Nov. 2014.

[21] C. B. Czegledi, G. Liga, D. Lavery, M. Karlsson, E. Agrell, S. J. Savory, and P. Bayvel, "Digital backpropagation accounting for polarization-mode dispersion," *Optics Express*, vol. 25, pp. 1903–1915, Feb. 2017.

[22] G. L. Lamb Jr, *Elements of soliton theory*. Wiley-Interscience, USA, 1980.

[23] J. Yang, *Nonlinear waves in integrable and nonintegrable systems*, vol. 16. Siam, 2010.

[24] M. Yousefi and F. Kschischang, "Information transmission using the nonlinear Fourier transform, part I: Mathematical tools," *IEEE Transactions on Information Theory*, vol. 60, pp. 4312–4328, Jul. 2014.

[25] M. Yousefi and F. Kschischang, "Information transmission using the nonlinear Fourier transform, part II: Numerical methods," *IEEE Transactions on Information Theory*, vol. 60, pp. 4329–4345, Jul. 2014.

[26] M. Yousefi and F. Kschischang, "Information transmission using the nonlinear Fourier transform, part III: Spectrum modulation," *IEEE Transactions on Information Theory*, vol. 60, pp. 4346–4369, Jul. 2014.

[27] S. K. Turitsyn, J. E. Prilepsky, S. T. Le, S. Wahls, L. L. Frumin, M. Kamalian, and S. A. Derevyanko, "Nonlinear Fourier transform for optical data processing and transmission: advances and perspectives," *Optica*, vol. 4, pp. 307–322, Mar. 2017.

[28] J. Sakaguchi, B. J. Puttnam, W. Klaus, Y. Awaji, N. Wada, A. Kanno, T. Kawanishi, K. Imamura, H. Inaba, K. Mukasa, *et al.*, "305 Tb/s space division multiplexed transmission using homogeneous 19-core fiber," *Journal of Lightwave Technology*, vol. 31, pp. 554–562, Sep. 2013.

[29] D. Richardson, J. Fini, and L. Nelson, "Space-division multiplexing in optical fibres," *Nature Photonics*, vol. 7, pp. 354–362, May 2013.

[30] Z. Tong, C. Lundström, P. Andrekson, C. McKinstrie, M. Karlsson, D. Blessing, E. Tipsuwannakul, B. Puttnam, H. Toda, and L. Grüner-Nielsen, "Towards ultrasensitive optical links enabled by low-noise phase-sensitive amplifiers," *Nature Photonics*, vol. 5, pp. 430–436, Jul. 2011.

[31] F. Poletti, M. N. Petrovich, and D. J. Richardson, "Hollow-core photonic bandgap fibers: technology and applications," *Nanophotonics*, vol. 2, pp. 315–340, Dec. 2013.

[32] C. S. Gardner, J. M. Greene, M. D. Kruskal, and R. M. Miura, "Method for solving the Korteweg-deVries equation," *Physical Review Letters*, vol. 19, p. 1095, Nov. 1967.

[33] C. S. Gardner, J. M. Greene, M. D. Kruskal, and R. M. Miura, "Korteweg-deVries equation and generalizations. VI. methods for exact solution," *Communications on pure and applied mathematics*, vol. 27, pp. 97–133, Jan 1974.

[34] A. Shabat and V. Zakharov, "Exact theory of two-dimensional self-focusing and one-dimensional self-modulation of waves in nonlinear media," *Soviet Physics JETP*, vol. 34, p. 62, Jan. 1972.

[35] A. Hasegawa and T. Nyu, "Eigenvalue communication," *Journal of lightwave technology*, vol. 11, pp. 395–399, Mar. 1993.

[36] M. J. Ablowitz and H. Segur, *Solitons and the inverse scattering transform*. SIAM, 1981.

[37] M. J. Ablowitz, D. J. Kaup, A. C. Newell, and H. Segur, "Nonlinear-evolution equations of physical significance," *Physical Review Letters*, vol. 31, p. 125, Jul. 1973.

[38] J. E. Prilepsky, S. A. Derevyanko, K. J. Blow, I. Gabitov, and S. K. Turitsyn, "Nonlinear inverse synthesis and eigenvalue division multiplexing in optical fiber channels," *Phys. Rev. Lett.*, vol. 113, p. 013901, Jul. 2014.

[39] S. T. Le, J. E. Prilepsky, and S. K. Turitsyn, "Nonlinear inverse synthesis for high spectral efficiency transmission in optical fibers," *Optics express*, vol. 22, pp. 26720–26741, Nov. 2014.

[40] S. T. Le, J. E. Prilepsky, and S. K. Turitsyn, "Nonlinear inverse synthesis technique for optical links with lumped amplification," *Optics express*, vol. 23, pp. 8317–8328, Apr. 2015.

[41] S. T. Le, J. E. Prilepsky, P. Rosa, J. D. Ania-Castanon, and S. K. Turitsyn, "Nonlinear inverse synthesis for optical links with distributed Raman amplification," *Journal of Lightwave Technology*, vol. 34, pp. 1778–1786, Apr. 2016.

[42] S. T. Le, I. D. Philips, J. E. Prilepsky, P. Harper, A. D. Ellis, and S. K. Turitsyn, "Demonstration of nonlinear inverse synthesis transmission over transoceanic distances," *Journal of Lightwave Technology*, vol. 34, pp. 2459–2466, May 2016.

[43] M. I. Yousefi and X. Yangzhang, "Linear and nonlinear frequency-division multiplexing," *arXiv preprint arXiv:1603.04389*, Mar. 2016.

[44] X. Yangzhang, M. Yousefi, A. Alvarado, D. Lavery, and P. Bayvel, "Nonlinear frequency-division multiplexing in the focusing regime," in *Optical Fiber Communication Conference*, pp. Tu3D–1, Optical Society of America, Mar. 2017.

[45] S. T. Le and H. Buelow, "64 x 0.5 Gbaud nonlinear frequency division multiplexed transmissions with high order modulation formats," *Journal of Lightwave Technology*, 2017.

[46] S. A. Derevyanko, J. E. Prilepsky, and S. K. Turitsyn, "Capacity estimates for optical transmission based on the nonlinear Fourier transform," *Nature Commun.*, vol. 7, p. 12710, Sep. 2016.

[47] D. Kaup, "A perturbation expansion for the Zakharov–Shabat inverse scattering transform," *SIAM Journal on Applied Mathematics*, vol. 31, pp. 121–133, Jul. 1976.

[48] A. Hasegawa and Y. Kodama, *Solitons in optical communications*. No. 7, Oxford University Press, USA, 1995.

[49] J. P. Gordon and H. A. Haus, "Random walk of coherently amplified solitons in optical fiber transmission," *Optics Letters*, vol. 11, pp. 665–667, Oct. 1986.

[50] D. Wood, "Constraints on the bit rates in direct detection optical communication systems using linear or soliton pulses," *Journal of Lightwave Technology*, vol. 8, pp. 1097–1106, Jul. 1990.

[51] E. Dianov, A. Luchnikov, A. Pilipetskii, and A. Prokhorov, "Long-range interaction of picosecond solitons through excitation of acoustic waves in optical fibers," *Applied Physics B: Lasers and Optics*, vol. 54, pp. 175–180, Feb. 1992.

[52] J. M. Jacob, E. A. Golovchenko, A. N. Pilipetskii, G. M. Carter, and C. R. Menyuk, "10-Gb/s transmission of NRZ over 10000 km and solitons over 13500 km error-free in the same dispersion-managed system," *IEEE Photonics Technology Letters*, vol. 9, pp. 1412–1414, Oct. 1997.

[53] E. Meron, M. Feder, and M. Shtaif, "On the achievable communication rates of generalized soliton transmission systems," *arXiv preprint arXiv:1207.0297*, Jul. 2012.

[54] O. Yushko, A. Redyuk, M. Fedoruk, and S. Turitsyn, "Coherent soliton communication lines," *Journal of Experimental and Theoretical Physics*, vol. 119, pp. 787–794, Nov. 2014.

[55] Q. Zhang and T. H. Chan, "A Gaussian noise model of spectral amplitudes in soliton communication systems," in *IEEE International Workshop on Signal Processing Advances in Wireless Communications*, pp. 455–459, IEEE, Jun. 2015.

[56] Q. Zhang and T. H. Chan, "A spectral domain noise model for optical fibre channels," in *IEEE International Symposium on Information Theory*, pp. 1660–1664, IEEE, Jun. 2015.

[57] Q. Zhang and T. H. Chan, "Achievable rates of soliton communication systems," in *Proceeding IEEE International Symposium on Information Theory*, pp. 605–609, Jul. 2016.

[58] Q. Zhang and T. H. Chan, "Noise models in the nonlinear spectral domain for optical fibre communications," *arXiv preprint arXiv:1702.06226*, Feb. 2017.

[59] N. A. Shevchenko, S. A. Derevyanko, J. E. Prilepsky, A. Alvarado, P. Bayvel, and S. K. Turitsyn, "On the capacity of the noncentral Chi-channel with applications to soliton amplitude modulation," *arXiv preprint arXiv:1609.02318*, Apr. 2017.

[60] N. A. Shevchenko, J. E. Prilepsky, S. A. Derevyanko, A. Alvarado, P. Bayvel, and S. K. Turitsyn, "A lower bound on the per soliton capacity of the nonlinear optical fibre channel," in *Proceeding of IEEE Information Theory Workshop*, pp. 104–108, Oct. 2015.

[61] S. Hari, M. I. Yousefi, and F. R. Kschischang, "Multieigenvalue communication," *Journal of Lightwave Technology*, vol. 34, pp. 3110–3117, Jul. 2016.

[62] Z. Dong, S. Hari, T. Gui, K. Zhong, M. I. Yousefi, C. Lu, P.-K. A. Wai, F. R. Kschischang, and A. P. T. Lau, "Nonlinear frequency division multiplexed transmissions based on NFT," *IEEE Photonics Technology Letters*, vol. 27, pp. 1621–1623, Aug.

[63] V. Aref and H. Buelow, "Design of 2-soliton spectral phase modulated pulses over lumped amplified link," in *European Conference on Optical Communication*, pp. 1–3, VDE, Sep. 2016.

[64] H. Bulow, "Nonlinear Fourier transformation based coherent detection scheme for discrete spectrum," in *Optical Fiber Communications Conference and Exhibition*, pp. 1–3, IEEE, Mar. 2015.

[65] K. Schuh, V. Aref, and H. Buelow, "Collision of QPSK modulated solitons," in *Optical Fiber Communication Conference and Exhibition*, no. W2A.33, IEEE and OSA, Mar. 2016.

[66] S. Hari and F. R. Kschischang, "Bi-directional algorithm for computing discrete spectral amplitudes in the NFT," *Journal of Lightwave Technology*, vol. 34, pp. 3529–3537, Aug. 2016.

[67] T. Gui, T. H. Chan, C. Lu, A. P. T. Lau, and P. K. A. Wai, "Alternative decoding methods for optical communications based on nonlinear Fourier transform," *Journal of Lightwave Technology*, vol. 35, pp. 1542–1550, May 2017.

[68] A. Toyota and A. Maruta, "Wavelength division multiplexed optical eigenvalue modulated system," in *Digital Communications (TIWDC), 2015 Tyrrhenian International Workshop on*, pp. 43–45, IEEE, Sep. 2015.

[69] A. Span, V. Aref, H. Buelow, and S. t. Brink, "On time-bandwidth product of multi-soliton pulses," *arXiv preprint arXiv:1705.09468*, may 2017.

[70] A. Geisler and C. G. Schaeffer, "Experimental nonlinear frequency division multiplexed transmission using eigenvalues with symmetric real part," in *ECOC 2016; 42nd European Conference on Optical Communication; Proceedings of*, pp. 1–3, VDE, Sep. 2016.

[71] T. Gui, C. Lu, A. P. T. Lau, and P. Wai, "High-order modulation on a single discrete eigenvalue for optical communications based on nonlinear Fourier transform," *Optics Express*, vol. 25, pp. 20286–20297, Aug. 2017.

[72] E. G. Turitsyna and S. K. Turitsyn, "Digital signal processing based on inverse scattering transform," *Optics letters*, vol. 38, pp. 4186–4188, Oct. 2013.

[73] H. Bülow, "Experimental demonstration of optical signal detection using nonlinear Fourier transform," *Journal of Lightwave Technology*, vol. 33, pp. 1433–1439, Apr. 2015.

[74] H. Terauchi and A. Maruta, "Eigenvalue modulated optical transmission system based on digital coherent technology," in *OptoElectronics and Communications Conference/International Conference on Photonics in Switching*, pp. 1–2, IEEE, Jun. 2013.

[75] H. Terauchi, Y. Matsuda, A. Toyota, and A. Maruta, "Noise tolerance of eigenvalue modulated optical transmission system based on digital coherent technology," in *Optical Fibre Technology, 2014 OptoElectronics and Communication Conference and Australian Conference on*, pp. 778–780, IEEE, Jul. 2014.

[76] Y. Matsuda, H. Terauchi, and A. Maruta, "Design of eigenvalue-multiplexed multi-level modulation optical transmission system," in *Optical Fibre Technology, 2014 OptoElectronics and Communication Conference and Australian Conference on*, pp. 1016–1018, IEEE, Jul. 2014.

[77] S. Wahls and H. V. Poor, "Fast numerical nonlinear Fourier transforms," *IEEE Transactions on Information Theory*, vol. 61, pp. 6957–6974, Dec. 2015.

[78] M. K. Kopae, J. E. Prilepsky, S. T. Le, and S. K. Turitsyn, "Optical communication based on the periodic nonlinear Fourier transform signal processing," in *Photonics (ICP), 2016 IEEE 6th International Conference on*, pp. 1–3, IEEE, Mar. 2016.

[79] M. Kamalian, J. E. Prilepsky, S. T. Le, and S. K. Turitsyn, "Periodic nonlinear Fourier transform for fiber-optic communications, part I: theory and numerical methods," *Optics express*, vol. 24, pp. 18353–18369, Aug. 2016.

[80] M. Kamalian, J. E. Prilepsky, S. T. Le, and S. K. Turitsyn, "Periodic nonlinear Fourier transform for fiber-optic communications, part II: eigenvalue communication," *Optics express*, vol. 24, pp. 18370–18381, Aug. 2016.

[81] M. Kamalian, J. E. Prilepsky, S. T. Le, and S. K. Turitsyn, "Spectral efficiency estimation in periodic nonlinear Fourier transform based communication systems," in *Optical Fiber Communications Conference and Exhibition (OFC), 2017*, pp. 1–3, IEEE, Mar. 2017.

[82] V. Aref, S. T. Le, and H. Buelow, "Demonstration of fully nonlinear spectrum modulated system in the highly nonlinear optical transmission regime," in *European Conference on Optical Communication*, pp. 1–3, Sep. 2016.

[83] A. Maruta and Y. Matsuda, "Polarization division multiplexed optical eigenvalue modulation," in *Photonics in Switching (PS), 2015 International Conference on*, pp. 265–267, IEEE, Sep. 2015.

[84] J.-W. Goossens, M. I. Yousefi, Y. Jaouën, and H. Hafermann, "Polarization-division multiplexing based on the nonlinear Fourier transform," *arXiv preprint arXiv:1707.08589*, Jul. 2017.

[85] S. Gaiarin, A. M. Perego, E. P. da Silva, F. Da Ros, and D. Zibar, "Experimental demonstration of dual polarization nonlinear frequency division multiplexed optical transmission system," *arXiv preprint arXiv:1708.00350*, Aug. 2017.

[86] O. Belai, L. Frumin, E. Podivilov, and D. Shapiro, "Efficient numerical method of the fiber Bragg grating synthesis," *JOSA B*, vol. 24, pp. 1451–1457, Jul. 2007.

[87] S. Civelli, L. Barletti, and M. Secondini, "Numerical methods for the inverse nonlinear Fourier transform," in *Digital Communications (TIWDC), 2015 Tyrrhenian International Workshop on*, pp. 13–16, IEEE, Sep. 2015.

[88] S. Civelli, E. Forestieri, and M. Secondini, "Impact of discretization and boundary conditions in nonlinear frequency-division multiplexing," in *Photonic Technologies (Fotonica 2016), 18th Italian National Conference on*, pp. 1–4, IET, Jun. 2016.

[89] L. L. Frumin, O. V. Belai, E. V. Podivilov, and D. A. Shapiro, "Efficient numerical method for solving the direct Zakharov–Shabat scattering problem," *JOSA B*, vol. 32, pp. 290–296, Feb. 2015.

[90] V. Aref, "Control and detection of discrete spectral amplitudes in nonlinear Fourier spectrum," *arXiv preprint arXiv:1605.06328*, May. 2016.

[91] I. T. Lima, V. S. Grigoryan, M. O'Sullivan, and C. R. Menyuk, "Computational complexity of nonlinear transforms applied to optical communications systems with normal dispersion fibers," in *Photonics Conference (IPC), 2015*, pp. 277–278, IEEE, Oct. 2015.

[92] S. Wahls and H. V. Poor, "Introducing the fast nonlinear Fourier transform," in *Acoustics, Speech and Signal Processing (ICASSP), 2013 IEEE International Conference on*, pp. 5780–5784, IEEE, May 2013.

[93] V. Vaibhav and S. Wahls, "Multipoint Newton-type nonlinear Fourier transform for detecting multi-solitons," in *Optical Fiber Communications Conference and Exhibition (OFC), 2016*, pp. 1–3, IEEE, Mar. 2016.

[94] S. Wahls and H. V. Poor, "Fast inverse nonlinear Fourier transform for generating multi-solitons in optical fiber," in *Information Theory (ISIT), 2015 IEEE International Symposium on*, pp. 1676–1680, IEEE, Jun. 2015.

[95] S. Wahls and H. V. Poor, "Fast numerical nonlinear Fourier transforms," *IEEE Transactions on Information Theory*, vol. 61, pp. 6957–6974, Dec. 2015.

[96] S. Wahls and V. Vaibhav, "Fast inverse nonlinear Fourier transforms for continuous spectra of Zakharov-Shabat type," *arXiv preprint arXiv:1607.01305*, Jul 2016.

[97] V. Vaibhav and S. Wahls, "Introducing the fast inverse NFT," in *Optical Fiber Communications Conference and Exhibition (OFC), 2017*, pp. 1–3, IEEE, Mar. 2017.

[98] G. P. Agrawal, *Nonlinear fiber optics*. Academic Press, 5 ed., 2013.

[99] G. P. Agrawal, *Fiber-Optic communication systems*. Wiley, 4 ed., 2010.

[100] M. J. Ablowitz, B. Prinari, and A. D. Trubatch, *Discrete and continuous nonlinear Schrödinger systems*, vol. 302. Cambridge University Press, 2004.

[101] F. Kapron, D. Keck, and R. Maurer, "Radiation losses in glass optical waveguides," *Applied Physics Letters*, vol. 17, pp. 423–425, Nov. 1970.

[102] C. R. Menyuk and B. S. Marks, "Interaction of polarization mode dispersion and nonlinearity in optical fiber transmission systems," *Journal of Lightwave Technology*, vol. 24, p. 2806, Jul. 2006.

[103] J. Gordon, L. Walker, and W. Louisell, "Quantum statistics of masers and attenuators," *Physical Review*, vol. 130, p. 806, Apr. 1963.

[104] J. Gordon, W. H. Louisell, and L. Walker, "Quantum fluctuations and noise in parametric processes. II," *Physical Review*, vol. 129, p. 481, Jan. 1963.

[105] J.-C. Bouteiller, K. Brar, J. Bromage, S. Radic, and C. Headley, "Dual-order Raman pump," *IEEE Photonics Technology Letters*, vol. 15, pp. 212–214, Feb. 2003.

[106] T. J. Ellingham, J. D. Ania-Castañón, R. Ibbotson, X. Chen, L. Zhang, and S. K. Turitsyn, "Quasi-lossless optical links for broadband transmission and data processing," *IEEE photonics technology letters*, vol. 18, pp. 268–270, Jan. 2006.

[107] J. S. Russell, "Report on waves," in *14th meeting of the British Association for the Advancement of Science*, pp. 311–390, Sep. 1844.

[108] J. Boussinesq, "Théorie de l'intumescence liquide appelée onde solitaire ou de translation se propageant dans un canal rectangulaire," *Comptes Rendus Acad. Sci (Paris)*, vol. 72, pp. 755–759, Jun. 1871.

[109] D. J. Korteweg and G. De Vries, "Xli. on the change of form of long waves advancing in a rectangular canal, and on a new type of long stationary waves," *The London, Edinburgh, and Dublin Philosophical Magazine and Journal of Science*, vol. 39, pp. 422–443, May 1895.

[110] E. Fermi, J. R. Pasta, and S. M. Ulam, "Studies of nonlinear problems," 1955.

[111] N. J. Zabusky and M. D. Kruskal, "Interaction of" solitons" in a collisionless plasma and the recurrence of initial states," *Physical review letters*, vol. 15, p. 240, Aug. 1965.

[112] P. D. Lax, "Integrals of nonlinear equations of evolution and solitary waves," *Communications on pure and applied mathematics*, vol. 21, pp. 467–490, Sep. 1968.

[113] S. V. Manakov, "On the theory of two-dimensional stationary self-focusing of electromagnetic waves," *Soviet Physics-JETP*, vol. 38, no. 2, pp. 248–53, 1974.

[114] D. Benney and G. J. Roskes, "Wave instabilities," *Studies in Applied Mathematics*, vol. 48, pp. 377–385, Dec. 1969.

[115] V. E. Zakharov, "Collapse of Langmuir waves," *Sov. Phys. JETP*, vol. 35, no. 5, pp. 908–914, 1972.

[116] A. Zvezdin and A. Popkov, "Contribution to the nonlinear theory of magnetostatic spin waves," *Sov. Phys. JETP*, vol. 2, p. 350, 1983.

[117] D. Benney and A. Newell, "The propagation of nonlinear wave envelopes," *Studies in Applied Mathematics*, vol. 46, pp. 133–139, Apr. 1967.

[118] M. J. Ablowitz, D. J. Kaup, and A. C. Newell, "The inverse scattering transform-Fourier analysis for nonlinear problems," *Studies in Applied Mathematics*, vol. 53, pp. 249–315, Dec. 1974.

[119] V. E. Zakharov and L. D. Faddeev, "Korteweg-de Vries equation: A completely integrable Hamiltonian system," *Functional analysis and its applications*, vol. 5, pp. 280–287, Oct. 1971.

[120] I. M. Gelfand and B. M. Levitan, *On the determination of a differential equation from its spectral function*. Rhode Island : American Mathematical Society Providence, Sep. 1955.

[121] V. A. Marchenko, "The periodic Korteweg–de Vries problem," *Matematicheskii Sbornik*, vol. 137, no. 3, pp. 331–356, 1974.

[122] G. Boffetta and A. Osborne, "Computation of the direct scattering transform for the nonlinear Schrödinger equation," *Journal of Computational Physics*, vol. 102, pp. 252–264, Oct. 1992.

[123] M. I. Yousefi, *Information transmission using the nonlinear Fourier transform*. PhD thesis, 2013.

[124] L. D. Faddeev and L. Takhtajan, *Hamiltonian methods in the theory of solitons*. Springer Science & Business Media, 2007.

[125] T. R. Taha and M. I. Ablowitz, "Analytical and numerical aspects of certain nonlinear evolution equations. II. numerical, nonlinear Schrödinger equation," *Journal of Computational Physics*, vol. 55, pp. 203–230, Aug. 1984.

[126] M. Lax, J. Batteh, and G. Agrawal, "Channeling of intense electromagnetic beams," *Journal of Applied Physics*, vol. 52, pp. 109–125, Jan. 1981.

[127] O. V. Sinkin, R. Holzlöhner, J. Zweck, and C. R. Menyuk, "Optimization of the split-step Fourier method in modeling optical-fiber communications systems," *J. Lightwave Technol.*, vol. 21, p. 61, Jan 2003.

[128] M. Ablowitz and J. Ladik, "Nonlinear differential–difference equations and Fourier analysis," *Journal of Mathematical Physics*, vol. 17, pp. 1011–1018, Jul. 1976.

[129] H. Segur and M. J. Ablowitz, "Asymptotic solutions and conservation laws for the nonlinear Schrödinger equation. I," *Journal of Mathematical Physics*, vol. 17, pp. 710–713, May 1976.

[130] V. Zakharov and S. Manakov, "Asymptotic behavior of non-linear wave systems integrated by the inverse scattering method," *Soviet Journal of Experimental and Theoretical Physics*, vol. 44, p. 106, Jul. 1976.

[131] S. A. Derevyanko, S. Turitsyn, and D. Yakushev, "Non-Gaussian statistics of an optical soliton in the presence of amplified spontaneous emission," *Optics Letters*, vol. 28, pp. 2097–2099, Nov. 2003.

[132] M. Bartlett, "The square root transformation in analysis of variance," *Journal of the Royal Statistical Society*, pp. 68–78, Jan. 1936.

[133] J. H. Curtiss, "On transformations used in the analysis of variance," *The Annals of Mathematical Statistics*, vol. 14, no. 2, pp. 107–122, 1943.

[134] P. R. Prucnal and B. E. Saleh, "Transformation of image-signal-dependent noise into image-signal-independent noise," *Optics letters*, vol. 6, pp. 316–318, Jul. 1981.

[135] M. Safari, "Efficient optical wireless communication in the presence of signal-dependent noise," in *IEEE International Conference on Communication Workshop*, pp. 1387–1391, Jun. 2015.

[136] A. Tsiatmas, F. M. Willems, and C. P. Baggen, "Square root approximation to the Poisson channel," in *IEEE International Symposium on Information Theory Proceedings*, pp. 1695–1699, Jul. 2013.

[137] T. M. Cover and J. A. Thomas, *Elements of information theory*. John Wiley & Sons, 2012.

[138] J. G. Smith, "The information capacity of amplitude-and variance-constrained sclar Gaussian channels," *Information and Control*, vol. 18, pp. 203–219, Apr. 1971.

[139] M. Sorokina, S. Sygletos, and S. Turitsyn, "Ripple distribution for nonlinear fiber-optic channels," *Opt. Express*, vol. 25, pp. 2228–2238, Feb. 2017.

[140] A. S. Skidin, O. S. Sidelnikov, M. P. Fedoruk, and S. K. Turitsyn, "Mitigation of nonlinear transmission effects for OFDM 16-QAM optical signal using adaptive modulation," *Optics Express*, vol. 24, pp. 30296–30308, Dec. 2016.

[141] A. A. Farid and S. Hranilovic, "Channel capacity and non-uniform signalling for free-space optical intensity channels," *IEEE Journal on Selected Areas in Communications*, vol. 27, pp. 1553–1563, Dec. 2009.

[142] L. Frumin, A. Gelash, and S. Turitsyn, "New approaches to coding information using inverse scattering transform," *Physical Review Letters*, vol. 118, p. 223901, May 2017.

[143] J. Rice, *Mathematical Statistics and Data Analysis*. Duxbury, 2 ed., 1995.

[144] C. Xie, M. Karlsson, P. A. Andrekson, H. Sunnerud, and J. Li, "Influences of polarization-mode dispersion on soliton transmission systems," *IEEE Journal of selected topics in quantum electronics*, vol. 8, pp. 575–590, May 2002.

[145] H. Sunnerud, C. Xie, M. Karlsson, R. Samuelsson, and P. A. Andrekson, "A comparison between different PMD compensation techniques," *Journal of Lightwave Technology*, vol. 20, p. 368, Mar. 2002.

[146] E. Ip, A. P. T. Lau, D. J. Barros, and J. M. Kahn, "Coherent detection in optical fiber systems," *Optics express*, vol. 16, pp. 753–791, Jan. 2008.

[147] R. Balakrishnan, "Soliton propagation in nonuniform media," *Physical Review A*, vol. 32, p. 1144, Aug. 1985.

[148] A. P. T. Lau and J. M. Kahn, "Signal design and detection in presence of nonlinear phase noise," *Journal of Lightwave Technology*, vol. 25, pp. 3008–3016, Oct. 2007.

[149] S. T. Le, V. Aref, and H. Buelow, "Nonlinear signal multiplexing for communication beyond the kerr nonlinearity limit," *Nature Photonics*, vol. 11, no. 9, p. 570, 2017.

[150] V. Aref, S. T. Le, and H. Buelow, "Modulation over nonlinear Fourier spectrum: Continuous and discrete spectrum," *J. Lightwave Technol.*, vol. 36, pp. 1289–1295, Mar 2018.